DEFECT QUANTUM EMITTERS IN GALLIUM NITRIDE

A Dissertation
Presented to the Faculty of the Graduate School
of Cornell University
in Partial Fulfillment of the Requirements for the Degree of
Doctor of Philosophy

by
Yifei Geng
December 2024

DEFECT QUANTUM EMITTERS IN GALLIUM NITRIDE

Yifei Geng, Ph.D.

Cornell University 2024

Single photon emitters (SPEs) are fundamental building blocks for quantum technologies. Ideal SPEs exhibit characteristics such as brightness, stability across diverse environments, linear polarization, and the ability to emit indistinguishable single-photon wave packets. GaN, a technically mature wide bandgap semiconductor extensively employed in various photonic and electronic devices, holds particular promise for on-chip photonic integration. This dissertation explores a series of experiments and theoretical investigations into the distinctive properties of GaN defect-based SPEs. Initially reported in 2017, GaN defect SPEs have a relatively short history. In the first part of this dissertation, we review this brief history along with the established properties of GaN SPEs. Subsequently, we formulate pertinent questions, the answers to which guide us into the main chapters of this study. The dissertation primarily discusses the dephasing mechanism of these SPEs at different temperatures, delves into the optical dipole structure and orientation, and investigates the ultrafast spectral diffusion properties of these emitters. Along this journey, sample nano-fabrication, various optical metrology techniques, optical simulations, and theoretical condensed matter physics come together to form a comprehensive understanding. In the final chapter, we summarize our research on GaN defect quantum emitters and discuss the future outlook for these SPEs in both fundamental research and device applications.

BIOGRAPHICAL SKETCH

Yifei Geng was born in November 1996 in China, into a family of high school teachers specializing in geography and ancient Chinese literature. His name, bestowed upon him by his parents, draws inspiration from the verses of an ancient Chinese poet. In 2015, Yifei embarked on his academic journey by participating in the college entrance exam. His path led him to Zhejiang University, where he faced the pivotal decision of choosing his major. After much contemplation, he found himself drawn to opto-electronic science and engineering, a choice that unfolded like a mysterious act of "spontaneous symmetry breaking." He humorously speculated that perhaps it was the universe's way of determining his ground state. Despite harboring an early interest in history, he discovered a passion for mathematics and physics during his undergraduate studies. This newfound enthusiasm propelled him to pursue a Ph.D. Continuing his academic pursuit, he applied to Cornell in 2019, securing admission after a concise interview where, once again, the enigmatic force of "spontaneous symmetry breaking" seemed to be at play.

Throughout his doctoral journey at Cornell, Yifei honed his skills in the cleanroom, mastering fabrication techniques and engaging in diverse metrology measurements. His commitment extended beyond optics, encompassing coursework across various realms of physics and mathematics. Although he recalls almost never arriving at fully correct answers for renormalization group calculations (especially when Feynman diagrams contained loops), nor for the high-order Lie derivative or covariant derivative given a complicated metric tensor, he still enjoys theoretical physics. Yifei's academic pursuits reflect not only his scientific acumen but also his willingness to explore the intricacies of different fields.

At the conclusion of his first year, Yifei excelled in the Ph.D. qualifying exam, distinguishing himself as the sole candidate to pass the quantum and solid-state subject exam that year. Throughout his doctoral studies, he delved into the intricacies of quantum optics, with a specific emphasis on single-photon sources. The genesis of this focus can be traced back to his second year when, grappling with uncertainty, he serendipitously examined discarded wafers using a confocal microscope. To his surprise, sharp emission peaks emerged from one GaN wafer, a discovery that felt like another instance of “spontaneous symmetry breaking,” occurring almost magically. Subsequently, he developed several research ideas and published a few papers in this field, supported by his advisor, Professor Farhan Rana. This scientific journey has reshaped his perspective on the world, instilling in him the belief that everything, whether acknowledged or not, must be underpinned by some physics and mathematics. With all that he has learned, he has equipped himself with the capabilities needed to confront future challenges.

Dedicated to my family, Cornell and people I love.

ACKNOWLEDGEMENTS

Here, I convey my boundless love and admiration for my family, mentors, friends, this hopeful world, and the captivating yet profoundly challenging realm of physics.

TABLE OF CONTENTS

LIST OF FIGURES

CHAPTER 1

INTRODUCTION TO SINGLE-PHOTON EMITTERS

1.1 Human-light interaction

Humanity has a long history of studying light. In fact, advancements in our understanding of light have consistently marked significant milestones in scientific progress and technological development. In geometric optics, light is considered as rays, with the core equation being the law of refraction (Snell's law), which can address the design problems of the vast majority of lighting and imaging systems. In wave optics, light is regarded as an electromagnetic wave, possessing attributes such as amplitude, frequency, polarization, and phase, and it can undergo interference and diffraction. Maxwell's equations are considered the cornerstone of wave optics and, importantly, gave rise to the theory of relativity. Within the framework of special relativity, any physical law must satisfy Lorentz covariance. In general relativity, curved spacetime is described by a specific metric tensor, and light propagates along (potentially curved) geodesics within it. In quantum optics, the electromagnetic field is quantized into photons, allowing us to study their statistical properties. Furthermore, in quantum electrodynamics, the electromagnetic field is represented by gauge bosons under the U(1) gauge group; a cross-section of the principal fiber bundle represents a gauge choice, and the gauge potential serves as the connection of the principal bundle. Humanity's understanding of light has reached profoundly advanced levels; however, "unfortunately," the application of light in the optics industry still remains primarily at the level of geometric optics and wave optics.

1.2 Single-photon source

How is light generated? This seemingly straightforward question is, in fact, profoundly intricate in its practical implications. Common sources of light include blackbody radiation (such as that emitted by our Sun), light resulting from atomic energy level transitions (as observed in hydrogen atomic spectra), and light emitted by lasers and light-emitting diodes (LEDs), among others. From the perspective of quantum optics, light sources can be classified into different types.

For instance, lasers exhibit coherent states, which are eigenstates of the photon annihilation operator. The photon statistics of coherent states follow a Poisson distribution. Assuming we have an ideal photon detector (one that can measure the number of photons received at a particular moment with infinitesimal time precision), using this detector to record the photons emitted by a laser would reveal that, at any given moment, there is a certain probability of detecting a specific number of photons. In contrast, a single-photon source, as the name implies, emits only one photon at a time, rather than simultaneously emitting two or more. The photon statistics follow a sub-Poissonian distribution, and such light exists in a photon number state, which is an eigenstate of the photon number operator. Figure 1.1 illustrates the comparison between classical light sources and single-photon sources.

So, how does one obtain a single-photon source? In fact, almost all single-photon sources can be modeled as a common physical system: a two-level system. Electrons are fermions, and in a two-level system (without considering spin), the Pauli exclusion principle dictates that the ground state and excited state can each hold only one electron. Thus, at most one electron can transition from the excited state to the ground state, emitting one photon in the process. While more complex scenarios may involve addi-

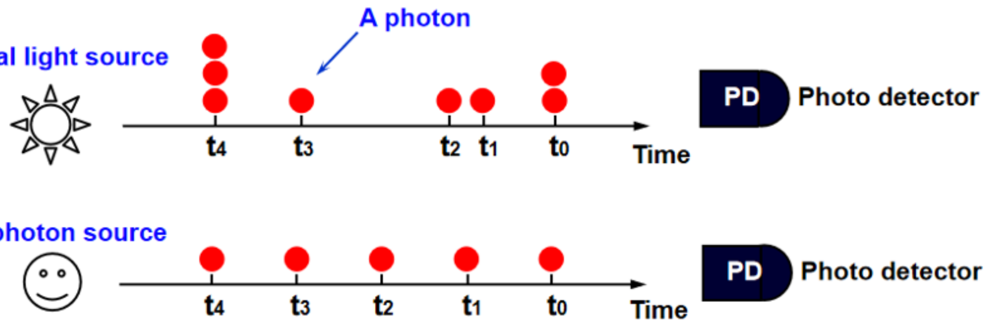

Figure 1.1: Comparison between classical light sources and single photon sources. If an ideal photon detector is used to record the number and arrival time of photons, a classical light source may produce multiple photons arriving simultaneously with some probability. In contrast, for a single-photon source, at most one photon arrives at any given time.

tional energy levels (such as metastable states), a two-level system is often sufficient to explain many physical aspects of single-photon sources. Common two-level systems include two suitable electron orbitals from the natural electron configurations of isolated atoms, two discrete energy levels of "artificial atoms" like quantum dots (which have discrete energy levels due to quantum confinement), or two-level systems formed by defect levels in the bandgap of semiconductor materials when defects are present, as shown in Figure 1.2.

1.3 Typical measurement of single-photon emitters

How can we demonstrate that a light source is a single-photon source? Ideally, we would use a perfect photon counter capable of recording the number of photons arriving at each moment with superfine time resolution (e.g. ~ 1 femtosecond). This is one of the hot research directions in quantum optical detector studies. However, in practice, common photon counters, such as avalanche photodiodes (APDs), suffer from dead time. After

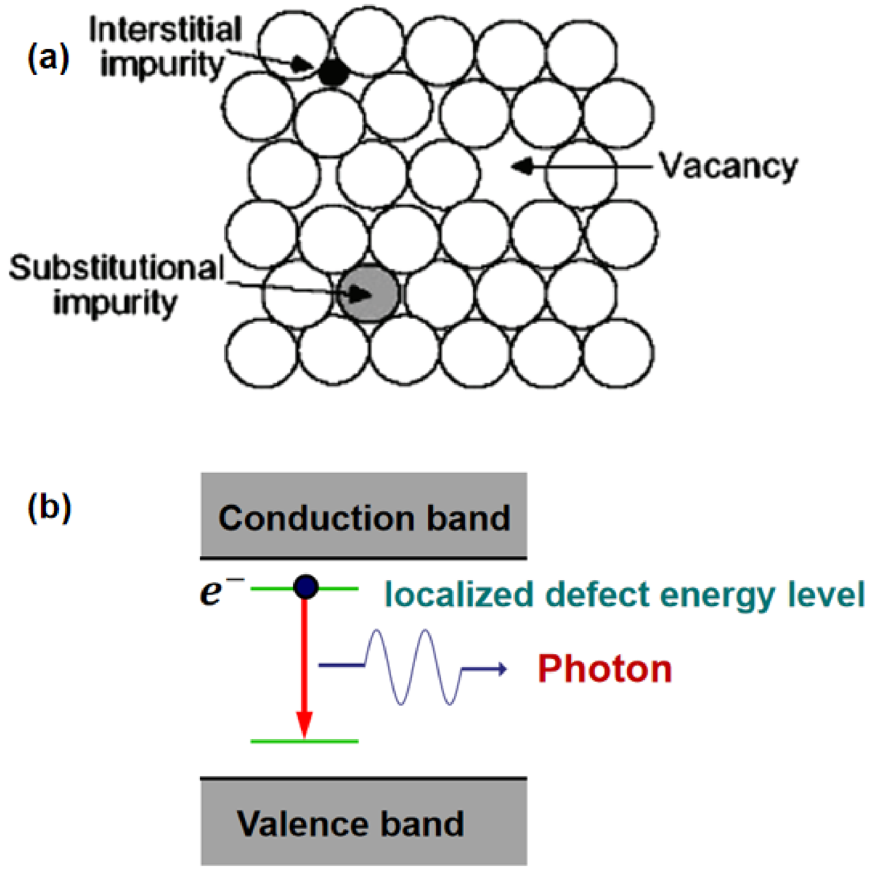

Figure 1.2: (a) Illustration of different point defects in a semiconductor crystal. (b) When defects are present, a two-level system can form in the bandgap, which can behave as a single-photon emitter.

detecting a photon, they generate an electrical pulse and require a certain amount of time—often several hundred picoseconds or a few nanoseconds—to deplete the charges. During this dead time, they cannot respond to or record any incoming photons.

To identify single-photon sources, we often resort to using Hanbury Brown and Twiss (HBT) interferometers to measure the second-order correlation function ($g^{(2)}$) of the incident light. As shown in Figure 1.3, an HBT interferometer typically consists of a 50:50 beam splitter, two photon detectors, and a photon correlator. The incident light enters the beam splitter and is split into two beams, which then enter two separate photon detectors. These detectors record whether a photon is received at each moment, resulting in a stream of photon event data for channels 1 and 2. The photon correlator measures the correlation function between these two channels. According to the interference theory of quantum optics, if two identical photons simultaneously enter the beam splitter, they will be separated after passing through it; each channel will receive one photon, preventing both photons from being detected in the same channel. If the light source is a single-photon source that emits one photon at regular intervals, it is impossible for both channels 1 and 2 to record a photon event simultaneously. At any given moment, the emitted photon will either appear in channel 1 or channel 2, but not in both. Consequently, the second-order correlation function exhibits a dip (antibunching) at a delay time of zero, approaching 1 at very large delay times. This indicates that after recording a photon event in channel 1, there is a possibility of recording a photon event in channel 2 after a significant time gap.

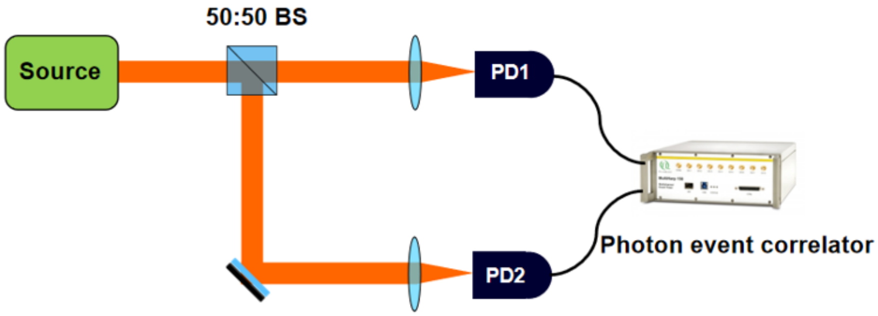

Figure 1.3: The typical setup for measuring $g^{(2)}$ is the Hanbury Brown and Twiss (HBT) interferometer, which usually includes a 50:50 beam splitter, two single-photon detectors, and a photon event correlator. The measurement of $g^{(2)}$ is central to quantum optics metrology.

If we assume the single-photon source is a two-level system, the measured second-order correlation function can be expressed as follows:

$$g^{(2)}(\tau) = 1 - ae^{-|\tau|/\tau_c} \tag{1.1}$$

where τ_c represents the characteristic time of antibunching, reflecting the lifetime of the excited state. In experiments involving a three-level system with a metastable state, a bunching effect may also be observed over longer time scales, superimposed on the antibunching effect. The correlation function measurement using the HBT interferometer is so crucial that many other important measurements can be considered variants of it. We will revisit this point in later chapters.

1.4 Ideal single-photon emitters

Single-photon sources play a crucial role in quantum communication and quantum computing [1], although current light sources used in quantum communication primarily consist of attenuated laser beams. For example, the BB84 protocol encodes information in the polarization direction of photons and employs attenuated lasers as light sources for quantum key distribution. However, attenuating the laser to obtain "single photons" reduces the usable brightness of the light source, thereby limiting the transmission rate of information.

For many years, researchers have made relentless efforts to develop perfect single-photon sources. A perfect single-photon source typically needs to possess the following characteristics:

1. High purity of single photons, indicating an extremely low probability of emitting two or more photons simultaneously.
2. High brightness, implying a large number of photons emitted per unit of time.

3. Linear polarization.
4. Ability to emit indistinguishable photons, meaning a narrow linewidth in the emission spectrum.
5. Operation at room temperature, eliminating the need for a cryogenic environment (such as liquid helium temperatures).
6. Attainability with mature materials, ensuring good prospects for on-chip integration applications.
7. Capability of being excited through electrical pumping, rather than optical pumping.
8. Stability, indicating that the single-photon source should exhibit long-term stable operation without susceptibility to issues such as photobleaching and blinking.
9. (Additional) If the single-photon source also exhibits favorable spin properties, it can serve not only as a single-photon source but also as a qubit for quantum computing or quantum sensing applications.

On-demand solid-state single-photon emitters have been realized in various material systems, including semiconductor quantum dots [2, 3], defects in two-dimensional materials [4, 5], and defects in wide bandgap materials such as diamond [6, 7] and silicon carbide (SiC) [8]. Numerous studies on their physical properties, as well as device-level applications, have been conducted over the last few years. Recently, defect-based single-photon emitters in aluminum nitride (AlN) [9] and gallium nitride (GaN) [10, 11] have also been reported.

As the focus of this thesis, GaN is a technically mature, direct wide bandgap semiconductor with extensive applications in photonic devices [12, 13, 14] and semiconductor RF and power devices [15, 16, 17, 18]. (The blue LED was awarded the Nobel

Prize in 2014 for this revolutionary achievement.) Therefore, single-photon sources in GaN hold particular significance. Once a quantum light source is realized in GaN, it can be seamlessly integrated with existing mature optoelectronic devices, facilitating convenient on-chip integration. Such advantages are not present in many other material systems, such as 2D materials and diamond. Notably, GaN hosts defect-based single-photon emitters, which were first reported in 2017 [10, 11]. Several properties have already been investigated, including photoluminescence spectrum, brightness, polarization, and lifetime. However, these aspects remain far from comprehensive, and the nature of these defects is still under debate. Some literature argues that these defects correspond to electronic states localized at stacking faults or dislocations [10, 19, 20], while others suggest they are substitutional atoms or vacancies [21].

1.5 "The big picture"

“What are scientists in the field of single-photon sources studying, and how do they do it?” This is a central question. As a researcher, the typical approach is as follows: First, choose a specific single-photon source as the research target. In the initial step, investigate its intrinsic physical properties, such as photoluminescence (PL) spectrum, lifetime, brightness, and polarization. The second step involves studying its response to external stimuli, including temperature-dependent properties, applied electric fields, magnetic fields, and stress. In the third step, employ nanofabrication techniques to couple the single-photon emitter into various structures, such as waveguides, resonant cavities, or metasurfaces, to achieve diverse applications. The fourth step explores its potential as a qubit, particularly if it possesses suitable spin properties. This opens up a new research direction, enabling the transfer of research paradigms, such as those from the study of NV centers in diamond, to this specific single-photon emitter.

Based on similar research approaches, understanding the underlying physics always remains the first step. For GaN defect single-photon emitters, we pose and aim to answer the following questions:

1. Defect-phonon interaction: How does it interact with phonons, and what is the dephasing mechanism?
2. Optical dipole structure and orientation: What is the optical dipole structure and orientation of GaN single-photon emitters, and is there any correlation with the crystal structure?
3. Spectral diffusion properties: What are the spectral diffusion properties, and can we achieve indistinguishable photons?
4. Nature of the defect: What is the nature of the defect single-photon emitters in GaN? Is it related to substitutional or interstitial atom impurities, stacking faults, or dislocations?

We will address the questions raised above. As a preview, answering the first question requires an investigation into the temperature-dependent photoluminescence (PL) spectra. We will observe how the linewidth and lineshape evolve with temperature, and we will develop a defect-phonon interaction model to explain the results [22, 23, 24, 25].

To answer the second question, we will employ defocused imaging techniques to measure the far-field radiation patterns of the optical dipoles. Subsequently, we can reconstruct the dipole orientation through Finite-Difference Time-Domain (FDTD) simulations [26, 27, 28].

For the third question, our primary focus will be on the strength and characteristic time of spectral diffusion. This involves measuring the time-dependent spectra; however, due to the constraints of conventional spectrometer readout times, we will use the

Hanbury Brown and Twiss (HBT) interferometer to selectively choose partial spectral windows for photon correlation measurements [29].

The research findings from the first three questions will significantly inform our investigation into the fourth question regarding the nature of these defects.

To address these questions, several tasks across various aspects are required, including the nanofabrication of samples in a cleanroom, the design and implementation of diverse metrology setups, experimental measurements, optical simulations, and theoretical physics calculations. These tasks form the main content of the next few chapters.

CHAPTER 2

DEPHASING MECHANISM OF GAN DEFECT SINGLE-PHOTON EMITTER

This chapter is mainly based on Ref[25].

2.1 Fundamentals

What does "dephasing" mean? A rigorous and comprehensive explanation of this term would be lengthy and complex. In our context, however, we can understand it simply as the broadening of the emission spectrum of a single-photon emitter due to various factors.

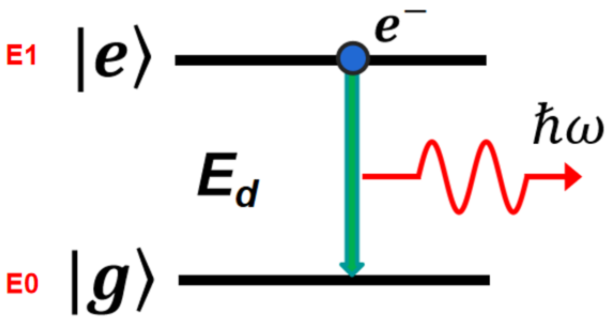

Figure 2.1: In a general two-level system, the energy of the ground state is $E0$ and the energy of the excited state is $E1$. When an electron transitions from the excited state to the ground state, it emits one photon with energy Ed, which corresponds to the energy difference between $E1$ and $E0$.

As shown in Figure 2.1, suppose the single-photon source is a two-level system, where the ground state has an energy of $E0$ and the excited state has an energy of $E1$. When an electron transitions from the excited state to the ground state, it emits a photon with a center energy of $E1 - E0$, which exactly corresponds to the energy difference between the two energy levels. The question is: what is the spectral linewidth of such emission? If no dephasing is involved, we know this corresponds to natural broadening.

Based on the energy-time uncertainty principle, the spectral linewidth is inversely proportional to the lifetime of the excited state, and their product is roughly on the order of Planck's constant.

$$\Delta E \, \Delta t \geq \hbar \tag{2.1}$$

From the literature, it has been demonstrated that the lifetime of the GaN defect single-photon source is approximately 1 to 2 nanoseconds. Therefore, the calculated natural linewidth of the spectrum is around micro-electronvolts ($\sim \mu$ eV). If this is true, it would be great! However, actual measurement results show that the spectral linewidth of the GaN defect single-photon source at room temperature (300 K) is approximately 10 meV, exceeding the natural linewidth value by ten thousand times. Figure 2.2 demonstrates the basic idea. Even in low-temperature environments (liquid helium temperature), their spectral linewidth is about 1 meV, still a thousand times greater than the calculated natural linewidth. Clearly, strong dephasing effects exist. More precisely, there are two different dephasing mechanisms at play: one is temperature-dependent, and the other is temperature-independent. Each mechanism gives rise to a different spectral line shape. In this chapter, we will focus on discussing these mechanisms in detail. But before we start, we need to lay some groundwork.

2.2 GaN defect single-photon emitters

The sample we are studying is semi-insulating GaN grown by the HVPE method on a sapphire substrate, as shown in Figure 2.3. The thickness of the GaN epitaxial layer is 4 μm, and the thickness of the sapphire substrate is 430 μm. Some single-photon emitters in GaN samples grown by MOCVD have also been reported in the literature.

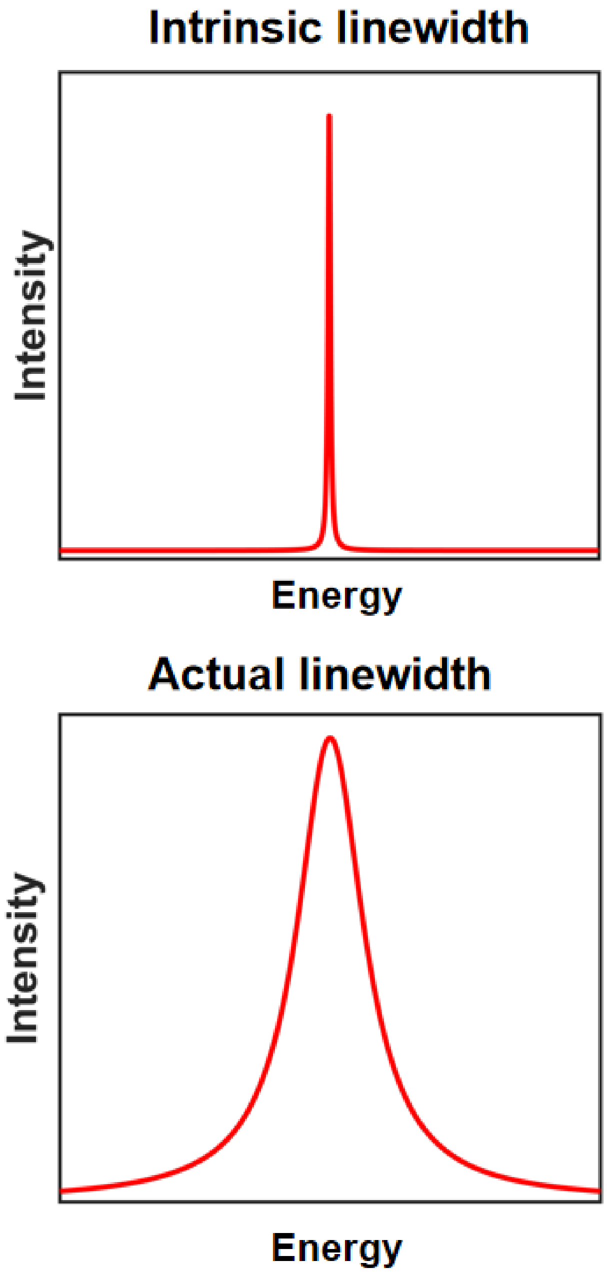

Figure 2.2: The ideal intrinsic linewidth, as determined by the energy-time uncertainty relation, compared to the actual linewidth determined by dephasing.

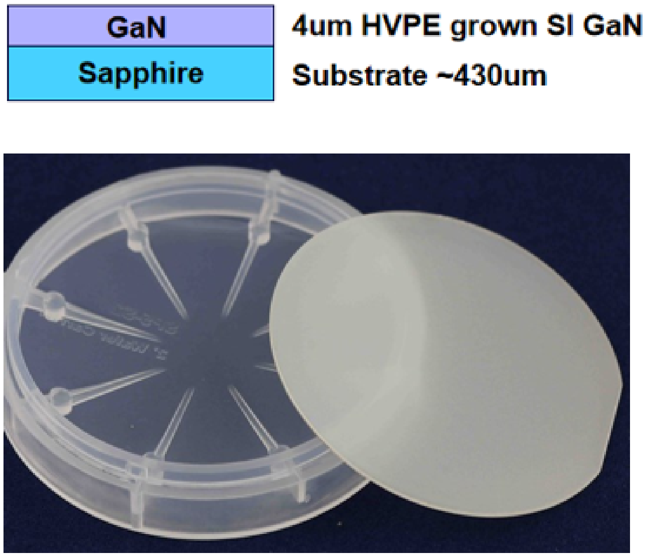

Figure 2.3: The sample under investigation is a 4 μm semi-insulating GaN layer grown using HVPE on a sapphire substrate.

If we use a 532 nm laser to excite the GaN sample and then collect the fluorescence signal using a confocal microscope, we can observe bright spots on the sample, which correspond to the defect emitters. These defect emitters are as-grown, meaning they can be directly found in the GaN sample without requiring any special treatment. By using a spectrometer to measure their spectra, we find that they are mainly concentrated in the visible light range, particularly in the red range from 600 nm to 700 nm. (Some literature also reports defect single-photon sources in GaN emitting in the infrared range, but we mainly focus on the visible light range here.)

Figure 2.4 shows five different defect emitters labeled E1 to E5, emitting spectra in the range of 600–700 nm at room temperature. From the graph, we can observe that their central wavelengths are 602.9 nm, 628.7 nm, 650.1 nm, 684.5 nm, and 710.5 nm, respectively. (The main emission line is sometimes referred to as the zero phonon line (ZPL) to distinguish it from the sidebands that arise from coupling with phonons,

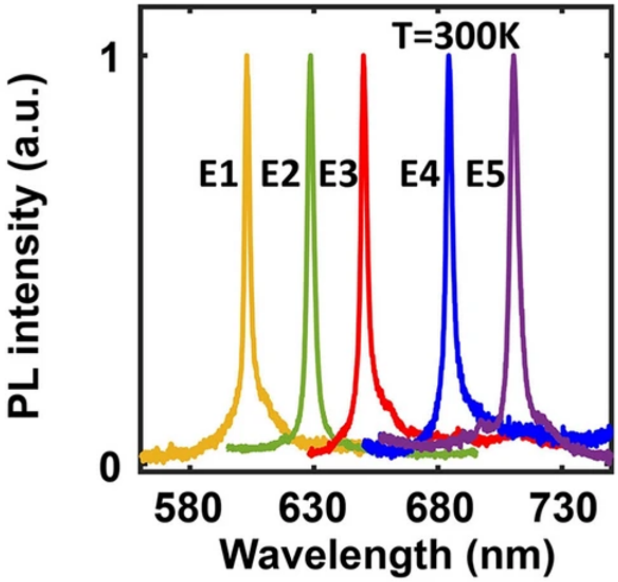

Figure 2.4: Representative PL spectra of five GaN SPEs, E1 through E5, are plotted at room temperature. Their central wavelengths are 602.9 nm, 628.7 nm, 650.1 nm, 684.5 nm, and 710.5 nm, respectively.

resulting in emission at other wavelengths.) Surprisingly, GaN defect emitters exhibit a strong and sharp ZPL even at room temperature. In contrast, for NV centers in diamond, the ZPL accounts for only 4% of the emission spectrum at room temperature, with the majority attributed to phonon sidebands. This characteristic makes GaN emitters more suitable as single-photon sources compared to NV centers in diamond.

After introducing the sample, we can move on to discussing the next steps of the experiment. However, before we proceed, we need to address an important engineering issue related to collection efficiency. This will be the main focus of the next section.

2.3 Solid immersion lens

GaN, as a technically mature wide-bandgap, direct-bandgap semiconductor material, serves as the primary platform for various optical devices such as LEDs, lasers, and waveguides, making it a promising candidate for photonic on-chip integration. However, GaN has a high refractive index, reaching up to 2.4 in the visible light range, compared to other optical materials such as glass, which has a refractive index of only 1.5. High refractive index materials are beneficial for integrated photonics applications, such as on-chip waveguides and resonant cavities, because they effectively confine light modes. However, for our research on single-photon sources, the high refractive index presents one of the main challenges we need to overcome. Assuming a defect emitter is embedded in GaN, with the top surface forming the GaN/air interface, where the refractive index of GaN is 2.4 and that of air is approximately 1, the light emitted by the defect emitter undergoes total internal reflection as it propagates from the optically dense medium to the optically rare medium.

According to Snell's law, the critical angle for total internal reflection is given by the equation:

$$\theta_c = arcsin(\frac{n_2}{n_1}) \tag{2.2}$$

This indicates that the critical angle of incidence on the GaN side is 24.6°, as shown in Figure 2.5 (a). However, we must also consider that, on the air side, only the transmitted light within the cone defined by the numerical aperture (NA) of the objective lens can be collected by our system. Therefore, the actual critical angle is even smaller, as illustrated in Figure 2.5 (b).

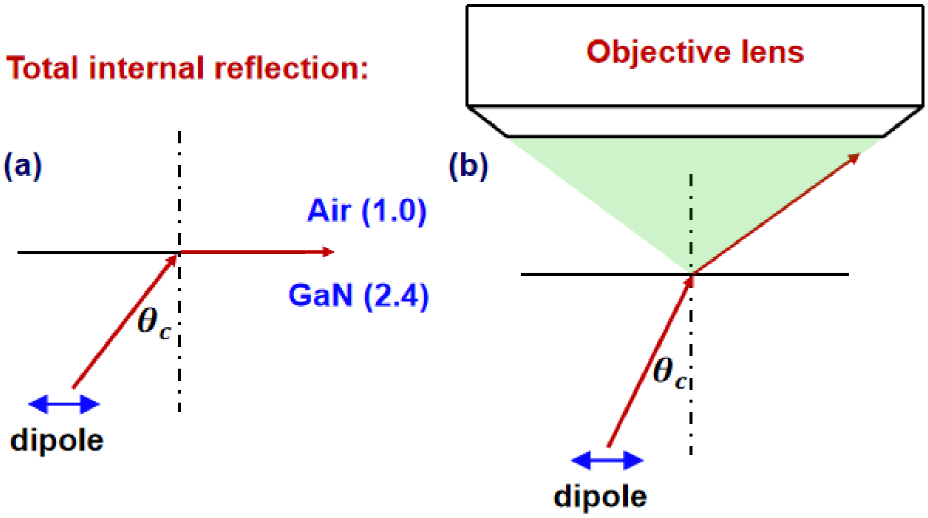

Figure 2.5: The total internal reflection at the GaN/air interface involves two key aspects: (a) the bare critical angle, which is determined by the difference in refractive indices, and (b) the actual critical angle, which is influenced by the numerical aperture (NA) of the objective lens.

$$\theta_c = arcsin(\frac{NA}{n_1}) \tag{2.3}$$

If the NA of the objective lens is 0.9, the calculated critical angle is 22°. This means that most of the light emitted by the defect emitter is reflected back into the substrate, resulting in a very weak light signal that can be collected on the air side. This limitation affects the signal-to-noise ratio (SNR) in many of our subsequent experiments, especially in low-temperature conditions where the sample is mounted in a cryostat, and only objectives with smaller NAs can be used to achieve sufficient working distance. To address this issue, we can design special structures at the interface between GaN and air to enhance collection efficiency. This can be achieved through nanofabrication. Common structures include coupling gratings[30], Fresnel lenses[31], solid immersion lenses[32, 33], and metasurface lenses[34].

Grating couplers are commonly used in integrated photonics applications, such as embedding single-photon sources into optical waveguides, transporting their emitted light to target locations, and coupling the light from the waveguide into free space for collection. This has been confirmed in recent years through various research studies involving defect SPEs in diamond and AlN. However, on-chip integrated optical waveguides are not the focus of this discussion.

Fresnel lenses and irregularly shaped inverse-design metasurface lenses are emerging as promising solutions for increasing light collection efficiency. For example, metasurface lenses based on inverse design can achieve a 20-fold improvement in collection efficiency for NV centers in diamond. However, the design of metasurface lenses typically relies on nanoscale structures to manipulate the phase of transmitted light, thereby achieving collimation. This approach tends to have significant effects only for individual wavelengths or narrow bandwidths, limiting its applicability for wider wavelength ranges. This specificity is particularly beneficial for applications involving NV centers in diamond, where the zero phonon line (ZPL) wavelength is precisely 637 nm, rather than a random value within a wide range. In contrast, the emission spectra of GaN defect single-photon emitters (SPEs) span a wide range of 600–700 nm. Designing a metasurface lens tailored to a bandwidth of 100 nm presents a considerable challenge in this case.

Solid immersion lenses are a more traditional and mature technology in microscopy. They employ individual hemispherical microlenses formed by etching material or depositing high index material on the sample surface to alter the angle of incidence of light on the surface of the optically dense medium, thereby overcoming total internal reflection at the interface. This approach can typically improve light collection efficiency by around five times. Although solid immersion lenses may not perform as well as metasurfaces, they still provide a significant enhancement. More importantly, solid immersion lenses do not exhibit strict wavelength selectivity (as long as the lens dimensions are much larger than the emission wavelength), making them suitable for wideband applications, which is precisely what we need for GaN defects in this context.

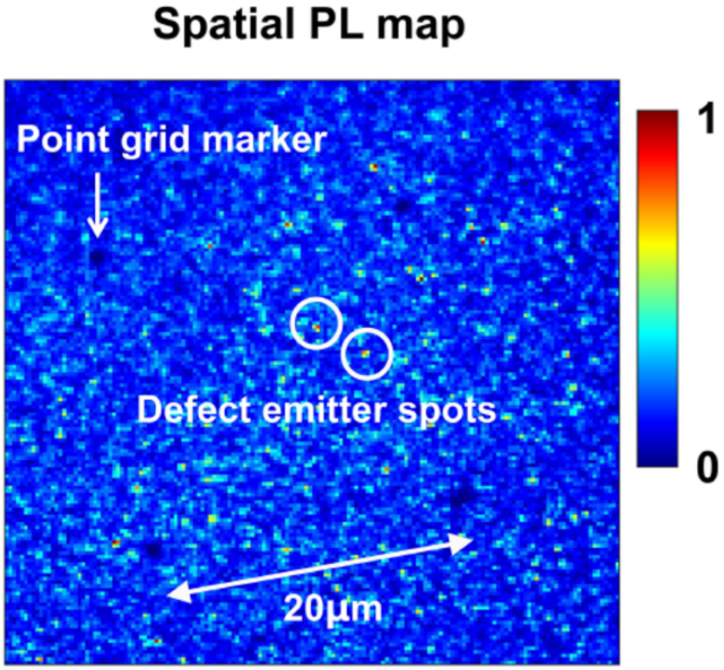

Figure 2.6: The spatial PL map of the GaN sample is shown. The horizontal and vertical axes represent the physical x and y directions, respectively, while the color indicates the normalized PL intensity. The dark spots are point grid markers etched onto the sample using FIB, spaced 20 μm apart, and the hot spots enclosed in white circles represent defect emitters. By measuring the relative distances between the defect emitters and the point markers, we can determine the precise locations of the defect emitters.

Based on the discussions above, we have decided to adopt the solid immersion lens technique to enhance the light collection efficiency of GaN defect single-photon emitters. The solid immersion lens is a hemisphere with a diameter of 5 μm, complemented by a cone trench. To etch the curved surface of the solid immersion lens onto the GaN, we use focused ion beam (FIB) milling.

The first question before fabrication is how to find the precise location of the defect emitters. We need to integrate the defect emitters into the solid immersion lens, as the performance of the lens depends on the position of the defect within it. If the defect emitter is located at the center of the solid immersion lens, the collection efficiency will be higher; conversely, if it is close to the edge, the collection efficiency will decrease. Thus, determining the precise location of the defect emitters is crucial.

As shown in Figure 2.6, we first use focused ion beam (FIB) milling to etch markers onto the GaN sample. These markers are holes with a diameter of 500 nm, spaced 20 μm apart. Afterward, we utilize a custom-built confocal scanning microscope (to be discussed in the next section) to acquire a photoluminescence (PL) map of the GaN sample. The horizontal and vertical axes represent the x and y directions, respectively, while the color indicates the normalized PL intensity. From the figure, we can see that the dark spots represent four marker points, while the hotspots within the white circles indicate the defect emitters. By measuring the distances between the defect emitters and the marker points, we can accurately determine their positions, ensuring they are precisely aligned with the center of the solid immersion lens to be etched. The overall accumulated fabrication error across all steps is typically less than 1 μm, which is important not only for this chapter but also for Chapter 4.

GaN is not a good electrical conductor, so when a focused ion beam is used for etching, the sample surface can accumulate charges that are not promptly discharged. These accumulated charges can deflect the ion beam, leading to distortion in the shape produced by the milling process. To address this issue, we pre-deposit a 30 nm layer of aluminum on the surface of the GaN sample via sputtering to enhance surface conductivity. After FIB milling, the remaining aluminum can be removed using a wet etch process.

Figure 2.7 shows a SEM image of five fabricated solid immersion lenses, clearly demonstrating the excellent fabrication results and the array of point markers. Figure

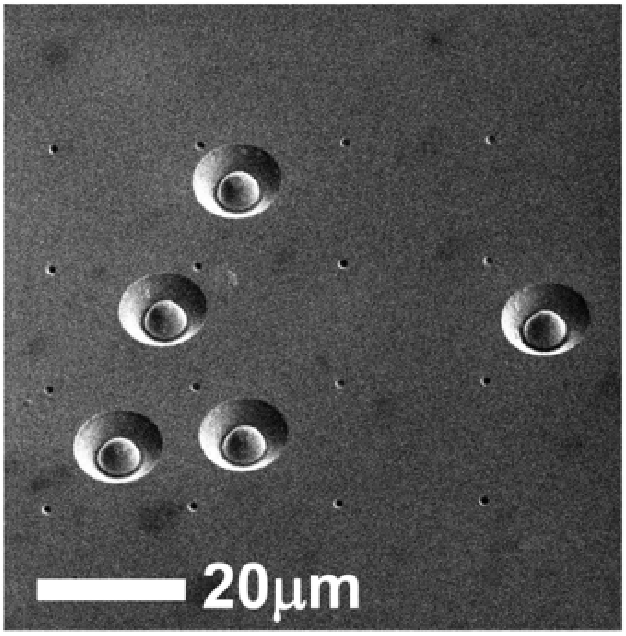

Figure 2.7: The SEM image of five fabricated solid immersion lenses is shown, clearly displaying the point grid markers as well.

2.8 presents a PL map of a defect emitter within a solid immersion lens; we can see that the hotspot in the center is the defect emitter, while the circular boundary indicates the edge of the solid immersion lens.

Figure 2.9 shows a comparison of defect emitter PL intensity before and after SIL fabrication, measured at room temperature using an objective lens with a numerical aperture of 0.9. The horizontal axis represents the excitation laser power, while the vertical axis indicates the number of photons collected by the photon detector per unit time. The experimentally measured PL intensity I_{pl} can be fitted using the following formula:

$$I_{pl} = I_{sat} \frac{P_{pump}}{P_{pump} + P_{sat}} \tag{2.4}$$

Here, I_{sat} is the saturation PL intensity, P_{pump} is the pump power, and P_{sat} is the satu-

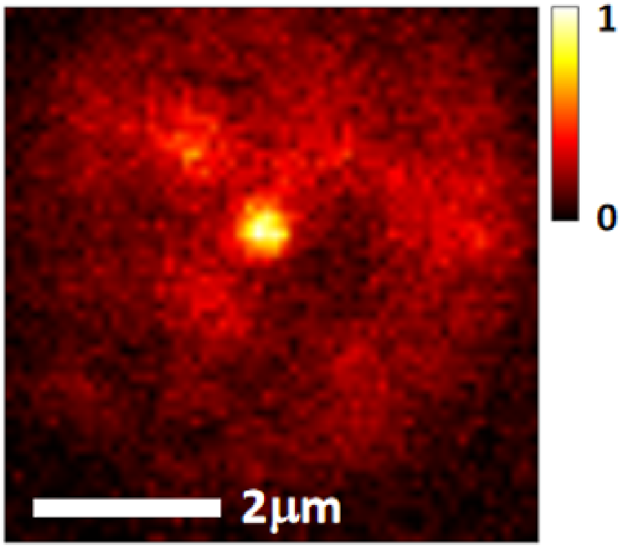

Figure 2.8: The spatial PL map of a defect emitter within a solid immersion lens is shown.

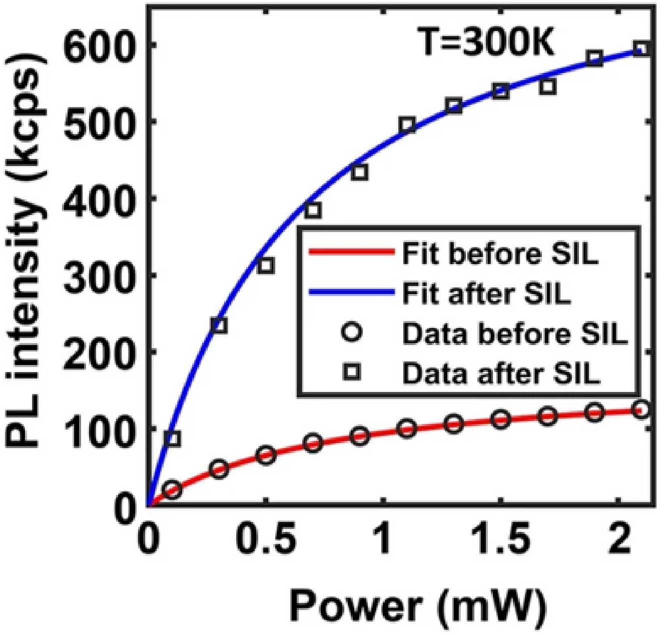

Figure 2.9: The comparison of the defect emitter power-dependent PL intensity before and after SIL fabrication was measured at room temperature using an objective lens with NA = 0.9.

ration pump power. For the data shown in Figure 2.9, P_{sat} is 650 μW, I_{sat} is 171 kcps without the SIL, and 779 kcps with the SIL, indicating that the PL collection efficiency is enhanced by a factor of approximately 4.5. This improvement in collection efficiency is crucial for ensuring an adequate signal-to-noise ratio (SNR), especially for the low-temperature experiments described in later sections. In those experiments, the sample will be mounted in a cryostat, and an objective lens with a smaller numerical aperture and a long working distance will be used to collect PL light through the cryostat window.

2.4 Confocal scanning microscope

The optical system is one of the most important experimental apparatuses in measurement methodology. Typically, various types of microscopes, especially confocal microscopes, are used to study semiconductor defect emitters. Microscopes generally consist of one objective lens, one tube lens, and a camera to magnify samples. However, due to the typically small sizes of point defects, only a small spot on the sample surface contributes to the signal, while the rest of the area appears as background noise. Confocal microscopes use a spatial filter, employing a pinhole several tens of micrometers in size, to select only the small area that contains the emitter and reject stray light from other regions, thereby ensuring a high SNR. The confocal pinhole filters out stray light not originating from the focal plane of the objective lens, collecting signals from a specific volume within the sample both laterally and axially.

Furthermore, it is often necessary to study multiple defect emitters on the sample. In such cases, incorporating scanning functionality into the confocal microscope is preferable. There are typically two methods to achieve scanning. One method involves mounting the sample on a piezo stage and moving the stage to observe different areas of the sample. The advantage of this method is its simplicity and convenience in terms of setup, but the drawback is its slower scanning speed. The other method involves using a steering mirror and a 4F system to move the laser spot. While this method results in a relatively complex system, it allows for high-speed scanning.

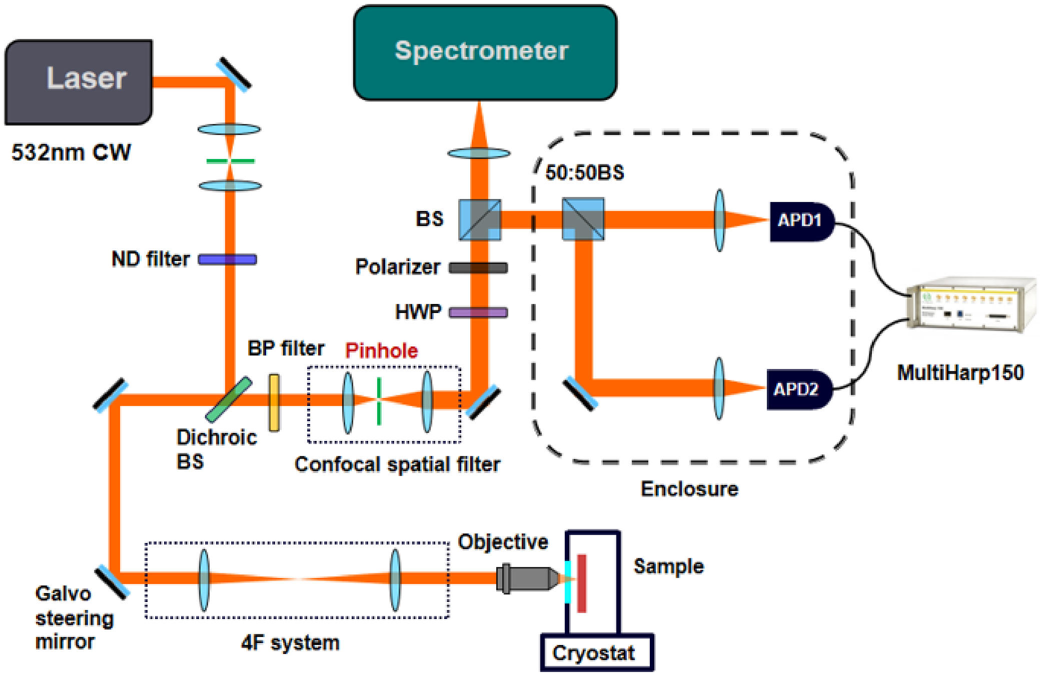

Figure 2.10: The confocal scanning microscope setup used for measuring second-order correlation functions $g^{(2)}$, polarization patterns, and PL spectra is depicted. A 532 nm laser excites the SPEs. The GaN sample is mounted inside a cryostat. A 4F system with a galvo steering mirror is employed for scanning. The collected PL light is split 50:50 into a spectrometer and a Hanbury-Brown and Twiss interferometer, which contains two single-photon detectors and a correlator. A half-wave plate and a polarizer in the collection path are used for polarization measurement.

Figure 2.10 illustrates a custom-built confocal scanning microscope setup. A 532 nm continuous-wave excitation laser passes through a spatial filter to clean the laser mode, then through a neutral density (ND) filter that controls the laser power. Subsequently, the laser is directed to a galvo scanning mirror after passing through a dichroic beam splitter. The galvo scanning mirror adjusts the reflection angle of the laser, while a 4F system conjugates the galvo mirror with the entrance pupil of the objective lens, ensuring that the laser can always enter the objective lens, even at different incident angles. The GaN sample is mounted inside a helium flow cryostat, with a temperature adjustable from room temperature to 4.4 K. For the collection path, the PL light emitted from the sample is collected by the same objective lens, then transmits through the dichroic beam splitter and a spectral bandpass filter, which selects only the wavelength range from 600 nm to 700 nm before entering the confocal spatial filter. The pinhole in the confocal spatial filter selects only the emitter spot while blocking all other stray light. Afterwards, the filtered PL light is split into two beams: one enters the spectrometer for PL spectrum measurement, and the other enters the HBT interferometer for the $g^{(2)}$ function measurement. The HBT interferometer consists of a 50:50 beam splitter, two single-photon counters (PMA Hybrid 40 from Picoquant), and a photon event correlator (MultiHarp 150 from Picoquant).

If needed, an additional half-wave plate and a polarizer can be inserted into the collection path to measure the polarization direction of the PL light. This will be an important part of our study to determine the optical dipole orientation of the defect emitters discussed in later chapters.

An important point to note is that, since the objective lens is placed outside the cryostat, the PL light from the sample passes through the cryostat window before entering the objective lens, and the laser is also focused on the sample through this window. This setup introduces significant spherical aberration because light with different incident angles will focus at different positions. To overcome this problem, a special objective lens with a correction collar is used. Some modern cryostats allow for the placement of the objective lens inside them, which can circumvent this issue and enable the use of high numerical aperture (NA = 0.9) objectives.

The above discussion outlines the main aspects of the confocal scanning microscope system. However, implementing the entire setup requires consideration of many specific technical details. This includes the selection of each optical and mechanical component, the alignment of each component to achieve optimal performance, and the mitigation of stray light within the system, which is particularly crucial for single-photon counters as they are extremely sensitive to stray light. Most importantly, it is essential to avoid significant vibrations during the transfer of liquid helium. Imagine this scenario: if the system's vibration due to helium transfer exceeds a few hundred nanometers, the size of the laser spot, we may miss the defect emitter during measurement. These are not fundamental issues and can all be resolved through careful engineering, although it may require some time and effort.

In fact, the aforementioned confocal scanning microscope is so versatile that, with slight modifications, it can be adapted to achieve many other functionalities. Numerous interesting experimental setups are built upon this foundation, and we will explore some of them in the following chapters as we study the spectral diffusion effect of the defect emitters at low temperatures.

Now that we have completed the fabrication of the solid immersion lens and the setup of the confocal scanning microscope system, it is akin to a warrior possessing a powerful weapon and a target. It is time for us to conduct experiments and achieve some exciting results.

2.5 Second-order correlation function results

First, let us demonstrate that these defect emitters are indeed single-photon emitters. Figure 2.11 shows the experimentally measured $g^{(2)}$ function of two defect emitters at room temperature. The $g^{(2)}$ values were obtained using the time-tagged time-resolved

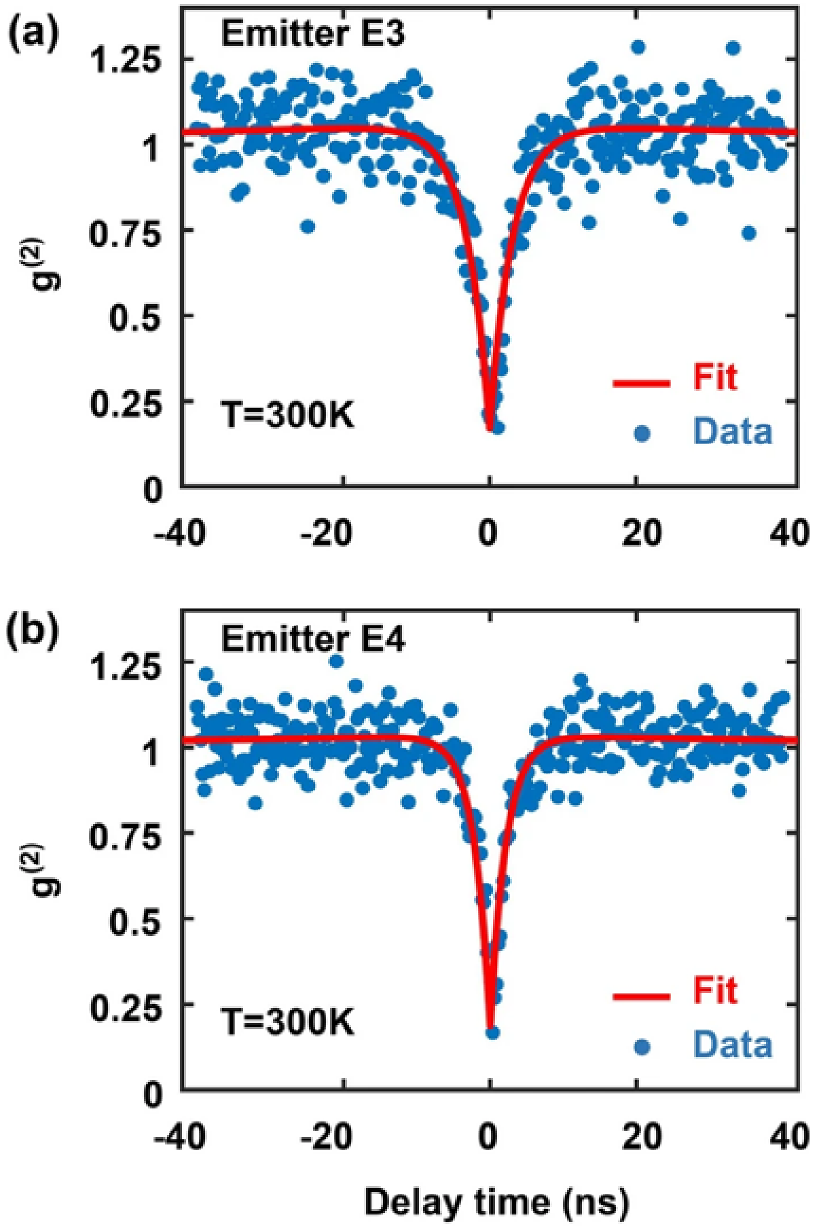

Figure 2.11: (a) The second-order correlation function $g^{(2)}(\tau)$ of emitter E3 (see Figure 2.4 for the label) is plotted, with $g^{(2)}(0) = 0.17$. (b) $g^{(2)}(\tau)$ of emitter E4 is plotted, with $g^{(2)}(0) = 0.19$. The solid lines represent the fits obtained using the expression provided in the text.

(TTTR) mode of the MultiHarp 150 instrument and were properly normalized. For both defect emitters, the measured $g^{(2)}$ function can be fitted using the following expression:

$$g^{(2)}(\tau) = 1 - ae^{-|\tau|/\tau_1} + be^{-|\tau|/\tau_2} \tag{2.5}$$

The fits are shown by the solid lines in Figure 2.11. The extracted values of τ_1 are 3.18 ± 0.24 ns and 2.2 ± 0.17 ns for emitters E3 and E4, respectively, and the values of τ_2 are 74 ± 27 ns and 65 ± 33 ns for emitters E3 and E4, respectively. The $g^{(2)}(0)$ values are 0.17 and 0.19 for emitters E3 and E4, respectively, confirming these defects as single-photon emitters.

Although two exponential terms are employed here to represent a more general scenario that captures transitions from metastable states (where both antibunching and bunching effects may coexist but occur at different time scales), experimental evidence suggests that, when the excitation laser power is sufficiently low, a simple two-level system model is adequate to describe the relevant physics. In fact, the bunching effect is so weak that it can be considered almost negligible due to the low laser power. Previous literature indicates that as laser power increases, the bunching effect becomes more pronounced and cannot be ignored. However, it is important to note that, in such cases, the observed bunching effect in the measured $g^{(2)}$ function solely arises from transitions involving metastable states. This point should be made very clear in advance, in preparation for later chapters where we will discuss the spectral diffusion effect.

2.6 Temperature-dependent spectra

As mentioned in Section 2.1, at room temperature, the linewidth of GaN defect emitters is on the order of 10 meV, which is significantly higher than the intrinsic linewidth deter-

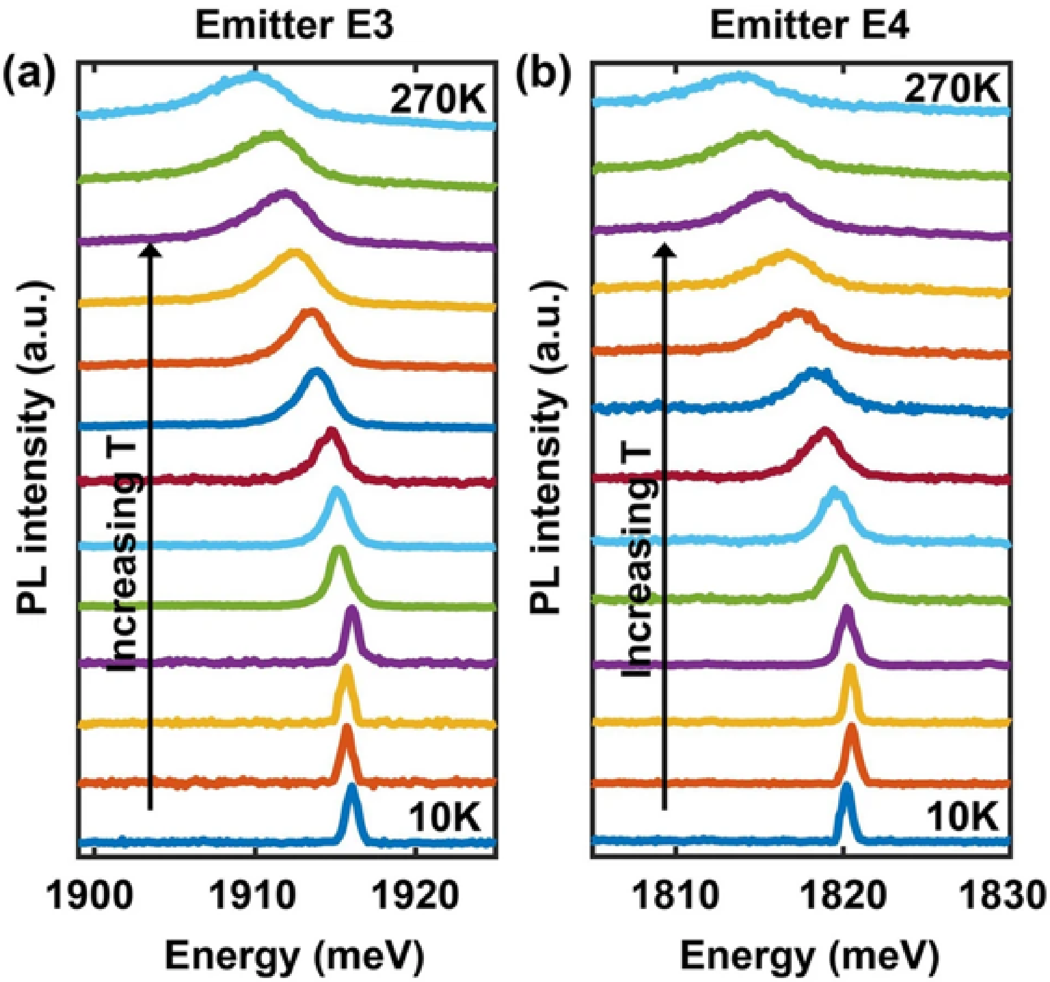

Figure 2.12: The emission spectra of emitter E3 (a) and emitter E4 (b) are plotted for different temperatures in the range of 10 K to 270 K, with an increment of 20 K. The labels for the emitters correspond to those in Figure 2.4.

mined by the energy-time uncertainty principle. We now want to investigate its dephasing mechanism. A natural conjecture is that dephasing is caused by defect-phonon interactions, although this factor only partially contributes to the overall dephasing. Proposing this conjecture is not difficult, as it has been confirmed for defect emitters in other material platforms, such as NV centers in diamond and defects in 2D materials like hBN. Phonons, being bosons, are distributed according to Bose-Einstein statistics, with their number decreasing as the temperature drops. Thus, we can explore the dephasing mechanism introduced by phonons by measuring temperature-dependent emission spectra. A natural hypothesis is that as the temperature decreases from room temperature to that of liquid helium, the emission spectrum linewidth should narrow, and indeed, experimental results have confirmed this. Using the setup described in Section 2.4, we varied the temperature of the GaN sample inside the cryostat from 10 K (low temperature) to 270 K (high temperature) to obtain temperature-dependent spectral results, as shown in Figure 2.12. This figure displays the temperature-dependent spectra of two distinct defect emitters: E3 and E4, as labeled in the previous Figure 2.4.

Firstly, we observe that as the temperature increases, the emission spectrum undergoes a redshift, indicating that the center energy decreases with rising temperature. This phenomenon has also been reported in other material platforms and occurs due to the reduction of the semiconductor bandgap width with increasing temperature. The zero-phonon line (ZPL) center energy of E3 shifts from 1916 meV at 10 K to 1909.4 meV at 270 K. For E4, the ZPL center energy shifts from 1820.2 meV at 10 K to 1813.5 meV at 270 K.

Secondly, as expected, we observe that the linewidth of the ZPL gradually narrows as the temperature decreases. It decreases from around 10 meV to about 1 meV, which is nearly an order of magnitude. However, 1 meV is still significantly larger than the intrinsic linewidth.

Now, we will delve deeper into the spectral line shapes at different temperatures. Our data shows that the ZPL spectra evolve from a Gaussian lineshape at temperatures below 50 K to a Lorentzian lineshape at temperatures above 125 K. This is illustrated in Figure 2.13, where we plot the ZPL spectra of emitters E3 and E4 at low (10 K) and high (270 K) temperatures, along with Gaussian and Lorentzian fits for both temperatures. At 10 K, the spectrum data (black dots) for E3 (E4) is fitted significantly better with a Gaus-

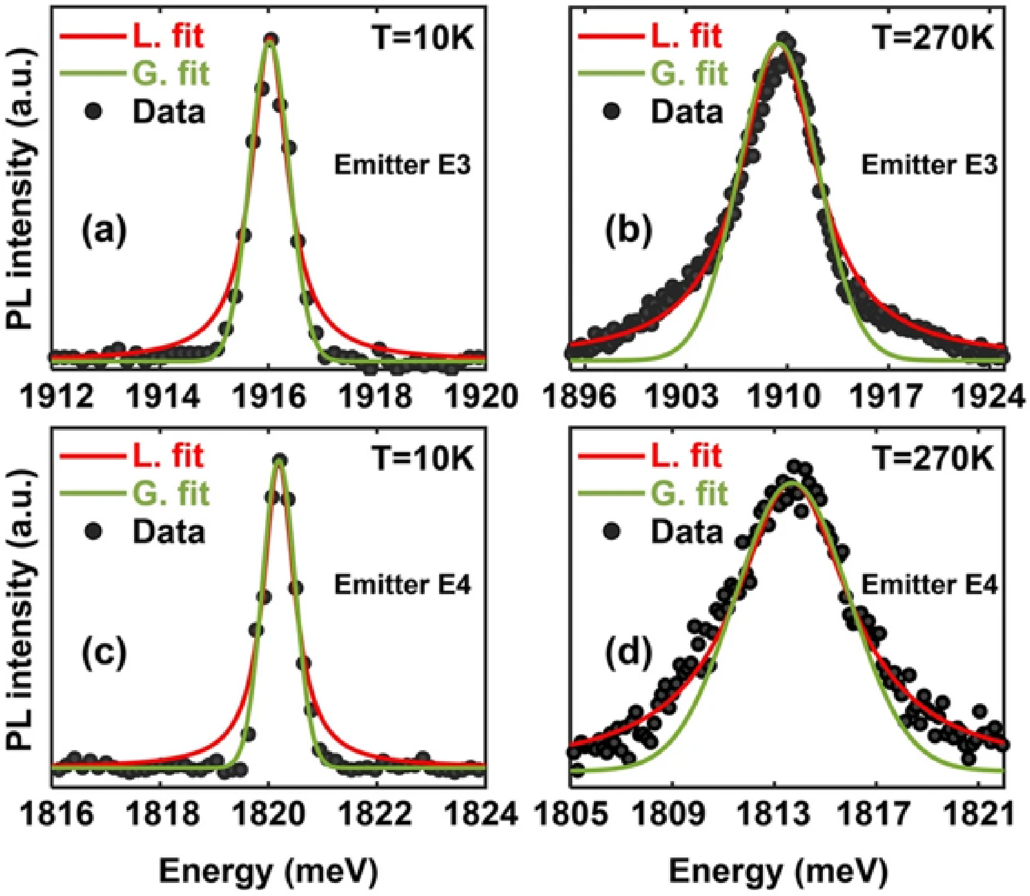

Figure 2.13: The ZPL spectra with Gaussian and Lorentzian fits at 10 K (a) and 270 K (b) for emitter E3 are plotted. Also shown are the ZPL spectra with Gaussian and Lorentzian fits at 10 K (c) and 270 K (d) for emitter E4. The labels for the emitters correspond to those in Figure 2.4.

sian spectral function (green curve), resulting in a full-width at half-maximum (FWHM) linewidth of 0.88 meV (0.72 meV). In contrast, at 270 K, the spectrum for E3 (E4) is fitted much better with a Lorentzian spectral function (red curve), yielding a FWHM linewidth of 7.12 meV (6.82 meV). These observations suggest that two different mechanisms are contributing to the linewidth, and one might assume that these mechanisms are independent. (Indeed, as we will see later, they are.)

Under this assumption, the ZPL spectral shape is more accurately described by a

Voigt function $V(\omega;\sigma,\gamma)$ which is a convolution of Gaussian and Lorentzian functions,

$$V(\omega;\sigma,\gamma) \propto \int_{-\infty}^{+\infty} G(\omega^{'};\sigma)L(\omega-\omega^{'};\gamma)d\omega^{'} \tag{2.6}$$

Here, $G(\omega;\sigma)$ and $L(\omega;\gamma)$ are Gaussian and Lorentzian functions with FWHM equal to $f_G = 2\sigma\sqrt{2\ln 2}$ and $f_L = 2\gamma$, respectively. The FWHM f_V of the Voigt function can be written as,

$$f_V = 0.5346 f_L + \sqrt{0.2166 f_L^2 + f_G^2} \tag{2.7}$$

By fitting the measured ZPL spectra with a Voigt function, we can extract the temperature-dependent FWHM of its Gaussian and Lorentzian components. We find that the FWHM of the Gaussian component is temperature-independent, remaining around 0.88 meV (0.72 meV) for emitters E3 (E4). An emission spectrum with a temperature-independent FWHM and a Gaussian lineshape is a common signature of spectral diffusion, where the emitter's emission energy changes over time due to factors such as variations in the local electric environment. This spectral diffusion effect has also been observed in other materials. We will study this in depth in later chapters, where more experimental results will be presented. For now, we can consider it a 'trivial' constant and turn our attention to the more interesting aspect: the Lorentzian component at higher temperatures.

To gain insight into the mechanism responsible for the Lorentzian component, we examine the FWHM linewidth of the ZPL as a function of temperature. This data is shown in Figure 2.14(a) for emitter E3 and in Figure 2.14(b) for emitter E4. It is evident that the Lorentzian component dominates the ZPL linewidth at temperatures exceeding approximately 125 K. Using the expression given in Eq.(2.7), we find that the temperature dependence of the FWHM of the Lorentzian component cannot be adequately fitted with an expression proportional to T^n, where n is any integer greater than or equal to

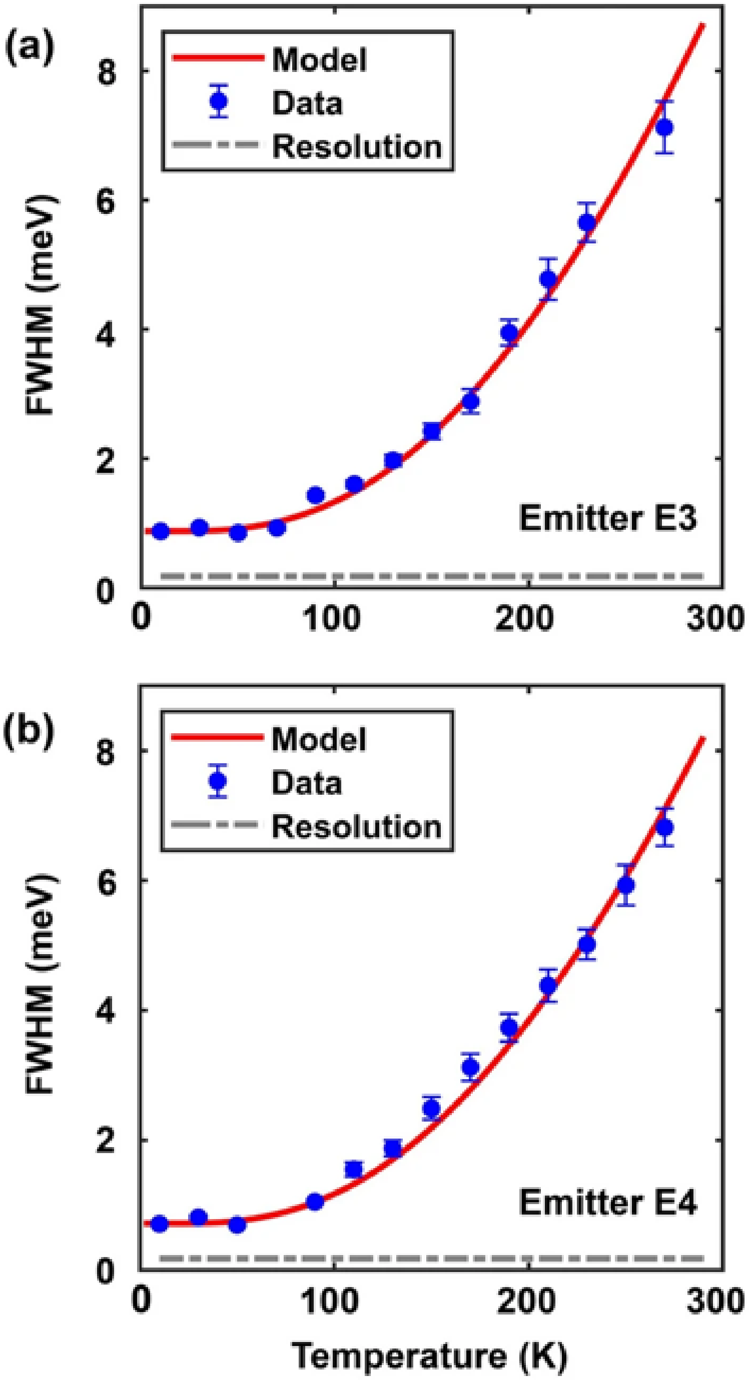

Figure 2.14: The FWHM linewidths of emitter E3 (a) and emitter E4 (b) are plotted as a function of temperature. The solid lines represent fits to the data using the theoretical model discussed in Section 2.8.

3 (with n equal to 3, 5, and 7 being common values for dephasing mechanisms in this field).

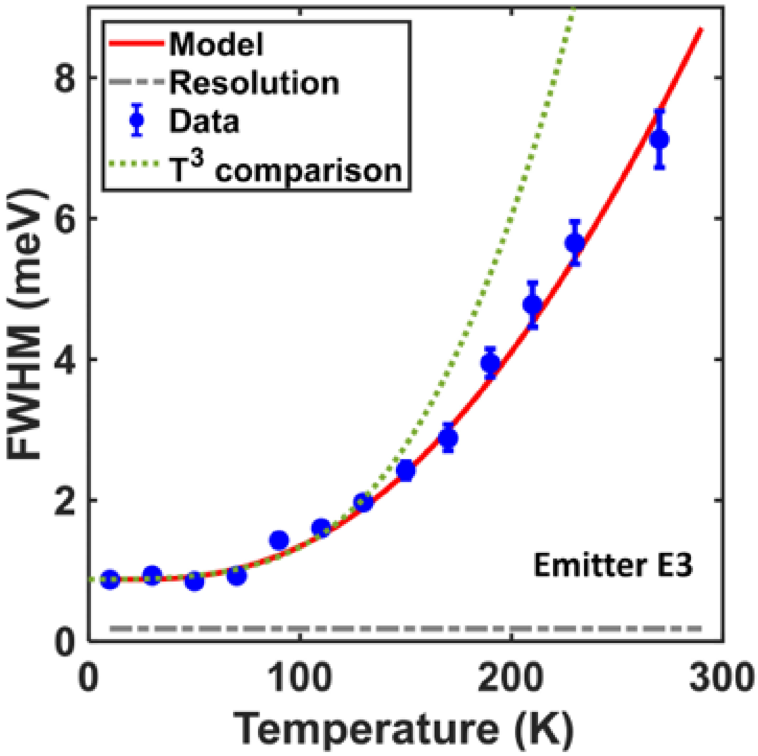

Figure 2.15: The FWHM linewidth of emitter E3 is plotted as a function of temperature. The solid line represents the fit to the data using the theoretical model discussed in Section 2.8. The dotted line illustrates an attempt to fit the data with a model in which the temperature dependence of the linewidth is proportional to T^3.

Figure 2.15 shows the poor comparison with the data obtained when the temperature dependence of the linewidth of the Lorentzian component is assumed to be T^3. It is evident that dephasing mechanisms resulting in T^5 orT^7 temperature dependence will also not align with the data. This indicates that the common dephasing mechanisms might not be the dominant dephasing mechanisms in the case of GaN SPEs. Therefore, we need to propose a new physical model to explain these experimental results. Before doing so, however, I would like to address a few key issues that I have identified as common misconceptions in the literature on this topic.

2.7 Common misconceptions

In studies investigating the temperature dependence of spectral linewidth for various emitters in this field, researchers commonly present figures like this: the horizontal axis represents temperature, while the vertical axis represents linewidth, similar to Figure 2.14 in this dissertation. The first misconception is that some papers use nanometers (in the wavelength domain) as the unit for measuring linewidth.

Note: please refrain from doing so.

As we later discuss the dephasing mechanism, it is common to propose an expression for the Hamiltonian. By solving it, we ultimately obtain an expression that describes the emission spectrum as a function of temperature. Since the Hamiltonian represents energy, the appropriate units should be those of energy (such as meV) or frequency (such as THz), as energy and frequency are directly proportional to each other. Throughout the derivation process, however, wavelength does not appear, even though it is inversely proportional to energy. Therefore, when representing the linewidth in the wavelength domain instead of the energy domain, the following relationship exists:

$$dE = \frac{hc}{\lambda^2} d\lambda \tag{2.8}$$

From this, it can be seen that $d\lambda$ and dE do not follow a simple linear relationship; instead, they relate to the central wavelength of the emission spectrum. And since we know that the central wavelength of the emission spectrum changes with temperature, a plot of linewidth (measured in nanometers in the wavelength domain) against temperature will exhibit distortion. If you claim that your linewidth in nanometers satisfies a

T^3 dependence, I would be curious to know how this T^3 dependence translates to the energy domain, and how it can be explained.

The second misconception is that, while we can currently treat the Gaussian term resulting from spectral diffusion at low temperatures as a ‘trivial’ constant (often referred to as ‘inhomogeneous broadening’ in the literature), it still requires careful consideration when included in the total linewidth.

Many papers do not use the previously mentioned formula 2.7 to represent the linewidth of the Voigt function; instead, they may adopt the following form:

$$Total\ linewidth\ (FWHM) = F(T) + C \tag{2.9}$$

Here, $F(T)$ represents the linewidth contribution from the temperature-dependent Lorentzian component (regardless of the model used), and C represents the Gaussian linewidth, which is incorrectly added as a constant directly to the temperature-dependent Lorentzian linewidth.

In fact, with some consideration, we can understand that the convolution of a Gaussian function with a Lorentzian function forms a Voigt function; however, the linewidth of this Voigt function is not simply the algebraic sum of the linewidths of the Gaussian and Lorentzian functions. In reality, there is no analytical expression for the linewidth of the Voigt function; instead, formula 2.7 provides the correct representation.

Therefore, if you come across an article (which is quite likely) that uses the form $F(T)+C$ to represent the total linewidth, be sure to remind yourself that there may be an issue with this approach.

If you are researching the temperature-dependent emission spectra of single-photon emitters and happen to read this dissertation, please remember not to use the form $F(T)+C$ for the total linewidth unless you have a very clear rationale for doing so. I would be immensely grateful for this.

After addressing the common misconceptions discussed above, we can now turn our attention to the new dephasing physical model. However, before we delve into that, it would be beneficial to review the various dephasing mechanisms that have been proposed in the past. This will be the main focus of the next section.

2.8 The theoretical model

Research on the dephasing mechanisms of defect single-photon sources has a rich history. The temperature-independent Gaussian linewidth, associated with spectral diffusion, has been confirmed in many materials. For now, let us set that aside and focus on the temperature-dependent linewidth component.

In most solid-state defect single-photon emitters (SPEs), interaction with low-energy acoustic phonons is responsible for the temperature dependence of dephasing rates as well as the broadening of emission linewidths. Various physical models have been proposed to explain the temperature dependence of the emission linewidths observed in solid-state SPEs. For instance, the T^3 temperature dependence observed in AlN, SiC, and hBN SPEs [9, 35, 36] has been attributed to acoustic phonon-induced dephasing in crystals with a high density of defects [37]. The T^5 dependence seen in NV^- centers in diamond is linked to the dynamic Jahn-Teller effect in the excited state [38, 39]. Additionally, the T^7 dependence observed in many solid-state emitters has been attributed to quadratic coupling to acoustic phonons [40, 41].

While interaction with optical phonons is generally not considered a significant dephasing mechanism at temperatures well below room temperature due to their high energy, this may not apply to GaN, where some optical phonon energies are relatively lower. We will explore this point in more detail later. However, before we proceed, let us consider a broader question: what kind of physical model could potentially be correct?

As physicists, a general approach to understanding this problem might proceed as follows:

First, since we are considering the temperature dependence of the emission spectrum, it is natural to examine the interaction between defects and phonons. To do this, we need to propose a reasonable Hamiltonian that describes such interactions. Next, we can employ various techniques from condensed matter many body physics to solve this Hamiltonian. Ultimately, our goal is to derive a relation that describes the dephasing rate, representing the Lorentzian linewidth, as a function of temperature:

$$Lorentzian\ linewidth\ (FWHM) = F(T) \tag{2.10}$$

Before proceeding, it is reasonable to ask: What properties are expected of this function $F(T)$?

Firstly, we need to impose some limitations on our model. For instance, we would not expect it to hold at extremely high temperatures (e.g., a few thousand K), where the material would have melted, as the model would naturally break down. Therefore, we consider only the temperature range up to and including room temperature.

Secondly, our natural intuition suggests that within this valid temperature range, as the temperature increases, more phonons will be present, leading to a monotonically increasing dephasing rate. While this is not always guaranteed, if you wish to argue for a function that oscillates with temperature, you would likely need to provide a very specific physical mechanism to support such a claim.

Thirdly, physicists often consider limits. For instance, we might want to ask what value this function takes as the temperature approaches absolute zero (0 K). At absolute zero, phonons cease to exist, and all lattice vibrations are frozen. Consequently, there is no defect-phonon interaction, and the temperature-dependent dephasing rate is zero at absolute zero, which means:

$$\lim_{T \to 0} F(T) = 0 \tag{2.11}$$

Figure 2.16 illustrates the qualitative behavior of the temperature-dependent linewidth component $F(T)$ as a function of temperature. It is expected to increase monotonically with temperature, approaching zero as the temperature approaches absolute zero.

Now, let us evaluate some of the models proposed in the past against these criteria. We will find that whether $F(t)$ is proportional to T^3, T^5, or T^7, all of these models satisfy the arguments outlined above: they are monotonically increasing and approach zero at absolute zero temperature.

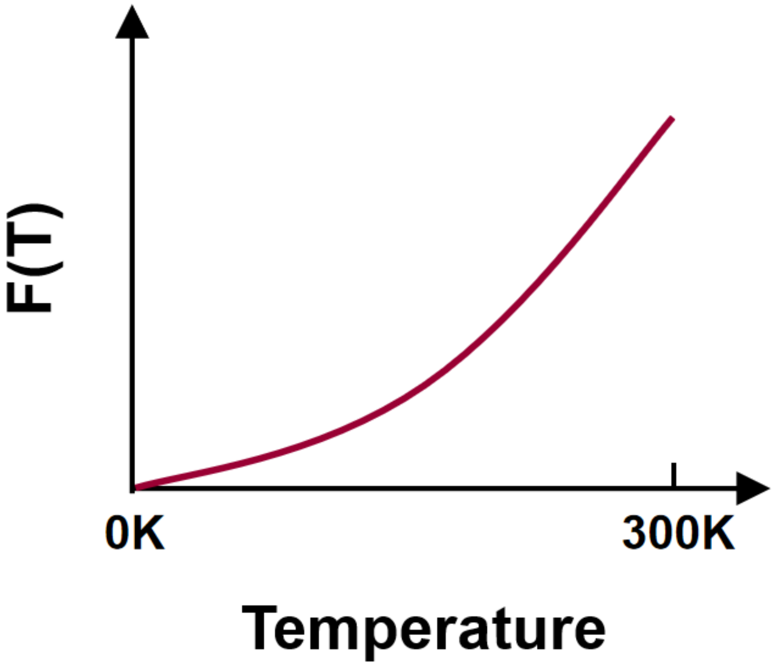

Figure 2.16: The expected shape of the temperature-dependent linewidth component due to defect-phonon interaction is illustrated. $F(T)$ is monotonically increasing with temperature, approaching zero as the temperature approaches absolute zero.

However, exponential functions may raise an issue. If one argues that $F(T) \propto e^{\alpha T}$, I would be curious to ask what happens as the temperature approaches zero. For an exponential function, as the temperature nears absolute zero, $F(T)$ approaches a non-zero constant. This implies that even at absolute zero, when no phonons are present, we would still have a non-zero dephasing rate due to defect-phonon interaction. This raises interesting questions!

Please note, as I have emphasized several times before, that here we are considering only the temperature-dependent dephasing rate caused by the defect-phonon interaction. In our current model, the Hamiltonian includes only this term as the interaction term. If we were to consider the Gaussian linewidth component caused by spectral diffusion, we would need to introduce another term in the Hamiltonian to describe it, which would be a constant unrelated to temperature and phonons.

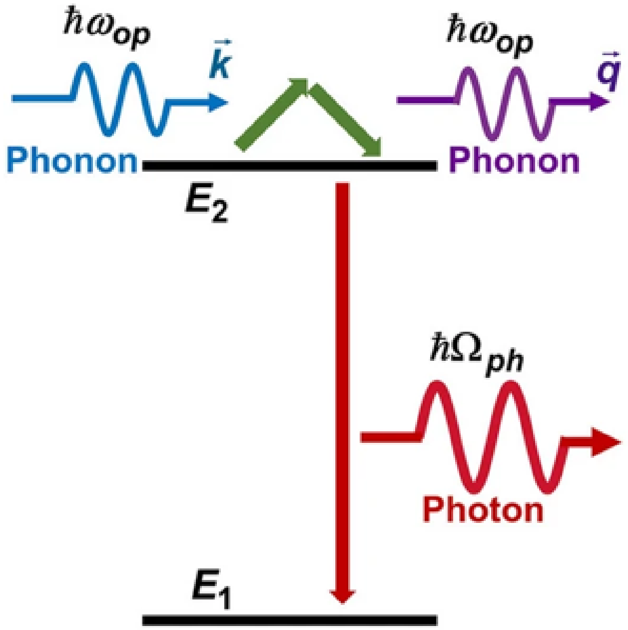

Figure 2.17: Proposed mechanism for dephasing involving absorption/emission of optical phonons via an elastic Raman process. E_2 (E_1) represents the excited (ground) state energy of the emitter.

The dephasing mechanism proposed here is depicted in Figure 2.17 and it involves absorption/emission of optical phonons in an elastic Raman process which results in the scattering of an optical phonon from the defect. A similar mechanism involving acoustic phonons is known to result in a dephasing rate proportional to T^7 in solid-state emitters [41, 40]. Although as depicted in Figure 2.17 the dephasing occurs only in the excited state, dephasing occurring by a similar process in the ground state can be handled in a way similar to the one shown below.

We assume that the Hamiltonian for the defect state interacting with optical phonons is,

$$
\begin{aligned}
H = & \sum_{j} \left[E_j + \alpha_j F(t) \right] c_j^{\dagger} c_j \\
& + \frac{1}{\sqrt{V}} \sum_{j \neq 2, \vec{k}} (M_{j,\vec{k}} c_j^{\dagger} c_2 + M^{*}_{j,-\vec{k}} c_2^{\dagger} c_j)(a_{\vec{k}} + a^{\dagger}_{-\vec{k}}) \\
& + \frac{1}{\sqrt{V'}} \sum_{\vec{k}} (F_{\vec{k}} c_1^{\dagger} c_2 + F^{*}_{-\vec{k}} c_2^{\dagger} c_1)(b_{\vec{k}} + b^{\dagger}_{-\vec{k}}) \\
& + \sum_{\vec{k}} \hbar \omega_{\vec{k}} a_{\vec{k}}^{\dagger} a_{\vec{k}} + \sum_{\vec{k}} \hbar \Omega_{\vec{k}} b_{\vec{k}}^{\dagger} b_{\vec{k}}
\end{aligned}
\tag{2.12}
$$

Here, c_j, $a_{\vec{k}}$, and $b_{\vec{k}}$ are the destruction operators for the electron, optical phonon, and photon states, respectively. E_j are the energies of the emitter electron states and, as shown in Fig. 2.17, $j = 1, 2$ states participate in photon emission. $\omega_{\vec{k}}$ are the frequencies of the optical phonons in a band that are coupled to the emitter. $\Omega_{\vec{k}}$ are the frequencies of the photon modes. V (V') is the volume in which the phonon (photon) modes are normalized. To model spectral diffusion, we have included terms in the electron energies linear in the external time-dependent electric field $F(t)$ which is assumed to be caused by time-dependent charges in the environment. Terms quadratic in $F(t)$ can also be included in the Hamiltonian but their inclusion does not affect the discussion that follows and the conclusions [42]. We assume that $\langle F(t) \rangle = 0$ and $\langle F(t)F(t') \rangle = F_o^2 e^{-\lambda |t-t'|}$, where λ^{-1} is the field correlation time and will be assumed to be much longer than any other time scale in the problem. The electron-phonon interaction term in the Hamiltonian couples the emitter excited state to virtual states that can be adiabatically eliminated to give the following effective electron-phonon interaction Hamiltonian for the process shown in Figure 2.17,

$$
H^{eff}_{e-ph} = c_2^{\dagger} c_2 \frac{1}{V} \sum_{\vec{k} \neq \vec{q}} G_{\vec{k},\vec{q}} a_{\vec{q}}^{\dagger} a_{\vec{k}}
\tag{2.13}
$$

where,

$$G_{\vec{k},\vec{q}} = \sum_{j\neq 2}\left[\frac{M^*_{j,\vec{q}}M_{j,\vec{k}}}{E_2 - E_j + \hbar\omega_{\vec{k}}} + \frac{M^*_{j,-\vec{k}}M_{j,-\vec{q}}}{E_2 - E_j - \hbar\omega_{\vec{q}}}\right] \tag{2.14}$$

If the electron-phonon interaction is via optical deformation potential then it is reasonable to assume that $G_{\vec{k},\vec{q}}$ will be large only when both $\vec{k},\vec{q}$ are small (near the center of the Brillouin zone) [43]. The ZPL emission spectrum $S(\omega)$ can be obtained from the relation [44],

$$\begin{aligned} S(\omega) &= \int dt\, e^{-i\omega t}\langle\sigma_+(t)\sigma_-(0)\rangle/\langle c_2^\dagger c_2\rangle \\ &= \int dt\, e^{-i\omega t}\langle c_2^\dagger(t)c_1(t)c_1^\dagger c_2\rangle/\langle c_2^\dagger c_2\rangle \end{aligned} \tag{2.15}$$

Using the cumulant expansion technique for the quantum propagator, the above expression gives,

$$S(\omega) \approx \int dt\, e^{-i[\omega-(E_2-E_1)/\hbar]t}\, e^{-\sigma^2 t^2/2} e^{-(\gamma+\gamma_{sp})|t|} \tag{2.16}$$

Here, $\sigma = |\alpha_2 - \alpha_1|F_o/\hbar$, $2\gamma_{sp}$ is the spontaneous emission rate, and the decoherence rate γ due to interaction with phonons is,

$$\begin{aligned} \gamma &= \frac{2\pi}{\hbar^2}\int d\omega D^2(\omega)|G(\omega)|^2 n(\omega)\,[n(\omega)+1] \\ &\approx \frac{2\pi}{\hbar^2} n(\omega_{op})\,[n(\omega_{op})+1]\int d\omega D^2(\omega)|G(\omega)|^2 \end{aligned} \tag{2.17}$$

$n(\omega)$ is the thermal boson occupation factor and $D(\omega)$ is the density of states function for the optical phonons. In the writing the result in Eq.(2.16), we have ignored the shift in the energy E_2 that results from phonon and photon interactions. We will assume that $\gamma >> \gamma_{sp}$ and that the dephasing is almost entirely due to interaction with phonons. The product $D^2(\omega)|G(\omega)|^2$ inside the integral is assumed to be peaked near the frequency ω_{op}. Eq.(2.16) shows that the ZPL spectral shape will be given by a Voigt function. The expression for γ shows that the temperature dependence of the dephasing rate is determined by the product $n(\omega_{op})\,[n(\omega_{op})+1]$, which gives a temperature dependence very different from any power law.

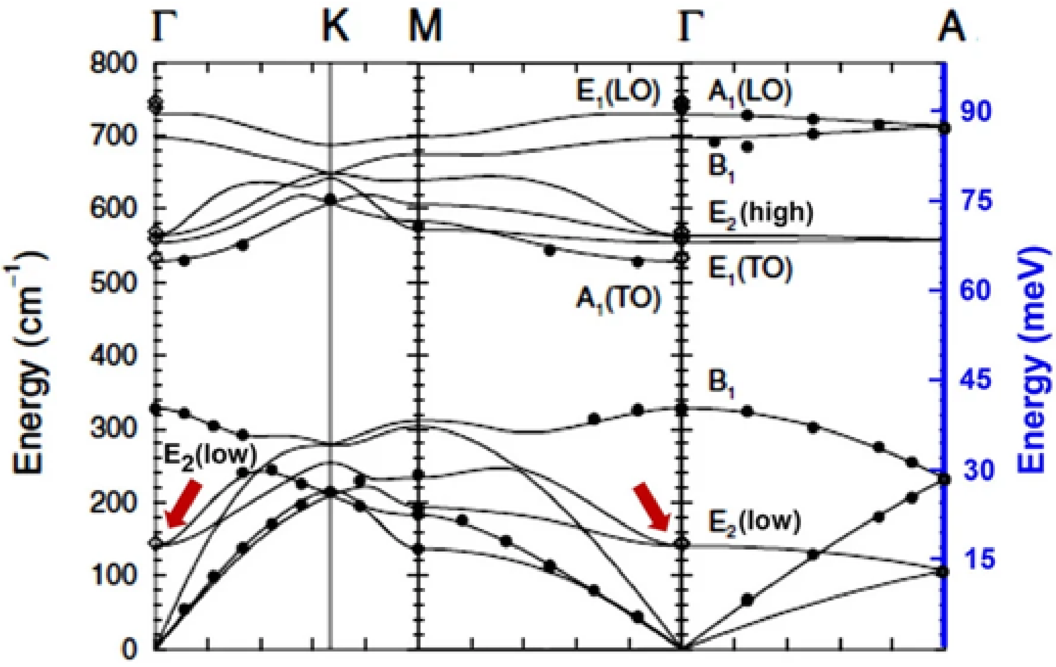

Figure 2.18: Phonon bands in wurtzite GaN are reproduced from the work of Ruf et al. [45]. The energy of the $E_2(low)$ optical phonon mode at the zone center matches the value obtained by fitting the model to the data.

Using the expression for the FWHM of $S(\omega)$ given earlier in Eq.(2.7) with the experimentally determined values of the Gaussian component f_G, and using the temperature dependence of γ given by the expression in Eq.(2.17) for the Lorentzian component $f_L = 2\gamma$, we can fit the measured FWHM of the ZPL, for both emitters E3 and E4, over the entire 10 K to 270 K temperature range with a root mean square error less than 0.05 meV provided we assume that $\hbar\omega_{op}$ equals 19 meV ± 0.5 meV. The fits obtained for $\hbar\omega_{op} = 19$ meV are shown by the solid lines in Figure 2.14. The excellent agreement between the data and the model begs the question if 19 meV is close to any one of the bulk optical phonons energies in GaN. Quite remarkably, the lowest energy Raman-active $E_2(low)$ optical phonon band in GaN has energy equal to $\sim$18 meV at the Γ-point of the Brillouin zone, as shown in Figure 2.18 [45]. Since, as stated earlier, $|G(\omega)|^2$ is expected to be large near the zone center, the experimental value of 19 meV for $\hbar\omega_{op}$ is reasonable and consistent with dephasing being caused by the coupling between the emitter and the bulk $E_2(low)$ optical phonons. The $E_2(low)$ optical phonon in GaN is known to be Raman active and couples strongly to the electronic states in the valence and conduction bands [46].

Finally, let us examine the equation 2.17 derived from our physical model.

$$\gamma \propto n(\omega_{op})\,[n(\omega_{op})+1] = \frac{e^{\frac{\hbar\omega}{K_bT}}}{(e^{\frac{\hbar\omega}{K_bT}}-1)^2} \tag{2.18}$$

γ increases with T monotonically and as T approaches zero, γ also approaches zero.

2.9 Discussions

The proposed physical model effectively explains the experimentally measured spectral data. Now, let us proceed with the discussion.

Since dephasing rate due to the process in Figure 2.17 is proportional to $n(\omega_{op})\,[n(\omega_{op})+1]$, the rate would have have been negligibly small, especially at low temperatures, if it were not for the fact that $\hbar\omega_{op}$ is also very small. Nitrides, and GaN in particular, are quite unique among wide bandgap semiconductors in that they possess optical phonon modes with low energies at the Brillouin zone center and these optical phonon modes are Raman-active and couple to the electronic states. Even if the emitter is coupled to other higher energy optical phonons, one would expect the lowest energy optical phonon with the largest thermal occupation to contribute the most to the dephasing rate via the mechanism shown in Figure 2.17 and this is also consistent with our data.

The coupling of the GaN defect SPEs to the low energy bulk optical phonon band is interesting because it suggests that the crystal lattice structure is not distorted by the defects to the extent that the bulk phonon modes become significantly modified in the vicinity of the defects. Furthermore, the presence of a sharp and strong ZPL at even room temperature, in contrast to the ZPLs of many other defects (e.g. NV^- centers in diamond) that are visible at only low temperatures, suggests that a localized optical phonon mode at the defect site is either absent or is very weakly coupled to the emitter (i.e. a small Huang-Rhys factor). The above characteristics are all consistent with the SPEs being substitutional impurity atoms or substitutional impurity-vacancy complexes.

But I should mention here that recently electron states localized at stacking faults and dislocations in the crystal have also been proposed as candidates for these SPEs [20]. Clearly, more work is needed to determine the nature of GaN SPEs.

CHAPTER 3

OPTICAL DIPOLE STRUCTURE AND ORIENTATION OF GAN DEFECT SINGLE PHOTON EMITTERS

This chapter is mainly based on Ref[26].

3.1 Fundamentals

In the previous chapter, we discussed that almost all single-photon emitters can be described as two-level systems. The transition from the excited state to the ground state results in the emission of a photon. Additionally, from quantum mechanics, we know that such transitions are often dipole transitions. Although this is not always the case, many experimental results in the literature support this. For dipole-like transitions, the transition matrix element can be written as:

$$M_{eg} = \langle g | \vec{\boldsymbol{d}} \cdot \vec{\boldsymbol{E}} | e \rangle \tag{3.1}$$

where where $|e\rangle$ represents the excited state, $|g\rangle$ represents the ground state, $\vec{\boldsymbol{d}}$ is the optical dipole moment and $\vec{\boldsymbol{E}}$ is the electric field.

Now, let us assume GaN defect emitters follow dipole transitions (which, as we will see by the end of this chapter, they do). It would then be natural for us to ask the following questions:

1. What is the dipole orientation? Is it in-plane, out-of-plane, or at an intermediate angle?

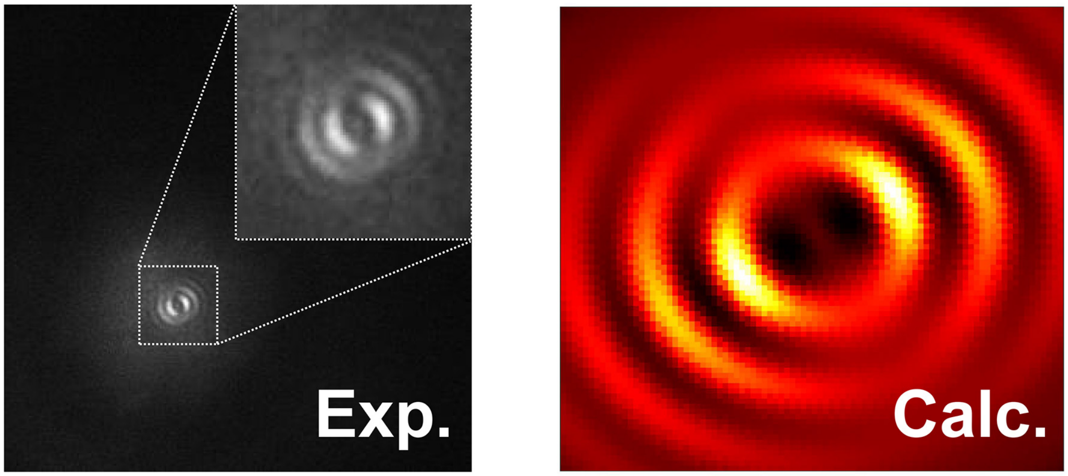

Figure 3.1: The comparison between the experimentally measured defocused image of a defect emitter (left) and the theoretically calculated dipole far-field radiation pattern (right) shows near-perfect agreement.

2. What is the correlation between the direction of the optical dipole moment and the crystal structure of GaN?
3. Is there any correlation between the emission wavelength and the dipole orientation?
4. What can we learn about the nature of these defects?

It can be seen that by studying the optical dipoles of these emitters, we can address the questions posed above, which is extremely valuable for both our understanding and the application of GaN emitters. For example, if we can determine the relationship between the orientation of these dipoles and the GaN crystal structure, we can infer the nature of these emitters to some extent. Additionally, when coupling these emitters into optical devices (such as waveguides or resonant cavities) for on-chip integration, it becomes essential to fully leverage their dipole properties. In this chapter, we will explore the optical dipole properties of GaN defect emitters in greater detail.

As a preview, we will use the defocused imaging technique to measure the far-field

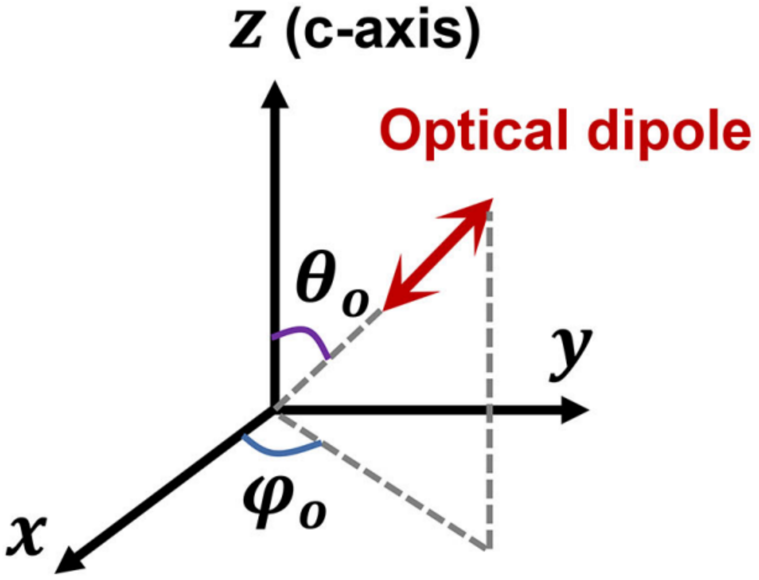

Figure 3.2: An optical dipole in space can be completely described by two angles: the in-plane angle φ_o and the out-of-plane angle θ_o. The spatial z-direction corresponds to the c-axis of the GaN crystal.

radiation patterns of GaN defect emitters, followed by Finite-Difference Time-Domain (FDTD) simulations to reconstruct the optical dipole orientation. This will result in Figure 3.1, which demonstrates the excellent agreement between experimental results and theoretical calculations.

As shown in Figure 3.2, consider a dipole in space. To fully determine its orientation, we need to know two angles: the out-of-plane angle (elevation angle) and the in-plane angle (azimuthal angle). From now on, we will assume that the sample is located in the x-y plane, with the surface normal direction (also the c-axis of the GaN crystal) aligned with the z-direction in Figure 3.2. We can readily see that the in-plane angle can be obtained by measuring the polarization patterns of the defect emitters. However, measuring the out-of-plane angle requires careful consideration.

As mentioned in the previous chapter, GaN is a high-refractive-index material, with a

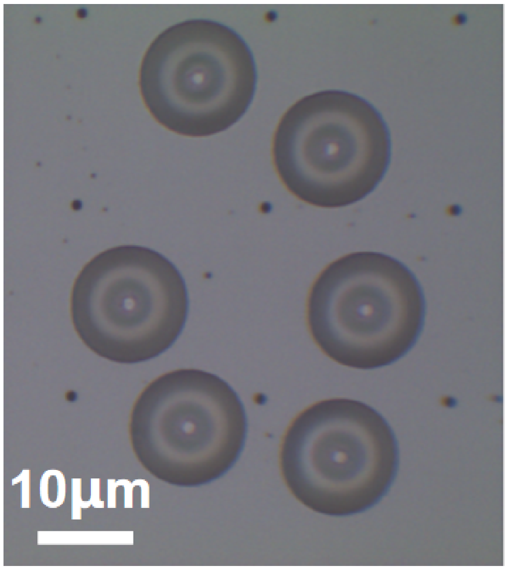

Figure 3.3: An optical microscopic image shows six fabricated solid immersion lenses, each with a diameter of 5 μm (hemispheres).

refractive index as high as 2.4 in the visible light range. There exists severe total internal reflection at the GaN/air interface. The large refractive index contrast between air and GaN reduces, in various ways, the accuracy with which the orientation of an optical dipole can be determined using defocused imaging. First, it decreases photon collection efficiency and the signal-to-noise ratio. Second, it leads to the formation of optical standing waves in the epitaxial layer, complicating the computational determination of the dipole orientation from the recorded data. Finally, the inability to collect photons emitted at large angles from the surface normal direction (due to total internal reflection) also degrades accuracy. To overcome these issues, we have introduced solid immersion lens fabrication using focused ion beam milling. Figure 3.3 shows an image of six fabricated solid immersion lenses acquired with an optical microscope.

However, to fully optimize these issues, we may need to explore alternatives beyond solely using solid immersion lenses. In microscopy, another common technique for increasing the numerical aperture is liquid immersion, such as water immersion and oil immersion. This approach is frequently utilized in biological experiments where super-resolution images of cells are desired.

In the previous temperature-dependent spectroscopy measurements, the sample was placed in a cryostat and cooled to low temperatures, which made it impossible to use an oil immersion objective lens. However, for the measurements of optical dipoles, all experiments are now conducted at room temperature, allowing us to fully utilize both oil and solid immersion lenses.

After introducing these fundamental concepts, the next section will discuss the optical systems required for measuring optical dipoles. In fact, there are various types of optical systems that can achieve our goal of determining the optical dipole. We will introduce these systems and discuss their advantages and disadvantages. Ultimately, we will choose a scheme known as defocused imaging.

3.2 Optical setups for measuring optical dipoles

The charm of optical measurements lies in their ability, through clever design, to measure nearly any physical quantity you wish to assess. Earlier, we introduced the confocal scanning microscope and the HBT interferometer used to measure single-photon emitters. Now, our goal is to measure the orientation of optical dipoles. We can employ various approaches to achieve this goal, such as the optical vortex technique [47], k-space imaging technique [48], and defocused imaging technique [49, 50, 51, 52]. Before introducing these experimental setups, we should clarify which dipole we are going to study. This depends on whether we are measuring the excitation end or the collection end.

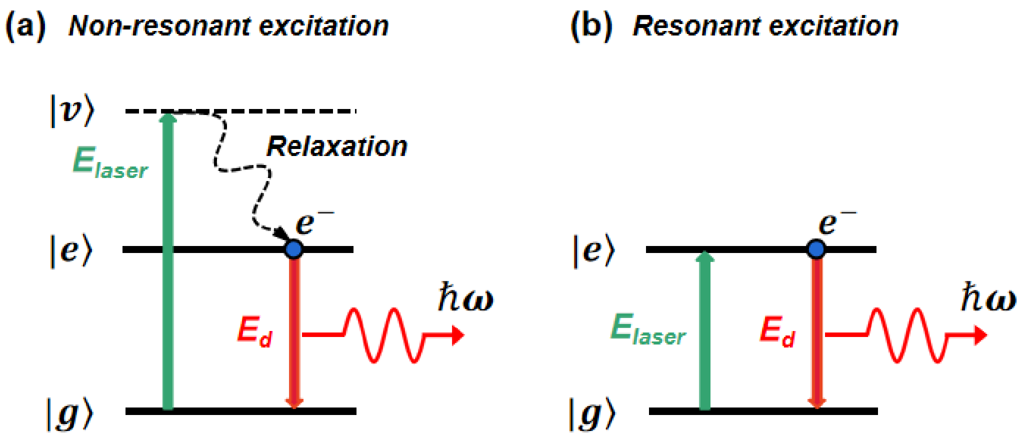

Figure 3.4: (a) Non-resonant excitation for a two-level system. In this scenario, the excitation laser energy is greater than the energy difference of the two-level system. As a result, the electron is excited to an intermediate state of higher energy, denoted as $|v\rangle$, and subsequently relaxes to the excited state $|e\rangle$ through non-radiative processes. (b) Resonant excitation for a two-level system. In this case, the laser energy is exactly equal to the energy difference between the two levels of the two-level system. This situation is commonly observed in Rabi oscillations.

As shown in the diagram 3.4, there are two excitation modes: non-resonant excitation and resonant excitation. For a two-level system, if the energy of the excitation laser is greater than the energy difference between the two levels (non-resonant excitation), the laser will cause the electron to transition from the ground state $|g\rangle$ to an intermediate state of higher energy $|v\rangle$. The electron then relaxes to the excited state $|e\rangle$ (usually through a non-radiative process; moreover, this non-radiative relaxation process typically does not preserve the previous dipole information) and subsequently transitions back to the ground state, emitting a fluorescence photon.

So, in the diagram, there are two dipole transition matrix elements: for the excitation end, it is the dipole transition between the ground state of the two-level system and the higher energy intermediate state ($M_{gv} = \langle g|\vec{\boldsymbol{d}} \cdot \vec{\boldsymbol{E}}|v\rangle$); while for the collection end, it is the dipole transition from the excited state to the ground state of the two-level system itself ($M_{eg} = \langle g|\vec{\boldsymbol{d}} \cdot \vec{\boldsymbol{E}}|e\rangle$). These two dipoles are usually not the same, so when measuring the dipole properties of a single photon emitter, it should be made clear which dipole is being studied. Typically, measurements at the excitation end focus on controlling the excitation laser (such as changing its polarization direction or using techniques like optical vortex), while measurements at the collection end focus on measuring the polarization properties or the far-field patterns of PL photons.

While the dipole at the excitation end can also, to some extent, demonstrate the nature of a single photon emitter, it ultimately depends on the choice of intermediate state levels and the excitation laser. In contrast, the dipole at the collection end directly characterizes the transition properties of the two-level system itself, making it more valuable for investigation. Since our excitation laser wavelength is 532 nm while the emission wavelength of GaN defect emitters is in the 600-700 nm range, this scenario belongs to the non-resonant excitation case. Later, we will see that, using the defocused imaging technique, we measure the collection end, i.e., the dipole properties of the transition of the two-level system itself.

For resonant excitation, as shown in Figure 3.4(b), the energy of the laser is exactly equal to the energy difference between the two levels of the two-level system. In this case, the matrix element for the upward transition caused by excitation is the same as the one for the downward transition caused by radiation. Thus, there is only one type of dipole in the diagram. However, since the laser wavelength is the same as the fluorescence wavelength, careful consideration is needed to filter out the laser at the collection end. The commonly used approach is cross-polarization, where the polarization direction of the laser is set perpendicular to the polarization direction of the fluorescence. This also requires the use of a polarizer with a very high extinction ratio. Another approach is to separate the spatial propagation directions of the laser and the fluorescence.

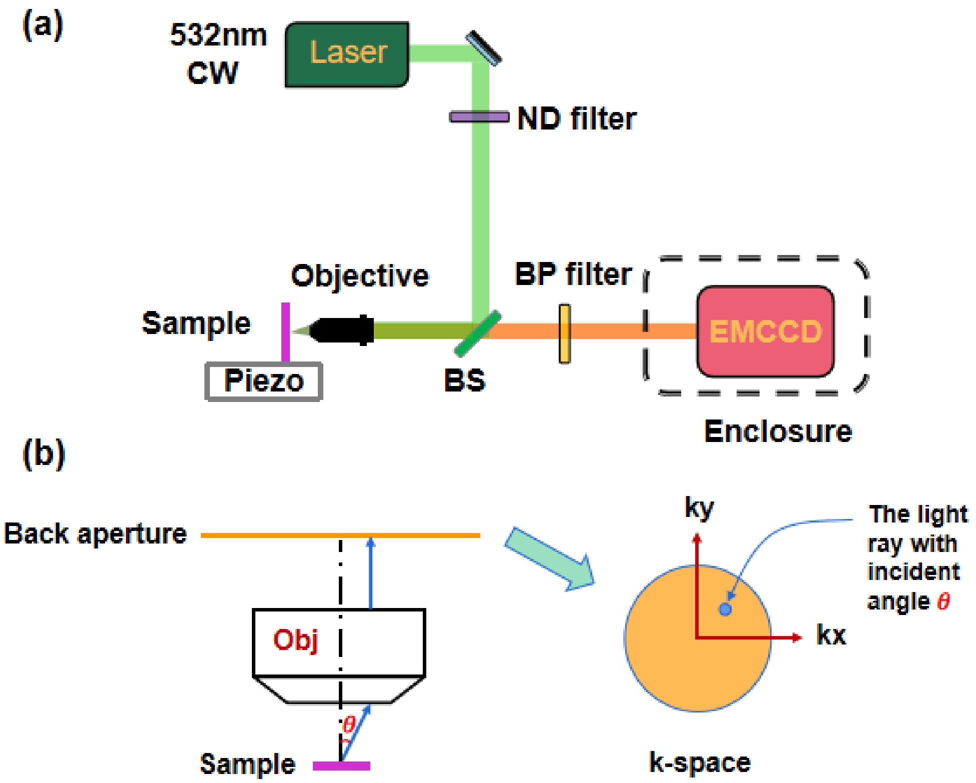

Figure 3.5: (a) The optical setup for the k-space imaging technique. A 532 nm laser is used to excite defect emitters, and the GaN sample is positioned in the focal plane of the objective lens. The EMCCD directly measures the collected PL light in k-space without any tube lens. (b) The PL light emitted from the sample is incident on the objective lens at some angle θ, corresponding to a specific point at the back aperture of the objective lens. Thus, the light distribution at the back aperture records all the k-space information of the emission, which can be used to infer the optical dipole orientation of the emitter on the sample.

For example, the laser can be incident on the sample along the z-direction, while the fluorescence signal is collected along the x-direction.

Now, let us introduce some specific experimental setups.

3.2.1 k-space imaging technique

Figure 3.5 shows the optical setup for k-space imaging. A 532 nm laser is focused onto the sample through a neutral density filter, which is used to control the laser power, and a dichroic beamsplitter. The sample is mounted on a piezo stage. The PL light emitted from the sample is collected by the same objective lens, then passes through a dichroic beamsplitter and a bandpass filter before being sent directly to an EMCCD camera. We typically use an EMCCD camera because the fluorescence signal from a single defect is usually very weak. Although its total brightness can reach several hundred kcps, when spread out over hundreds or even thousands of camera pixels, the number of photons received per pixel is very low. A traditional CCD camera may not provide enough signal-to-noise ratio, but the electron multiplication (EM) gain of an EMCCD camera can easily achieve this. Since there is no tube lens at the collection end before the EMCCD, this is not a traditional imaging system. In this case, the EMCCD camera measures k-space information.

As shown in Figure 3.5 (b), the fluorescence light incident on the objective lens at different angles will appear at different positions on the back aperture of the objective lens after being collimated by the lens. For example, the photoluminescence (PL) light from the sample, incident at an angle of θ in Figure 3.5 (b), will appear at the position indicated by the blue dot on the back aperture of the objective lens. Therefore, the back aperture records the k-space information of the emitted light, and measuring the distribution of photons on the back aperture is effectively measuring the angle-dependent emission pattern.

The advantage of the k-space imaging technique is that the setup is easy to implement; however, the cost is that reconstructing the orientation of dipoles from the k-space image is not as straightforward, although this can certainly be achieved with careful con-

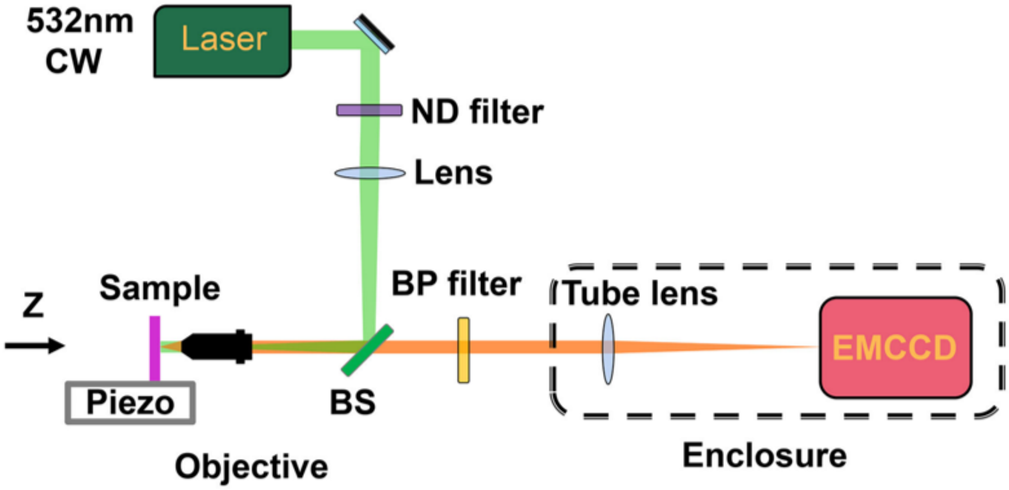

Figure 3.6: The optical setup for the defocused imaging technique involves a 532 nm laser used to excite defect emitters. A lens in the excitation path is employed to achieve wide-field illumination of the laser. This lens, along with the objective, forms a telescope system. The sample is mounted on a piezo stage, allowing it to be moved out of the focal plane of the objective lens, and the defocused image is recorded by the EMCCD.

sideration. Additionally, only one defect emitter can be studied at a time because the laser is focused on the sample to excite only one defect emitter. This limitation makes the technique less efficient, especially when a large number of defect emitters need to be studied to obtain statistical information.

In contrast, the defocused imaging technique is more straightforward and intuitive, making the reconstruction problem less complex. Additionally, it can be used to simultaneously study many defects in parallel due to its wide-field illumination and collection nature.

3.2.2 Defocused imaging technique

The setup for the defocused imaging technique is shown in Figure 3.6. A 532 nm laser, controlled for power by an ND filter, is directed onto the objective lens after passing through a lens and a dichroic beamsplitter. Compared to the previous k-space imaging setup, a lens has been inserted at the excitation end in this configuration. This lens, combined with the objective lens, forms a telescope system that collimates the laser before it strikes the sample. This ensures that the laser illuminates a large area on the sample, and that when the sample is later moved in the z-direction, the laser illumination area remains unchanged. The sample is still mounted on a piezo stage, allowing for precise control of the defocus depth. The PL light then passes through a dichroic beamsplitter and a bandpass filter before entering the EMCCD camera via a tube lens. As we can see, the presence of a tube lens at the collection end indicates that this is a typical imaging system. When the sample is in the focal plane of the objective lens, we are effectively imaging the defect emitter using this system. However, due to the extremely small size of the defect (possibly at the atomic scale), far below the diffraction limit, we can only observe a diffraction-limited spot on the EMCCD. When the piezo stage is moved to take the sample out of focus, the far-field radiation pattern of the defect emitter will be recorded by the EMCCD.

The reconstruction problem can be solved by numerically simulating the far-field radiation pattern of dipoles and comparing it with the defocused image obtained experimentally. Since the laser illumination area is large, typically ranging from tens to hundreds of square micrometers, this approach often allows us to observe the far-field images of many dipoles simultaneously. Correspondingly, it is necessary to increase the total laser power to ensure that the laser intensity per unit area is sufficiently strong to excite the defect emitters located within that area. The defocused imaging technique has

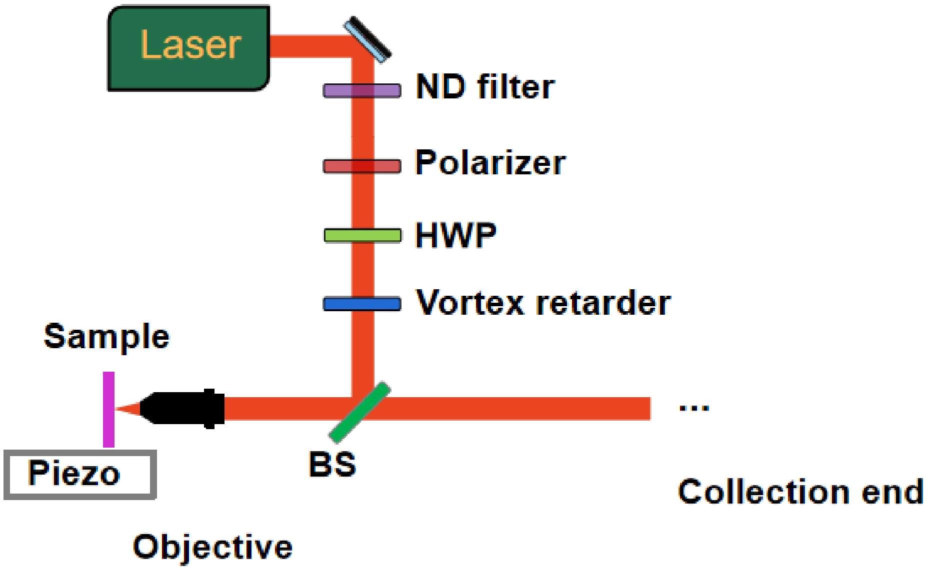

Figure 3.7: The excitation part of the optical setup for the optical vortex technique involves the laser passing through a polarizer and a half-wave plate. The vortex retarder then converts it into vortex light, which is focused onto the sample by the objective lens to excite the defect emitter.

been previously utilized to determine the optical dipole orientation in colloidal quantum dots[53, 54, 55] and dye molecules [56, 57].

3.2.3 Optical vortex technique

Sometimes in the literature, the optical vortex technique is used in the study of dipoles. The typical setup is shown in Figure 3.7. The figure only shows the excitation end to emphasize the main point. After passing through the ND filter, the laser needs to pass through a polarizer to ensure good linear polarization characteristics. It then passes through a half-wave plate to rotate the polarization direction of the laser. After that, the vortex retarder converts it into vortex light, which is focused onto the sample by the objective lens to excite the defect emitter. Due to the nature of vortex light, laser beams with different polarization components interact with dipoles oriented in different directions, allowing us to determine which dipoles are excited and thereby infer the orientation of the dipoles.

However, it should be noted that if the laser wavelength is different from the fluorescence wavelength (non-resonant excitation), then the dipoles being studied are at the excitation end (the transition matrix element is $M_{gv} = \langle g|\vec{\boldsymbol{d}} \cdot \vec{\boldsymbol{E}}|v\rangle$, where $|v\rangle$ represents the intermediate level shown in Figure 3.4 (a)), not the dipoles of the two-level system itself.

From the above discussion, it is clear that there are different techniques available for use here. However, our goal is to study the optical dipole properties of the two-level system itself, so we will focus on the collection end and choose the defocused imaging technique to study GaN defect emitters. After understanding the basic principles of defocused imaging, it is time to present and discuss the experimental results.

3.3 Experimental results

If we were to design an experimental project to investigate the optical dipole properties of GaN defect emitters from scratch, the first question we should ask as experimental physicists is: What are the necessary experiments we need to conduct?

Certainly, there are four essential experiments that must be conducted. They are: the PL spectra of GaN defect emitters, their polarization patterns, their $g^{(2)}$ functions, and, most importantly, their defocused images. Among these, the spectrum measurement is used to determine their emission wavelength, the $g^{(2)}$ function measurement is used to verify whether they are indeed single-photon emitters, and the polarization and defocused image measurements are used to determine their dipole orientations. Additionally, we need to measure multiple emitters to obtain statistical information and study the correlations between the aforementioned properties.

These experiments require the use of two optical setups. One is the defocused imaging setup mentioned in the previous section, which is used solely to acquire the defocused images. The other is the confocal scanning microscope introduced in Section 2.4, which is used for the measurement of $g^{(2)}$ functions, polarization patterns, and PL spectra. Figure 3.8 shows the main experimental results, which consist of four types of data from five different defect emitters labeled E1 to E5. All experiments were conducted at room temperature.

Figures 3.8 (a)-(e) show the radiation patterns (defocused images) of emitters E1 through E5, integrated with solid immersion lenses (emitters E2 and E3 share the same solid immersion lens). The boundary of the solid immersion lens is also clearly visible in the images. The defocusing was achieved by moving the piezostage approximately 1 μm away from the focal plane of the objective. The EMCCD accumulated 20 frames with an electron multiplying (EM) gain of 500, with an exposure time of 0.1 s for each frame. All SPEs exhibit a two-lobe radiation pattern, which, as shown later, is consistent with a single optical dipole oriented almost perpendicular to the crystal c-axis.

Figures 3.8 (f)-(j) show the corresponding polarization patterns obtained directly using a polarizer. The polarization data in each case can be fitted with the function $\cos^2(\varphi - \varphi_o)$, which is consistent with light polarized linearly in the direction φ_o, in agreement with the measured radiation pattern. Here, $\varphi = 0^\circ$ corresponds to the direction perpendicular to the wurtzite m-plane. The text in green in Figures 3.8 (f)-(j) indicates the in-plane angles φ_o of the dipoles, as obtained by fitting the polarization patterns with the function $\cos^2(\varphi - \varphi_o)$.

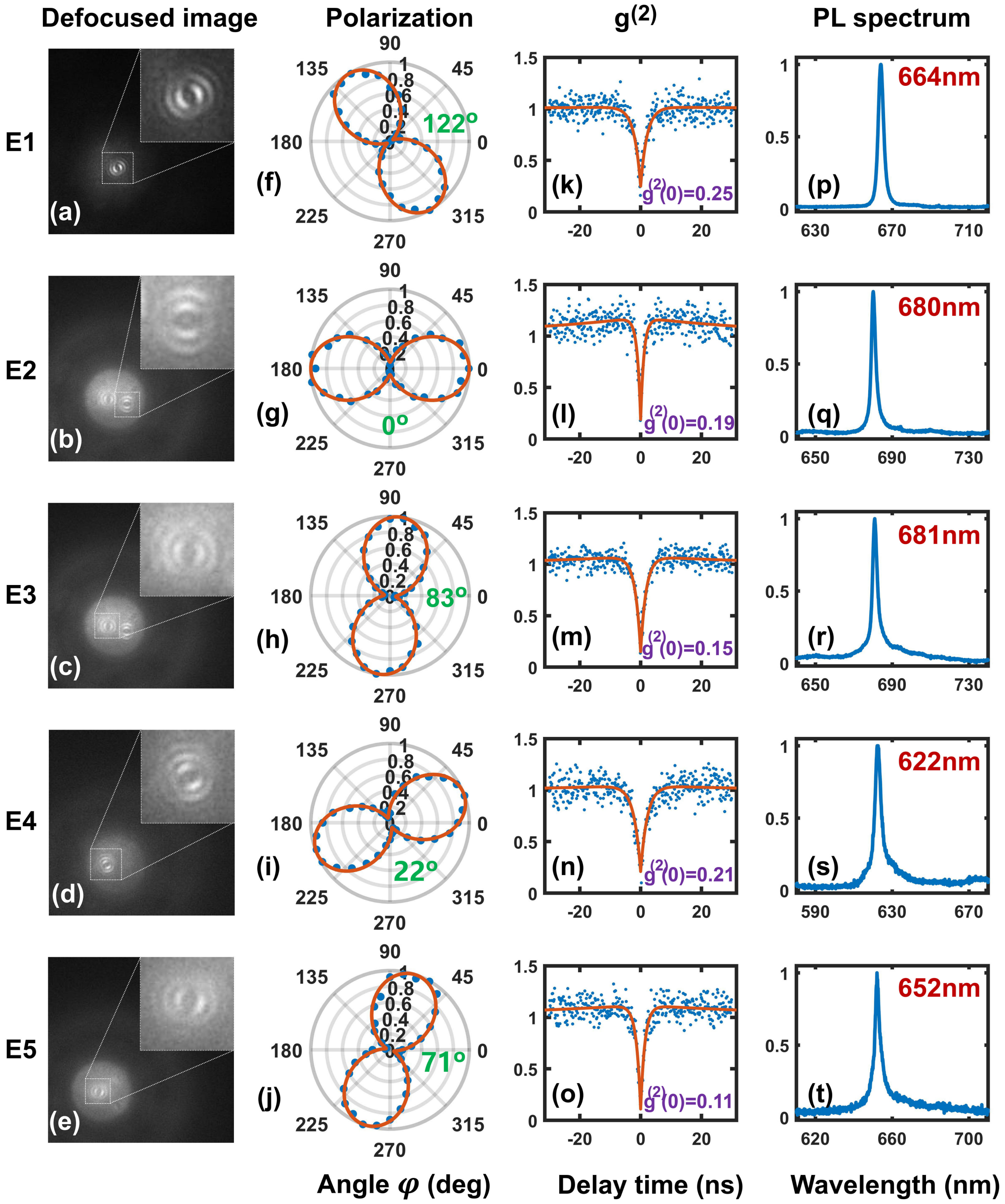

Figure 3.8: (a)-(e) Defocused images of light emission from five different SPEs, E1 through E5, integrated with solid immersion lenses are shown. Insets show the zoomed-in radiation patterns of each SPE. (f)-(j) Measured polarization patterns of the emitted light are plotted as a function of the in-plane angle φ. $\varphi = 0^\circ$ corresponds to the direction perpendicular to the wurtzite m-plane. The text in green shows the in-plane angles φ_o of the dipoles as obtained by fitting data with the function $\cos^2(\varphi - \varphi_o)$. (k)-(o) Measured second order correlation functions are plotted. (p)-(t) Measured PL spectra are plotted. All measurements were performed at room temperature.

Figures 3.8 (k)-(o) show the second-order correlation functions ($g^{(2)}$) measured using the time-tagged time-resolved (TTTR) mode of the correlator (MultiHarp150 from Picoquant) instrument. The small values (below 0.5) of $g^{(2)}(0)$ confirm that all defects are SPEs.

The measured emission spectra are plotted in Figures 3.8 (p)-(t). All single-photon emitters (SPEs) exhibit sharp and strong zero-phonon lines in the 600-700 nm wavelength range at room temperature. Although the emission wavelengths vary, all emitters shown in Figure 3.8 display similar defocused radiation patterns and polarization patterns.

Figure 3.9 shows the defocus depth-dependent emission patterns for emitter E1 from Figure 3.8. The defocus depth refers to the distance between the emitter and the focal plane. When the defect emitter is in the focal plane, a diffraction-limited spot is observed, as shown in the top left sub-figure. This occurs because the size of the defect emitter is much smaller than the diffraction limit, preventing the optical microscope from resolving it.

As the defocus depth increases, the image evolves from the diffraction-limited spot to the two-lobe far-field radiation pattern shown in the bottom right sub-figure. Clear far-field radiation patterns can be observed when the defocus depth is around 1 μm. However, as the defocus depth increases beyond 1 μm, the total amount of collected light decreases, and the recorded radiation pattern gradually fades into the noise floor.

After obtaining the experimental data described above, we are more than 90% confident that these defect emitters correspond to in-plane dipoles. However, a rigorous approach involves assuming a specific orientation for the dipole, using electromagnetic simulation (FDTD method) to calculate the theoretical radiation pattern, and then com-

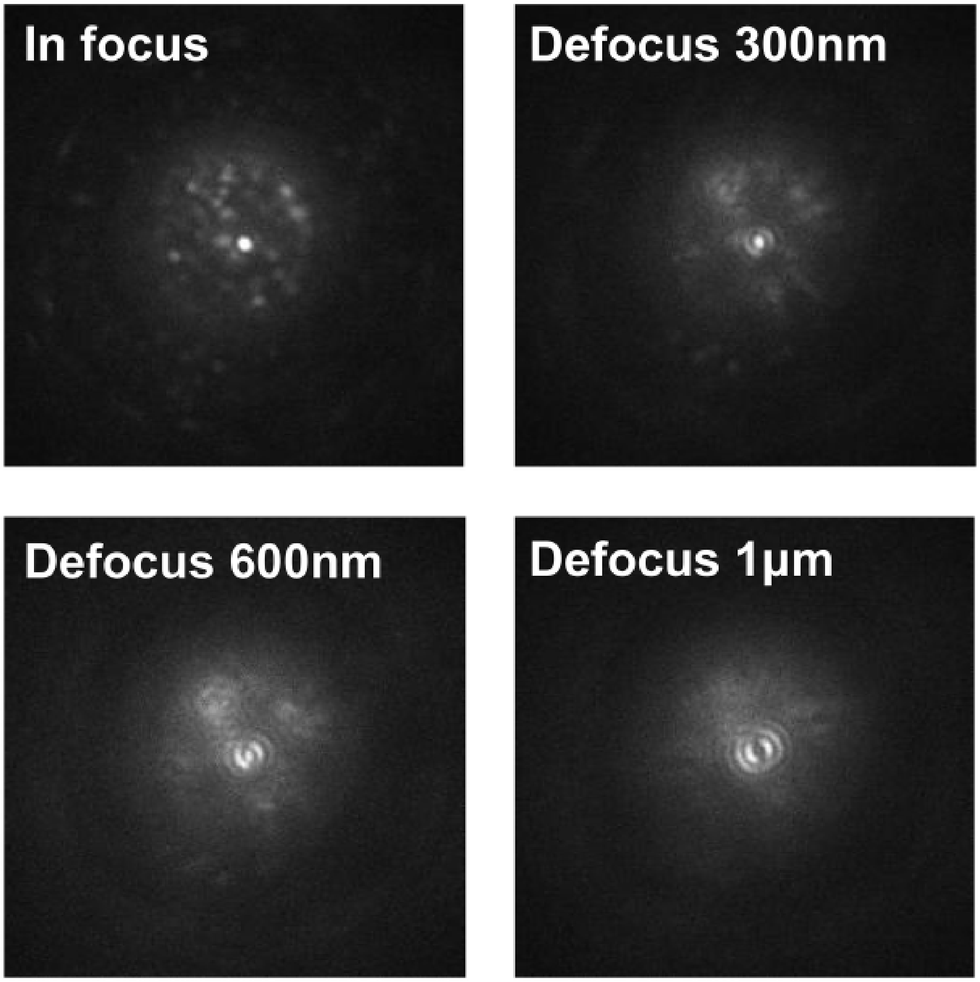

Figure 3.9: The defocused images of the defect emitter E1 from Figure 3.8 are shown for different defocus depths. The defocus depth refers to the distance between the emitter and the focal plane.

paring it with the experimental results to draw a conclusion. This will be precisely what we do in the next section.

3.4 Simulations

3.4.1 Simulation setup and results

The determination of the optical dipole angles θ_o from the defocused images requires analytical or computational modeling. We employ the finite-difference time-domain (FDTD) technique to compute the radiation patterns for different dipole angles θ_o and compare them with the measurements. Figure 3.10(a) shows the model structure used in the computations. A 4 μm thick GaN layer (refractive index $n = 2.37$) is sandwiched between a 430 μm thick sapphire substrate ($n = 1.76$) and a 150 μm thick immersion oil layer ($n = 1.51$). (Note that we use an oil immersion objective lens for the defocused imaging technique.) The solid immersion lens is a hemisphere with a diameter of 5 μm. The 430 μm sapphire layer and the 150 μm immersion oil layer can be considered as far-field regions, since their dimensions are both much larger than the defect emission wavelength (600-700 nm in free space). An optical dipole is placed in the center of the solid immersion lens, and the angle θ_o of the dipole is varied while calculating the radiation patterns in the far field.

Figure 3.10(b) shows the computed far-field radiation patterns for different representative angles θ_o assuming that $\varphi_o = 0°$ and that the dipole emission wavelength is 680 nm. When $\theta_o = 90°$, and the dipole is oriented perpendicular to the c-axis, the radiation pattern has two-fold rotation symmetry (group C_{2v}) with respect to the c-axis, with reflection planes at $\varphi = 0°$ and $\varphi = 90°$. When $\theta_o = 0°$, and the dipole is oriented along the c-axis, the radiation pattern has complete rotation symmetry (group $O(2)$). However, the power radiated in the upward direction is extremely small in this case. For all other values of θ_o, the radiation pattern has lower symmetry (group C_{1v}) with a single reflection plane at $\varphi = 0°$. As shown in Figure 3.10(b), the lowering of symmetry in the radiation

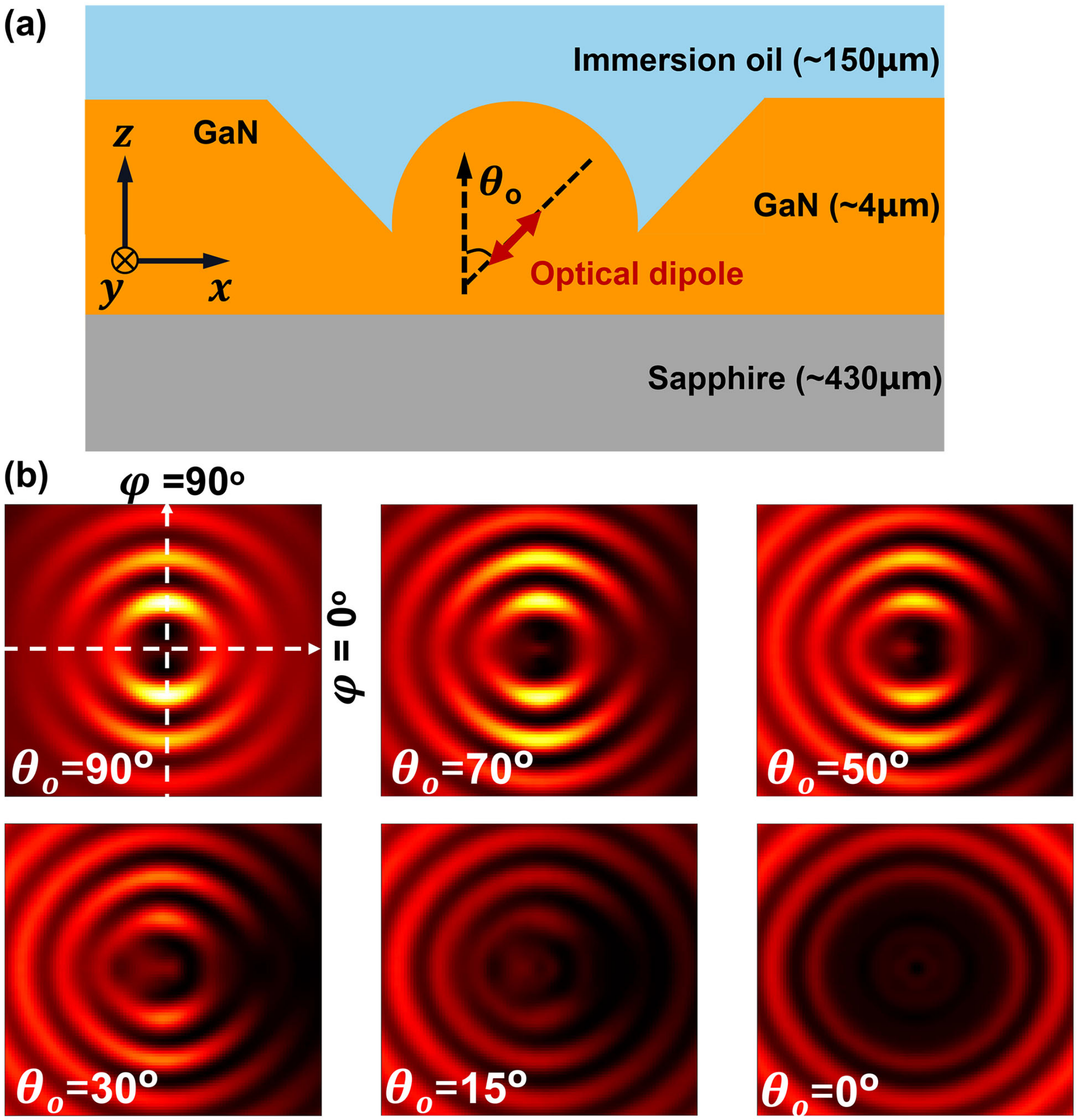

Figure 3.10: The structure used in numerical (FDTD) computations consists of a 4 μm GaN layer sandwiched between an oil immersion layer and a sapphire substrate. The diameter of the solid immersion lens is 5 μm. (b) The calculated far-field radiation patterns from the dipole are plotted for different out-of-plane dipole angles θ_o. The radiation pattern exhibits C_{2v} symmetry for $\theta_o = 90°$, $O(2)$ symmetry for $\theta_o = 0°$, and C_{1v} symmetry for all angles in between. Since the radiated power in the vertical direction is also a function of the dipole angle, the contrast is adjusted in the figures shown for better visibility as follows: ($\theta_o = 90°$, contrast 1X), (70°, 1X), (50°, 2X), (30°, 3X), (15°, 5X), and (0°, 10X).

pattern from C_{2v} to C_{1v}, as the dipole angle is reduced from $\theta_o = 90^\circ$, makes the pattern more asymmetric with respect to the $\varphi = 90^\circ$ plane. The accuracy with which the dipole angle θ_o can be determined from the measured radiation pattern depends on the exact and detailed comparison between data and theory and also on the signal-to-noise ratio in the measured data. As shown in Figures 3.8(a)-(e), the measured radiation patterns of all SPEs have approximately two-fold C_{2v} symmetry, which implies that all SPEs are oriented perpendicular (or almost perpendicular) to the c-axis (i.e., $\theta_o = 90^\circ$). However, noise in our measurements can be used to put an error margin on the value of θ_o. By comparing the measurements with the computed images, and taking into account the noise in our data, we estimate that θ_o for all SPEs satisfies $70^\circ < \theta_o < 110^\circ$ irrespective of the wavelength and the in-plane orientation of the SPE dipole. This range specifies the noise-limited error margin in our determination of θ_o.

Other factors that can affect the determination of the dipole angle θ_o include the following: i) the emission wavelength of a SPE can be different from 680 nm, the wavelength used in our computations, and ii) in actual samples, SPEs are not exactly located at the location assumed in the computations (see Figure 3.10(a)). Points whose distance r from a dipole satisfy $r >> \lambda/(2\pi n) \approx 50$ nm, where n is the refractive index of GaN, constitute the radiation far-field region. If a dipole is away from all interfaces by at least 1 μm ($\sim$20 times $\lambda/(2\pi n)$), and the lens structure does not favor the formation of strong standing waves, one can expect that the recorded radiation pattern will not get much affected by the exact location of the dipole inside the lens. The SPEs studied in this work were selected such that they were at least a micrometer away from the top and bottom interfaces of the GaN epitaxial layer to avoid surface contamination and interface defects. Furthermore, the offsets between the centers of the solid immersion lenses and the SPEs due to fabrication errors were generally less than 1 μm. This ensured that all interfaces were in the far-field regions of the SPEs. Numerical computations indeed show that when the above conditions are fulfilled, the effect of the location of the dipole on the radiation pattern and on the accuracy with which θ_o can be determined is small enough to be almost negligible compared to the accuracy limitation imposed by the presence of noise, as discussed above. This can be seen in our experimental data as well (Figures 3.8(a)-(e)) where the approximate C_{2v} symmetry is seen for all SPEs irrespective of their exact location within the lens. Similarly, numerical computations show that the effect of variation in the emission wavelength of a SPE in the 600-700 nm range on the radiation pattern is small enough to be ignored.

3.4.2 The error margin in the estimation of the angle θ_o of an optical dipole

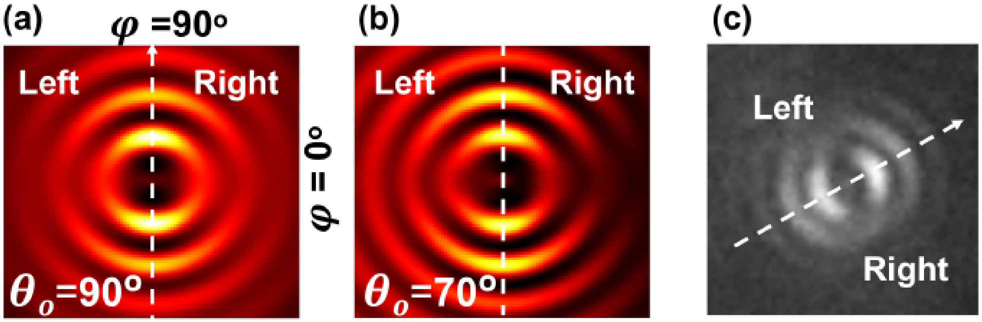

Figure 3.11: Comparison between calculated far field emission patterns and measured defocused image. (a)-(b) Calculated far field radiation patterns with $\theta_o = 90°$ and $\theta_o = 70°$ respectively (same as Figure 3.10 (b)). (c) Defocused image of emitter E1 (same as Figure 3.8 (a))

The computed emission pattern for $\theta_o = 90°$, shown in Figure 3.11 (a), has reflection symmetry with respect to the axis perpendicular to the dipole axis (vertical dashed line). But if $0° < \theta_o < 90°$, the emission pattern is not symmetric with respect to the axis perpendicular to the dipole axis, as shown in Figure 3.11 (b) for $\theta_o = 70°$. This asymmetry can be quantified by the integrated intensity in the left and right halves of the image. We use a parameter ΔI defined as follows,

$$\Delta I = \frac{I_L - I_R}{I_L + I_R} \tag{3.2}$$

where I_L and I_R are the integrated signals in the left and right halves of the image, respectively, as recorded by the EMCCD detector. In general, ΔI measured in experiments can be expressed to a good approximation as,

$$\Delta I_{Measured} = \Delta I_{\theta_o} + \Delta I_{Dipolelocation} + \Delta I_{Noise} \tag{3.3}$$

where ΔI_{θ_o} is the asymmetry because $0^\circ < \theta_o < 90^\circ$. ΔI_{θ_o} is zero when $\theta_o = 90^\circ$ or when $\theta_o = 0^\circ$. ΔI_{Noise} is the contribution from noise (background noise, detector dark current noise, detector readout noise, etc) and $\Delta I_{Dipolelocation}$ is the contribution if the dipole is not located right in the center of the SIL. These aforementioned contributions to $\Delta I_{Measured}$ are additive to the first order. $|\Delta I_{Noise}|$ can be estimated from the noise specifications of the EMCCD detector and the detected total photon count rate in the experiments. $|\Delta I_{Noise}|$ is estimated to be less than 8 percent. Numerical computations show that $|\Delta I_{Dipolelocation}|$ is smaller than 3 percent provided the defect emitter is not off-center by more than 1 μm in the lateral direction. The experimentally obtained quantity $|\Delta I_{Measured}|$ for emission patterns recorded in this work varies greatly from image to image but is always less than 10 percent. Therefore, even in the worst-case scenario, $|\Delta I_{\theta_o}| < 21$ percent. For $\theta_o = 70^\circ$ (or $\theta_o = 110^\circ$), ΔI_{θ_o} is $\sim$21 percent from theoretical modeling (shown in Figure 3.11 (b)). Therefore, we conclude that $70^\circ < \theta_o < 110^\circ$ as stated earlier.

We have completed the experimental measurements and theoretical simulations. Next, we aim to understand the correlation between the dipole properties and the GaN crystal structure. This requires measuring multiple emitters to gather statistical information.

3.5 Statistics and discussion

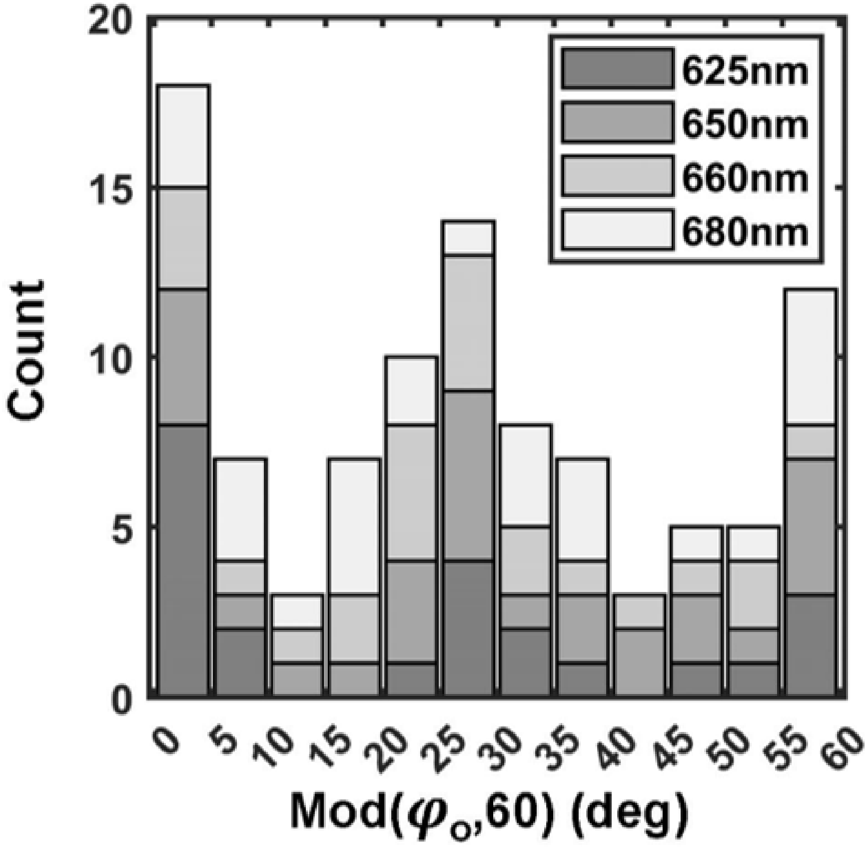

Figure 3.12: The distributions of in-plane optical dipole angles $mod(\varphi_o, 60^\circ)$ for different wavelength SPEs are shown. Two distinct groups are observed, one is centered around 0° (or 60°), while the other is centered around 30°.

In the previous section, we observed that the out-of-plane angle of the optical dipoles is nearly 90 degrees (indicating the dipole is in the plane), while the in-plane angles vary across a relatively large range. So we investigate the distribution of the in-plane angle φ_o

of the SPEs and examine if any correlations exist between these angles and the underlying crystal structure. Since the wurtzite crystal structure has an in-plane 3-fold rotation symmetry and the linearly polarized light from the SPEs has a 2-fold symmetry, we classify all measured SPEs according to the angle $mod(\varphi_o, 60^\circ)$. The resulting distribution is plotted in Figure 3.12 for close to 100 emitters with different emission wavelengths in the 600-700 nm range. The four wavelengths shown are the center wavelengths of the bins in which SPEs with emission wavelengths close to the bin center wavelength (within ± 5 nm) were placed in making the plot. Several interesting features are visible in this plot. First, SPEs of all wavelengths exhibit very similar angular distributions. Second, the angular distributions are fairly wide. Third, the angular distributions show two distinct peaks at angles close to 0° (or 60°) and 30°. These angles correspond to the directions between the nearest Ga-N bonds (labeled as Group 1) and the nearest Ga-Ga (or N-N) directions (labeled as Group 2) in the wurtzite crystal structure of GaN, as depicted in Figure 3.13 (a).

The information obtained via defocused imaging about the optical dipole orientation of GaN SPEs in the 600-700 nm wavelength range can help identify the nature and origin of the SPEs. First, a single substitutional impurity or a vacancy at either the Ga or N site is expected to have C_{3v} point group symmetry with the c-axis as the 3-fold axis of rotation. The C_{3v} group has two one-dimensional representations, A_1 and A_2, and one two-dimensional representation E. Optical transitions are allowed between states with the same A_1, A_2 or E symmetry, and between states with A_1 or A_2 symmetry and E symmetry. In all of these cases, linearly polarized light emission with a single optical dipole axis, as observed in our measurements, is not possible (unless the double degeneracy between the states with E symmetry is somehow lifted). Next, we consider impurity/vacancy complexes of the form $X_N Y_N$, $X_{Ga} Y_{Ga}$, $X_{Ga} Y_N$, $X_{Ga} Y_i$, and $X_N Y_i$ (see Figure 3.14). X and Y stand for an impurity/substitutional atom or a vacancy (if on a

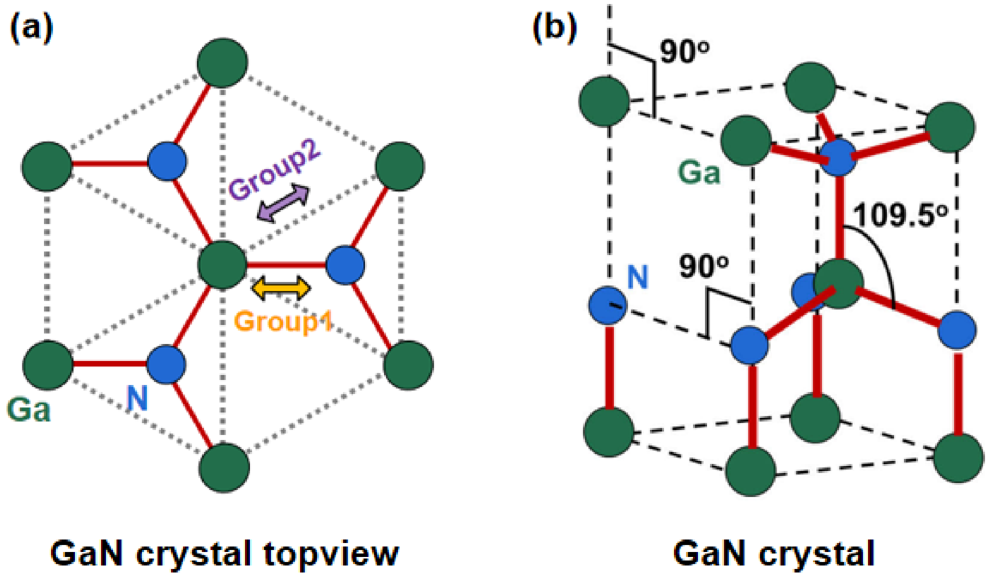

Figure 3.13: (a) Two groups of dipoles can be seen in the GaN crystal structure (topview), Group 1 corresponds to the directions between the nearest Ga-N bonds (0° or 60°), while Group 2 corresponds to the nearest Ga-Ga (or N-N) directions (30°) in the wurtzite crystal. (b) GaN wurtzite crystal structure (side view).

lattice site) and the subscript i stands for an interstitial. If one assumes that the optical dipole moment is along the axis of the X-Y complex, then this family of defects could explain the measured dipole orientations (angles θ_o and φ_o) of the SPEs (note the 109.5° and 90° angles between the c-axis and the nearest Ga-N bonds and the nearest Ga-Ga (or N-N) directions, respectively, in Figure 3.13(b)). Several first principles studies have been reported for point defects in GaN [58, 59, 60, 61, 62, 21]. Point defects in which one of X and Y is carbon or iron and the other is carbon, hydrogen, oxygen, or a vacancy are promising candidates as computations have shown these point defects to have relatively small formation energies and their computed ZPL photon emission energies are in the neighborhood of the observed emission energies [58, 59, 60, 61, 62]. However, computed optical dipole orientations have not been reported in the literature for all of these defects. In the case when both X and Y are carbon atoms, the optical dipoles are

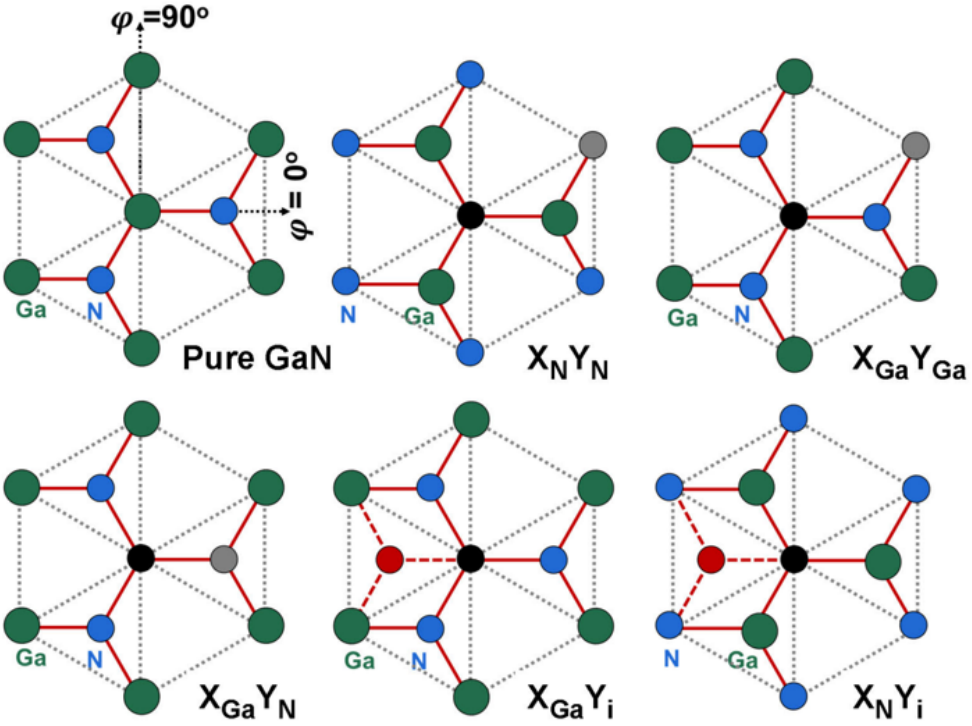

Figure 3.14: Impurity/vacancy complexes of the forms $X_N Y_N$, $X_{Ga} Y_{Ga}$, $X_{Ga} Y_N$, $X_{Ga} Y_i$, and $X_N Y_i$ are depicted. X and Y stand for an impurity atom or a vacancy (if on a lattice site) and the subscript i stands for an interstitial (shown in red). Substitutional impurities and vacancies are shown in black or gray. The leftmost figure in the top row shows a pure GaN crystal (top view).

known to be oriented along the X-Y axis [58]. The experimentally observed departure from exact 0° and 30° values of $mod(\varphi_o, 60^\circ)$ could be due to the fact that the presence of impurity atoms causes lattice distortion, and therefore, the actual positions of the atoms are not expected to be as shown in Figure 3.14 [58, 59, 62]. Supporting evidence for these defects also comes from secondary ion mass spectrometry (SIMS) data. The semi-insulating GaN samples used in this work were iron doped and the iron concentration measured by SIMS was $\sim 7 \times 10^{17}$ /cm^3. SIMS also showed carbon, hydrogen, and oxygen concentrations of $\sim 5 \times 10^{16}$ /cm^3, $\sim 3 \times 10^{17}$ /cm^3, and $\sim 10^{16}$ /cm^3, respectively. Whereas the defects mentioned above are all extrinsic, recently an intrinsic antisite-vacancy complex $N_{Ga} V_N$ (also of the type $X_{Ga} Y_N$) has also been suggested as a possible candidate for SPEs with emission wavelengths close to 625 nm [21]. I should mention here that the SPE density in our samples is less than 10^{10} /cm^3. This means that impurity atoms in concentrations much lower than the SIMS detection limit could also underlie the observed SPEs in our samples.

CHAPTER 4

SPECTRAL DIFFUSION OF GAN DEFECT EMITTERS

This chapter is mainly based on Ref[29].

4.1 Fundamentals

In the previous two chapters, we discussed the dephasing properties and optical dipole characteristics of GaN defect emitters, all related to the two-level system itself. Now, we will shift our focus from the defect emitters to their surrounding environment. Do you remember the spectral broadening issue in the dephasing mechanisms discussed in Chapter 2? There, we observed that the actual spectrum (FWHM of about 10 meV) is broadened by a factor of ten thousand compared to the ideal spectrum (FWHM $\sim \mu$eV, determined by the lifetime) at room temperature. Even in a low-temperature environment (10 K), the linewidth of the actual spectrum is approximately 1 meV, which is still one thousand times broader than the ideal case. We have also noted that the tenfold broadening from 1 meV to 10 meV is caused by defect-phonon coupling, which is temperature-dependent, and that the line shape follows a Lorentzian function.

However, at low temperatures, the PL spectrum saturates to a Gaussian line shape with a linewidth of around 1 meV, corresponding to the remaining thousandfold broadening. This is much more pronounced than the dephasing caused by phonon coupling. In Chapter 2, we treated this term as a constant and briefly mentioned that this Gaussian contribution arises from the spectral diffusion effect. Now, we should delve deeply into this aspect to gain insight into its significance. Before studying any scientific problem, the first thing to clarify is always the concepts. Here, the question is: what is spectral diffusion? As the name suggests, it refers to the change in the emission spectrum of defect emitters over time in the wavelength (or energy) domain, resembling a spread from one wavelength to another. This phenomenon usually occurs due to fluctuations in the local electric environment around the defect emitter[63].

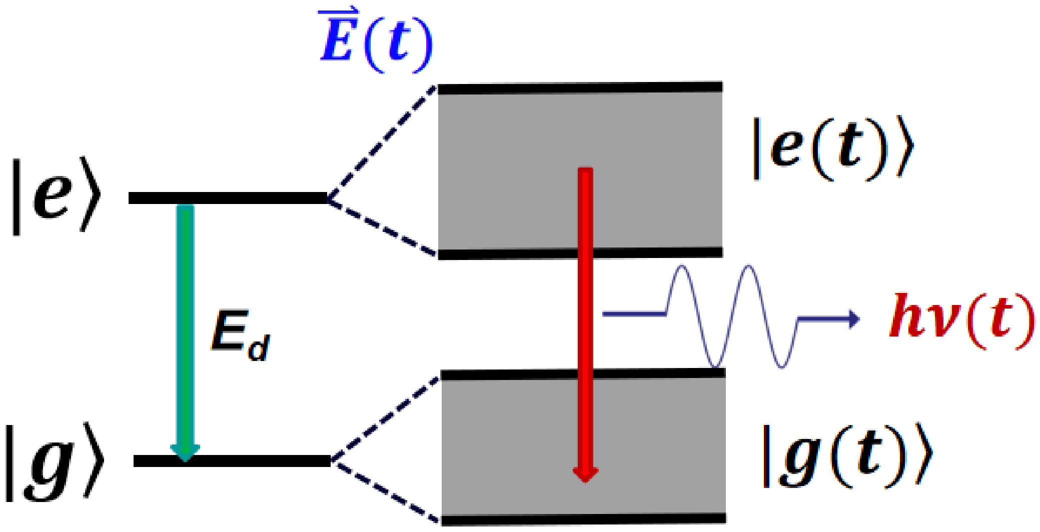

Figure 4.1: If there is a time-varying external electric field coupled to the two-level system due to the Stark effect, the ground and excited state energies will also change over time. As a result, the energy of the emitted photons will likewise change, a phenomenon known as spectral diffusion.

As shown in Figure 4.1, we assume the defect emitter is a two level system, as we have done many times before. In the absence of an external electric field, the ground state is $|g\rangle$, and the excited state is $|e\rangle$. The transition between them will emit single photons, which will have exactly the same energy (within the limits of energy-time uncertainty).

If there is an external time varying electric field, meaning the defect emitter experiences an electric field that varies rapidly with time and has a mean value of zero (only the AC component exists), the presence of the Stark effect introduces an additional term in the Hamiltonian, known as the Stark shift. This causes the eigenenergies of the ground and excited states to change over time, as illustrated in Figure 4.1.

The figure seems to suggest that the ground state and excited state split into two energy bands, but this is not the case in reality. At any given moment, there is only a single ground state level and a single excited state level; however, these two levels fluctuate over time. The illustration in the figure indicates the range of energies for the ground state and excited state over an extended period. Consequently, the energy (or wavelength) of the emitted photons also changes over time, as the energy of the emitted photon at any moment corresponds to the energy difference between the excited state and the ground state at that moment.

From Figure 4.1, it is clear that the energy of the emitted photons is no longer a fixed value (intrinsic energy) but rather a range that corresponds to the fluctuation range of the ground state and excited state energy levels under the external time dependent electric field. This is the concept of spectral diffusion, which is the main reason for limiting the generation of indistinguishable photons at low temperatures. So, where does this time varying external electric field come from? In fact, this is not due to the intentional placement of electrodes or the application of any voltage (if we did, that would be a separate research topic concerning the Stark shift), but rather because GaN samples are typically not pure crystals. They contain many defects, such as impurities, donor atoms, acceptor atoms, and surface defects.

Figure 4.2 shows a schematic diagram of our sample, where a 4 μm thick GaN epitaxial layer is grown on a sapphire substrate. A solid immersion lens with a diameter of 5 μm is fabricated using focused ion beam etching, and a defect emitter is located at the center of the lens.

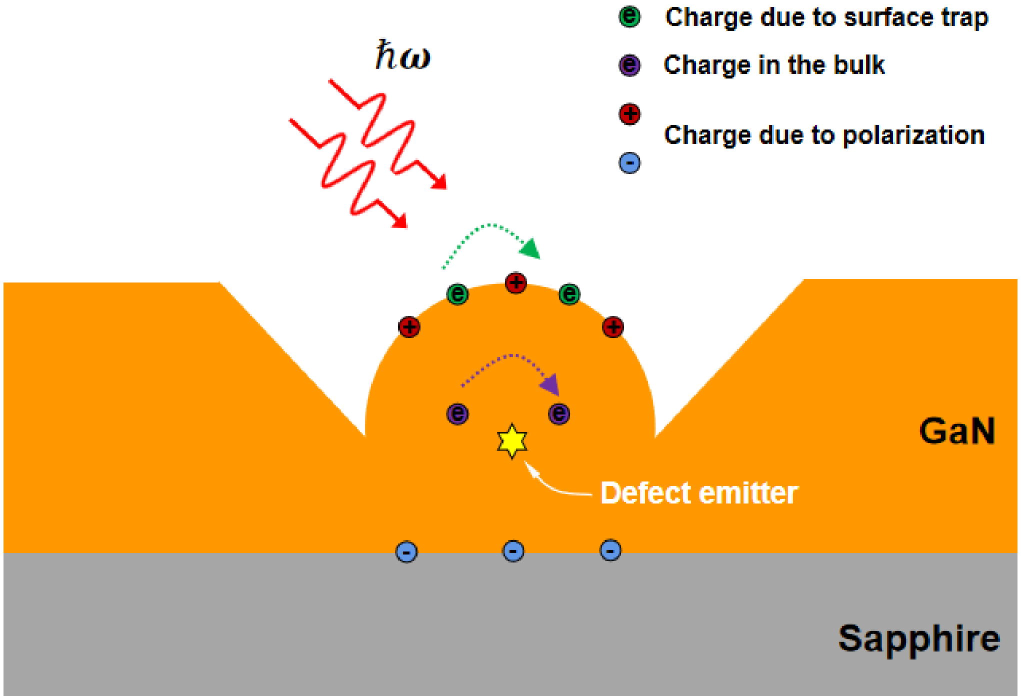

Figure 4.2: A schematic diagram of the GaN sample is presented. The 4 μm thick GaN epitaxial layer is grown on top of a sapphire substrate. A solid immersion lens with a diameter of 5 μm is fabricated using focused ion beam etching, and a defect emitter is located at the center of the lens. Various sources contribute to the electric field that the emitter can experience.

Let us discuss the possible sources of the electric field that the defect emitter might experience. Firstly, GaN is a polar material, which means there are polarization charges on its surface. Secondly, our sample is known to be impure (if it were pure, we would not observe single photon emitters in the first place), containing a significant number of impurities such as iron, carbon, hydrogen, and oxygen atoms, as well as vacancies, dislocations, and stacking faults. Thirdly, we used focused ion beam etching when processing the solid immersion lens, which is a highly aggressive process that removes atoms from the crystal surface. It can be imagined that this process creates many different defects on the surface. If these defects are charged, the defect emitter will experience an electric field due to Coulomb interactions. However, if this electric field is static and does not change over time, it will simply act as a stable background electric field for the defect emitter, not contributing to the broadening of the emission spectrum.

However, when the excitation laser is directed at the sample, the situation changes. The laser not only excites the defect emitter but also ionizes other defects, leading to processes such as the generation, annihilation, and diffusion of dynamic charges. Consequently, the defect emitter will experience a time varying background electric field, causing the emission spectrum to broaden accordingly.

Based on the discussion above, we would like to propose the following questions:

1. What is the magnitude of the spectral diffusion? In other words, how large is the energy difference?
2. What is the characteristic time scale of the spectral diffusion? In other words, how fast does the electric field vary?
3. How can these properties be measured?
4. How can spectral diffusion be mitigated?

In this chapter, we will address the above questions. The first question is straightforward to answer, as we already know the answer. The magnitude of the spectral diffusion directly corresponds to the emission linewidth (Gaussian component) at low temperature, which, as discussed in previous chapters, is roughly on the order of 1 meV. However, answering the other questions will require careful consideration, especially the second one. Ultrafast spectral diffusion timescales have been studied in various single photon emitter platforms, such as quantum dots [64, 65, 66, 67, 68], NV centers in diamond [69, 70], and defects in two-dimensional materials like hBN [71, 72, 35]. However, the spectral diffusion effect in GaN defect-based single photon emitter systems has not yet been investigated.

4.2 Time-dependent spectroscopy at low temperature

First, let us conduct some relatively simple yet important experiments as an initial step to investigate the spectral diffusion effect in GaN. We will use the confocal scanning microscope setup introduced in Chapter 2 to study the time-dependent properties of the emission spectrum at low temperatures.

First, as usual, the room temperature properties of the defect emitter we are studying in this project are presented in Figure 4.3. Figure 4.3 (a) shows an SEM image of the fabricated solid immersion lens used in this study. Figure 4.3 (b) presents the spatial PL map of the defect emitter integrated within the solid immersion lens, where the hotspot indicates the emitter and the circular boundary of the lens is clearly visible. Figure 4.3 (c) displays the PL spectrum of the defect emitter at room temperature, with a center wavelength of 672 nm. Figure 4.3 (d) shows the second-order correlation function measured at room temperature, where $g^{(2)}(0) = 0.14$ confirms that this is a single-photon emitter. (Indeed, these are the essential foundational experiments conducted each time we study a single photon emitter, even though they may seem trivial to us now.)

Now we cool the sample down to 10 K to observe the effects. We begin our investigation by measuring the time-dependent PL spectrum of the defect emitter under an excitation laser power of 150 μW. Figure 4.4 (a) displays the emission spectrum over a 5-minute period, with each measurement frame having an exposure time of 2 seconds.

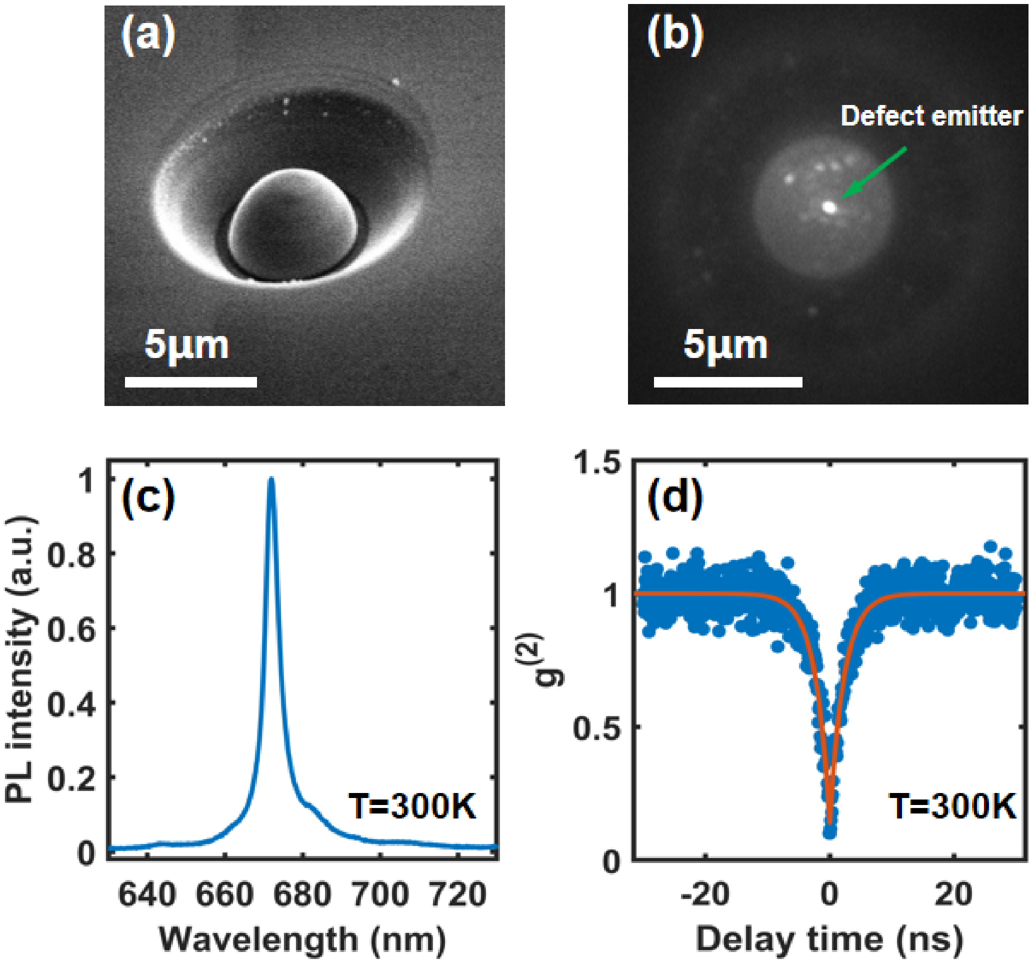

Figure 4.3: (a) The SEM image of the fabricated solid immersion lens used in this study. (b) The spatial PL map of the defect emitter integrated within the solid immersion lens, where the hotspot indicates the emitter and the circular boundary of the lens is clearly visible. (c) The PL spectrum of the defect emitter at room temperature, with a center wavelength of 672 nm. (d) The second-order correlation function measured at room temperature, where $g^{(2)}(0) = 0.14$ confirms that this is a single-photon emitter.

The averaged PL spectrum over 5 minutes is shown in Figure 4.4 (b), where the measured data can be fitted by a Gaussian curve with a center energy of 1854.2 meV and a linewidth (FWHM) of 1.07 meV. A blue shift of the emission energy at low temperature is observed, as expected, and the Gaussian lineshape is also anticipated, as discussed in Chapter 2. Spectral diffusion, which causes an inhomogeneous line shape at low

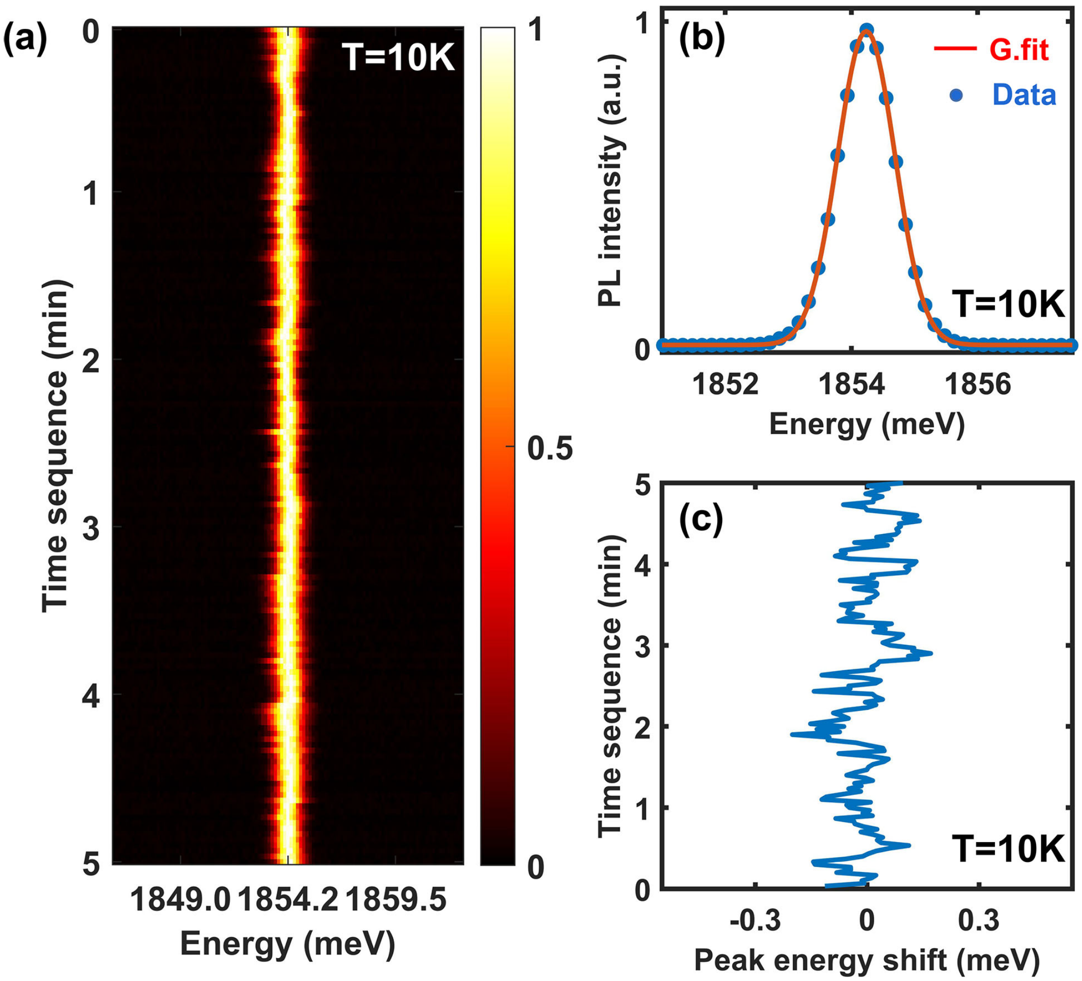

Figure 4.4: (a) The time-dependent PL spectrum of the defect emitter at 10 K over a 5-minute period is shown, with each measurement frame having an exposure time of 2 seconds. The color bar indicates the normalized PL intensity. (b) The averaged PL spectrum data collected over 5 minutes at 10 K, along with a Gaussian fit, is presented. The center energy is 1854.2 meV, and the Gaussian linewidth (FWHM) is 1.07 meV. (c) The fluctuation of the fitted Gaussian center energy for each measurement frame during the 5-minute period is illustrated.

temperatures when phonon-induced linewidth broadening is negligible, is known to be Gaussian, a feature observed in many other material platforms. Figure 4.4 (c) displays the fluctuation of the fitted Gaussian center energy for each measurement frame over 5 minutes, showing that the peak energy randomly fluctuates within the range of -0.1 to 0.1 meV, with a standard deviation of 0.069 meV. This random fluctuation conforms to a Gaussian distribution, which is a typical characteristic of spectral diffusion. In other words, the fluctuation of the local electric field experienced by the defect emitter follows a Gaussian random process.

In our measurement scheme, with each measurement frame taken every two seconds, the average spectral linewidth is 1.07 meV, while the standard deviation of the spectral fluctuations is only 0.069 meV, accounting for just 6.4% of the total linewidth. This indicates that the defect emitter does not exhibit substantial spectral diffusion over a timescale of seconds, suggesting that the linewidth broadening is most likely attributed to ultrafast spectral diffusion.

In other words, the characteristic timescale of spectral diffusion is very short (on the order of microseconds, as we will confirm later), so when we measure the spectral data every 2 seconds, spectral diffusion has already undergone millions of cycles. Consequently, the information regarding spectral diffusion has been averaged out in our results, and our measurement cannot effectively capture that rapid dynamics.

So where does this problem arise? The issue stems from the CCD detector of the spectrometer. CCD detectors have a readout time, which limits their response speed to the order of seconds (or, at best, a few hundred milliseconds), much longer than the timescale we are interested in.

In the presence of spectral diffusion, we can visualize the emission of photons from the defect emitter as illustrated in Figure 4.5. The horizontal axis represents the energy of emitted photons, while the vertical axis indicates the flow of time. The red circles in the diagram represent the emitted photons. For example, the diagram shows the emitter emitting a photon with energy E_1 at time t_1, a photon with energy E_4 at time t_2, a photon with energy E_2 at time t_3, a photon with energy E_3 at time t_4. Each emitted photon has

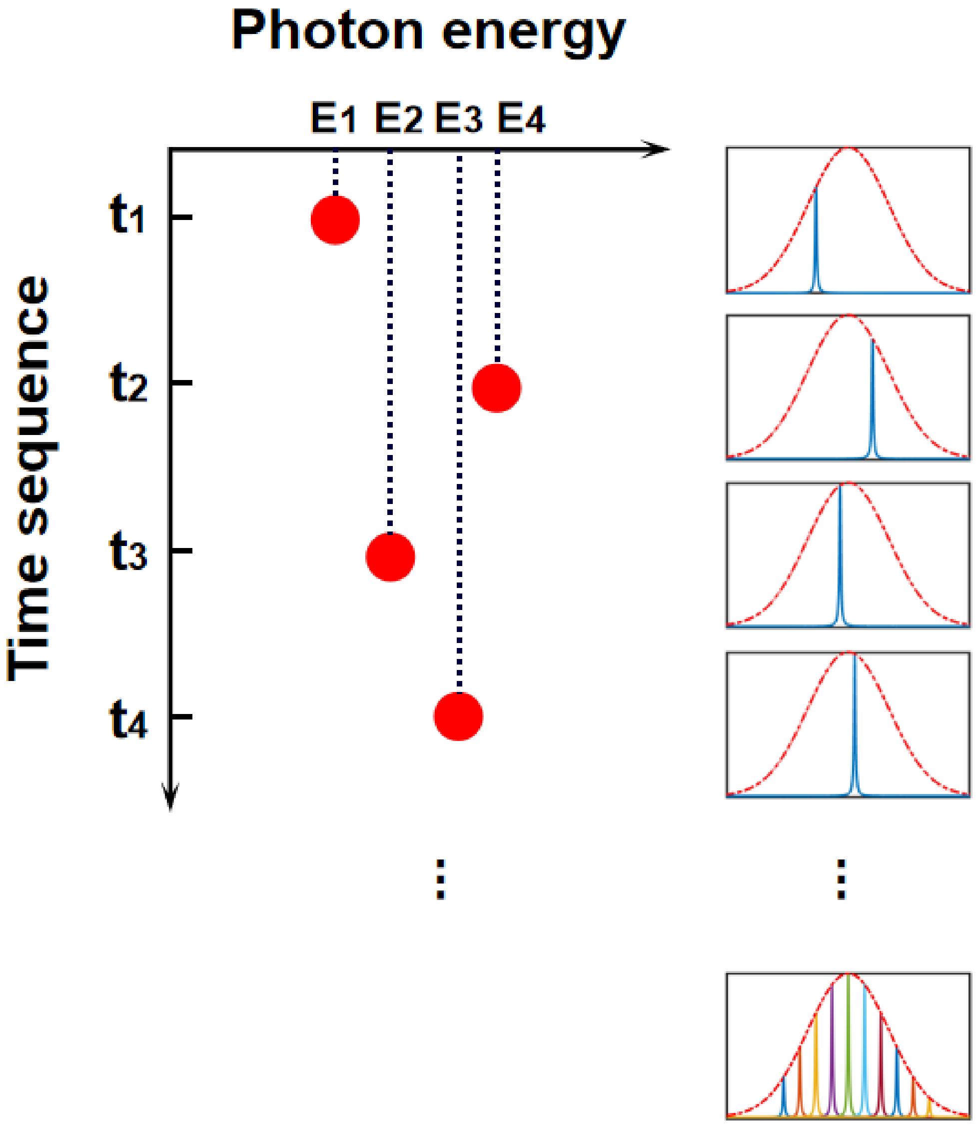

Figure 4.5: The "nature" of spectral diffusion reveals that the defect emitter emits photons with varying energies over time. The intrinsic line for each single photon (akin to a delta function) randomly shifts under a Gaussian envelope function. When a million photons are collected, these intrinsic lines are averaged out, resulting in only the Gaussian envelope being visible. Conversely, if we had a perfect spectrometer with infinitesimal spectral and temporal resolution, we could directly observe the motion illustrated in the diagram, where the intrinsic line "diffuses" randomly from one spectral position to another.

a very narrow intrinsic linewidth determined by the lifetime (akin to a delta function). However, the central energy of the emitted photons varies due to spectral diffusion, as labeled E_1 to E_4 in the diagram.

The right part of Figure 4.5 displays the positions of the intrinsic spectral lines (blue lines) at different times, along with the Gaussian envelope (red line) resulting from spectral diffusion. The emission spectrum is modulated by this Gaussian envelope. Although each individually emitted photon adheres to the intrinsic linewidth, the random fluctuations of each photon within this Gaussian envelope lead to averaging effects when many cycles are accumulated (imagine collecting millions of photons). As a result, the very narrow intrinsic lines are averaged out, and the spectral data we ultimately obtain reveal only the Gaussian envelope.

This phenomenon is precisely what we observe in Figure 4.4, where spectral data is collected every 2 seconds, resulting in the averaging out of all intrinsic spectral lines and leaving only the Gaussian envelope visible.

If there were a perfect spectrometer with infinitesimal time and spectral resolution (for example, capable of recording spectral data every femtosecond and resolving spectral differences of one picoelectronvolt), using such a device to measure the time-dependent emission spectrum would yield results identical to those shown in Figure 4.5. In this scenario, we could directly observe the intrinsic line jumps over time, allowing for the direct measurement of the characteristic time of spectral diffusion. Unfortunately, such an ideal spectrometer does not exist, and we cannot measure the characteristic time of spectral diffusion using this approach. However, this does not imply that measurement is impossible. In fact, there are many innovative methods available to assess such ultrafast properties. In the next section, we will introduce the measurement schemes that can be employed.

4.3 Measurement schemes

Our goal is to measure the characteristic time of ultrafast spectral diffusion. As experimental physicists, it is crucial to have a rough estimate of our experimental objectives before conducting experiments. Although we may not have a precise understanding of the specific range for this characteristic time, we can reasonably speculate on a few aspects. Firstly, we know that this characteristic time is much shorter than seconds, as conventional spectrometers cannot detect it, as stated earlier. So, how small might it be? We speculate that it is not shorter than the excited state lifetime of the defect emitter itself. From our $g^{(2)}$ results, we observe that the antibunching characteristic time is about a few nanoseconds, suggesting that the characteristic time of spectral diffusion may range from nanoseconds to seconds. While this may seem like limited progress, if this assumption is valid, it implies that we can use our HBT interferometer for this measurement. Since our HBT interferometer can detect features on the nanosecond scale, it should be capable of measuring this ultrafast spectral diffusion. It turns out this can indeed be accomplished.

Let us closely revisit the motion pattern of spectral diffusion represented in Figure 4.5. An important observation emerges: although each intrinsic line randomly jumps within the Gaussian envelope, at any specific moment, only one intrinsic line appears at a certain position in the energy (or wavelength) domain, rather than two or more, since this is a single photon emitter. A natural idea is to fully utilize the two channels of our HBT interferometer to measure the characteristic time of adjacent jumps.

As shown in Figure 4.6, if we can split the emission spectrum of the defect emitter into two halves—painting the left side light green and the right side light red—we can then send the photons from the left and right sides to the two channels of the HBT inter-

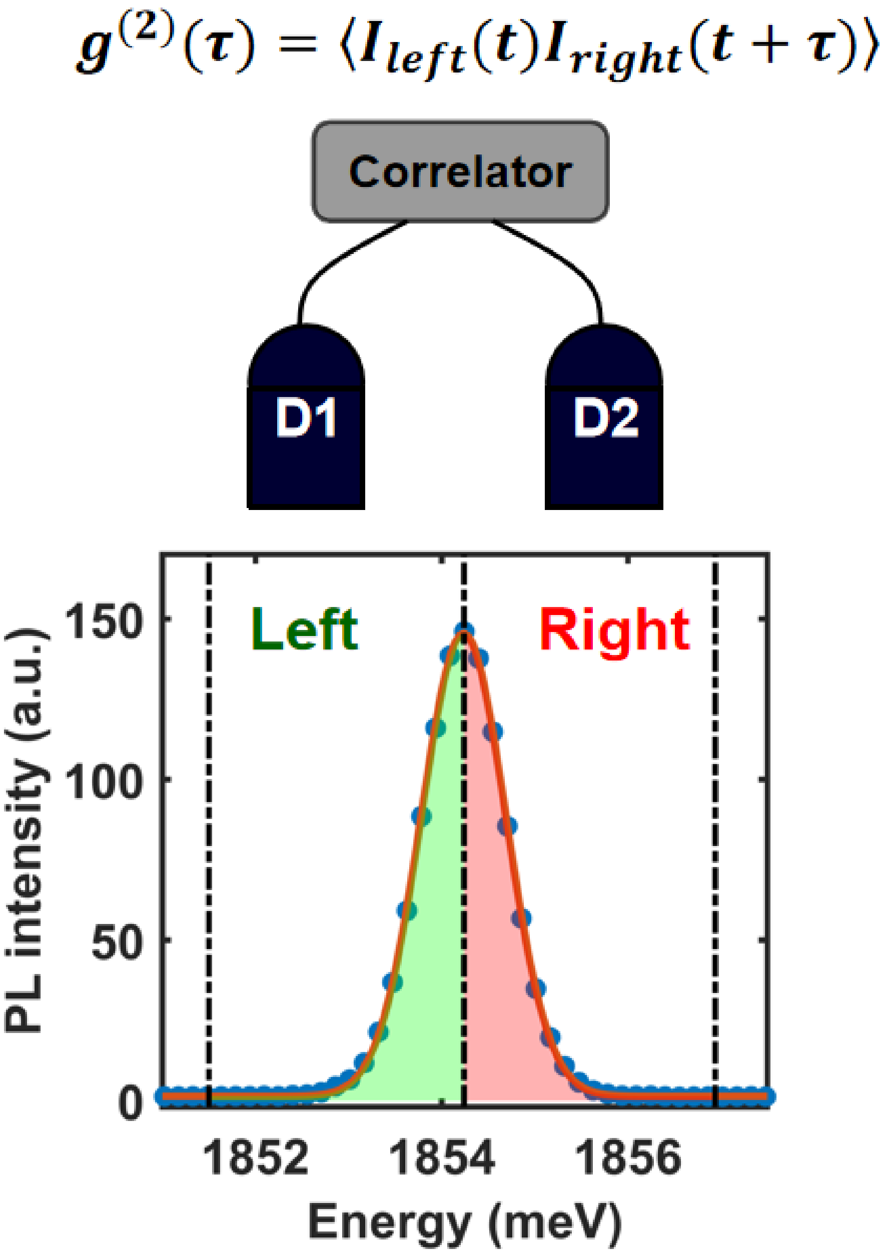

Figure 4.6: If we can split the emission spectrum of the defect emitter into two halves, painting the left side light green and the right side light red, we can send the photons from the left and right sides to the two channels of the HBT interferometer, respectively. This setup allows us to measure the cross-correlation function between the left half of the spectral window and the right half.

ferometer, respectively. This setup allows us to measure the cross-correlation function between the two channels. We will observe a significant result: when a photon's intrinsic line appears on the left at a certain moment, it is impossible for a photon to appear on the right at the same time, resulting in zero coincident counts (cross-correlation equals zero). However, if there is a time delay between the two channels, receiving a photon on the left at a certain moment creates the possibility of detecting a photon on the right after a specific time interval, leading to non-zero coincident counts (cross-correlation equals one).

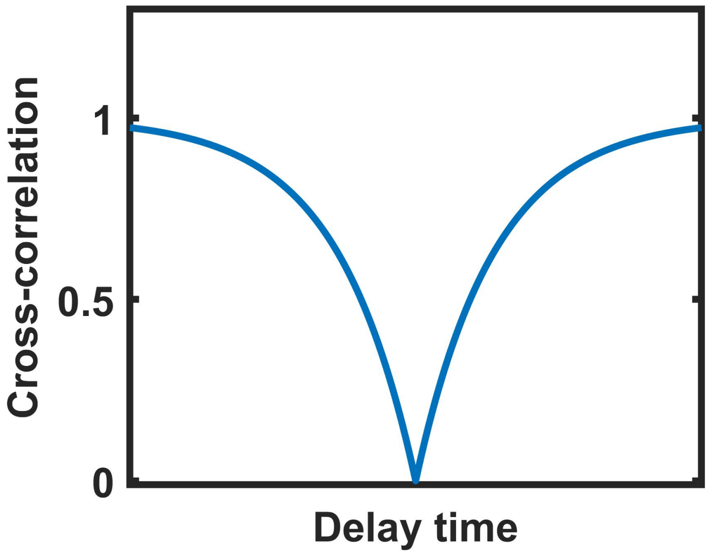

Figure 4.7: The cross-correlation function between the left half and the right half of the spectrum should exhibit this antibunching feature, where the antibunching time serves as a measure of the characteristic time of spectral diffusion. While this demonstrates an "antibunching" feature, its physical interpretation differs significantly from the antibunching observed earlier when determining the identity of the single photon emitter.

It is precisely the spectral diffusion that causes the intrinsic emission line of the photon to “diffuse” from the left half window to the right half window. When we conduct this experiment, we expect to observe the results illustrated in Figure 4.7, which displays an “antibunching-like” feature. However, it’s important to note that this antibunching feature differs from the previously measured $g^{(2)}$ function used to demonstrate single-photon sources; while they exhibit similar characteristics, their underlying physics is entirely distinct. In this context, the characteristic time of antibunching represents the characteristic time of spectral diffusion, whereas the antibunching time in the $g^{(2)}$ function measures the defect emitter's lifetime.

The next question is how we can implement the experimental idea of splitting the emission spectrum into two halves. This is where the monochromator comes into play, as it is commonly used for precise spectral filtering.

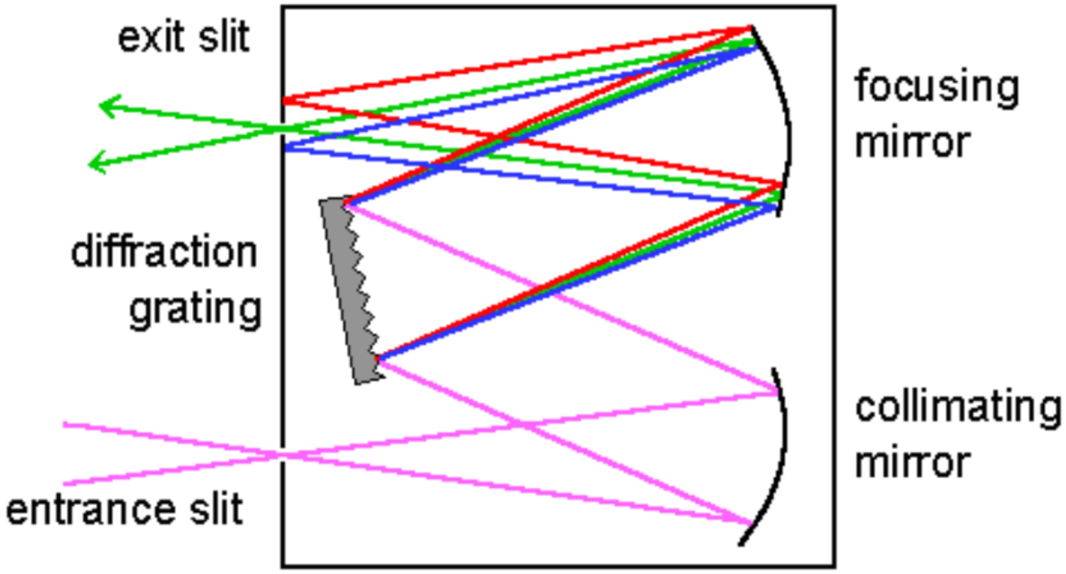

Figure 4.8: The internal structure of the monochromator is as follows: The incident light is focused by a lens onto the entrance slit. It then passes through a collimating mirror, converting the light into a collimated beam before it enters the grating. After dispersion by the grating, light of different wavelengths is focused by a focusing mirror onto various lateral positions of the exit slit. (Figure from https://www.chemicool.com/definition/monochromators.html)

Figure 4.8 shows the internal structure of the monochromator, which consists of an entrance slit, an exit slit, a grating, a focusing mirror, and a collimating mirror. The incident light is focused by a lens onto the entrance slit. It then passes through a collimating mirror, becoming collimated light before entering the grating. After dispersion by the grating, light of different wavelengths is focused by a focusing mirror onto various lateral positions of the exit slit. Due to the high spectral dispersion of the grating, the wavelength resolution of the monochromator typically reaches around 0.05 nm, depending on the groove density and focal length.

We use two monochromators, with the exit slit of each monochromator blocking one half of the emission spectrum, allowing only the right half to pass through for one monochromator and the left half for the other. The light exiting each monochromator is then directed into one of the two channels of the HBT interferometer, enabling the measurement of the cross-correlation between the left and right halves of the spectrum.

The corresponding optical setup is illustrated in Figure 4.9. The left side of the system is similar to the confocal scanning microscope described earlier in Chapter 2. The GaN sample is mounted in a cryostat and cooled to low temperatures. A galvo steering mirror and a 4F system are employed for scanning. The collected PL light from the defect emitter is split into two beams after passing through a confocal spatial filter, with each beam directed into one of the two monochromators. An HBT interferometer is then used to measure the cross-correlation function.

This is a great experimental scheme. The only limitation is that it requires two monochromators to filter the left half and right half of the spectrum, respectively. Unfortunately, I only have one available in my laboratory.

Experimental equipment is like a soldier's weapon for an experimental physicist. Without good tools, achieving quality results can be challenging. However, skilled experimental physicists find ways to work around limitations. In our case, we can demonstrate that using just one monochromator, we can still measure the characteristic time of spectral diffusion. While we will still need the HBT interferometer to measure the $g^{(2)}$ function, we will now focus on a specific (maybe small) portion of the spectrum rather

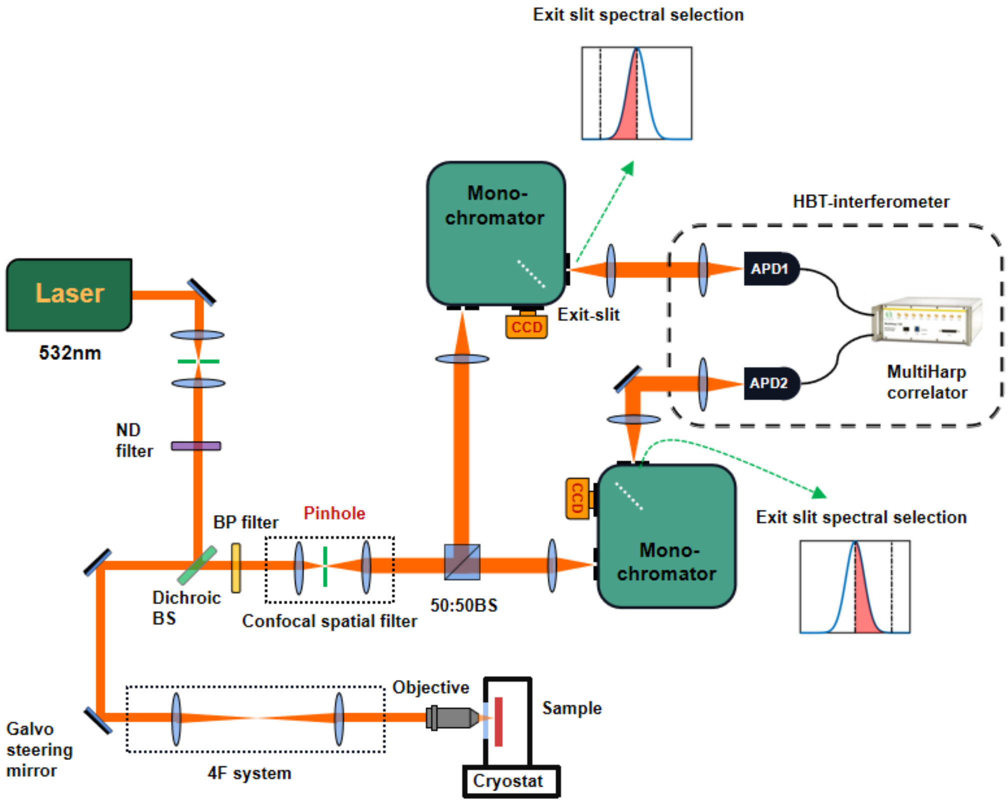

Figure 4.9: The optical system used for the cross-correlation measurement is similar to the confocal scanning microscope described earlier in Chapter 2. The collected PL light from the defect emitter is split into two beams after passing through a confocal spatial filter, with each beam directed into one of the two monochromators. Two monochromators are employed, with the exit slits configured to block one half of the emission spectrum, allowing only the right half to pass through for one monochromator and the left half for the other.

than the entire range.

The actual experimental setup used is illustrated in Figure 4.10. As before, the left side of the system retains the confocal scanning microscope. In the collection path, the PL light emitted by the defect emitter passes through a confocal spatial filter before being focused by a lens onto the entrance slit of the monochromator. We then adjust the width of the monochromator's exit slit and the angle of the grating to select a small

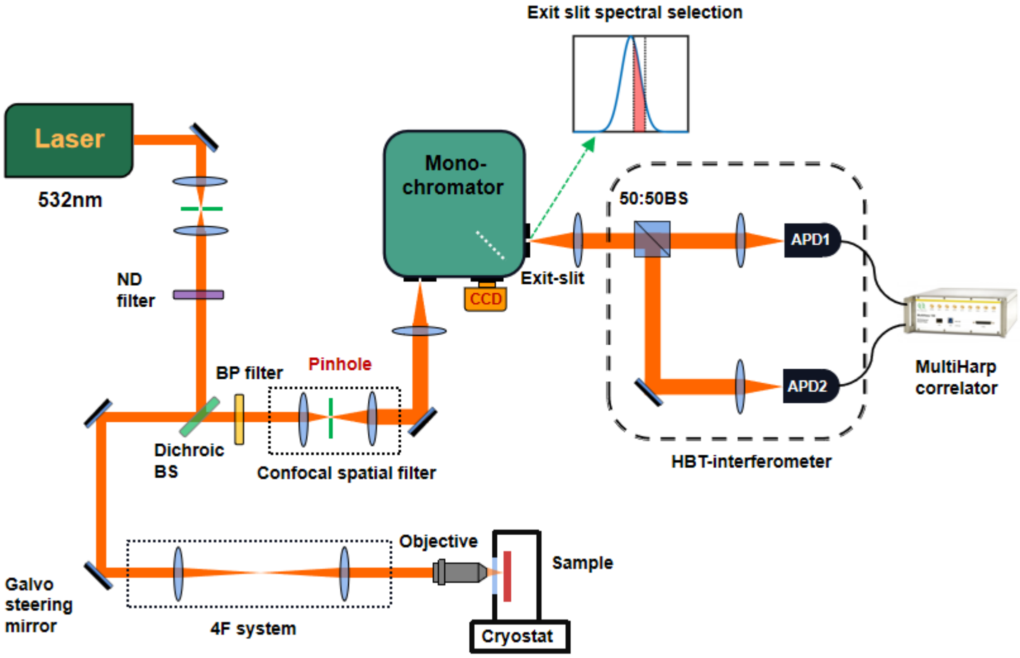

Figure 4.10: The actual experimental setup used in the spectral diffusion study is shown. We can measure spectral diffusion using only one monochromator, but we must select a specific portion of the spectrum for the $g^{(2)}$ measurement. By adjusting the exit slit width and the angle of the grating in the monochromator, we can choose different desired spectral windows of the PL spectrum from the defect emitter.

portion of the spectral window to feed into the HBT interferometer.

In this setup, the $g^{(2)}$ function measured by the HBT interferometer will exhibit not only an antibunching effect due to the single-photon nature of the emitter but also a bunching effect caused by spectral diffusion. The characteristic time of this bunching effect corresponds to the characteristic time of the spectral diffusion. Why does this occur? I will not delve into the detailed derivation here, but it can be found in reference [64].

It is important to highlight that the width of the spectral window does not affect the characteristic time of the bunching effect, which is our main focus; it only influences the height of the bunching effect. Specifically, a very small spectral window will result in a pronounced bunching effect (with a large height). In contrast, selecting a wide spectral window, or even no window at all, will lead to a faint bunching effect, or it may not appear at all. While a narrower spectral window enhances the significance of the bunching, it also limits the number of photons entering the HBT interferometer, thereby restricting the signal-to-noise ratio of the measurement. Typically, choosing around 1/4 of the emission spectrum is a reasonable compromise for this experiment.

Before we discuss the experimental results, I would like to briefly introduce another completely different experimental system that is also widely used to measure spectral diffusion.

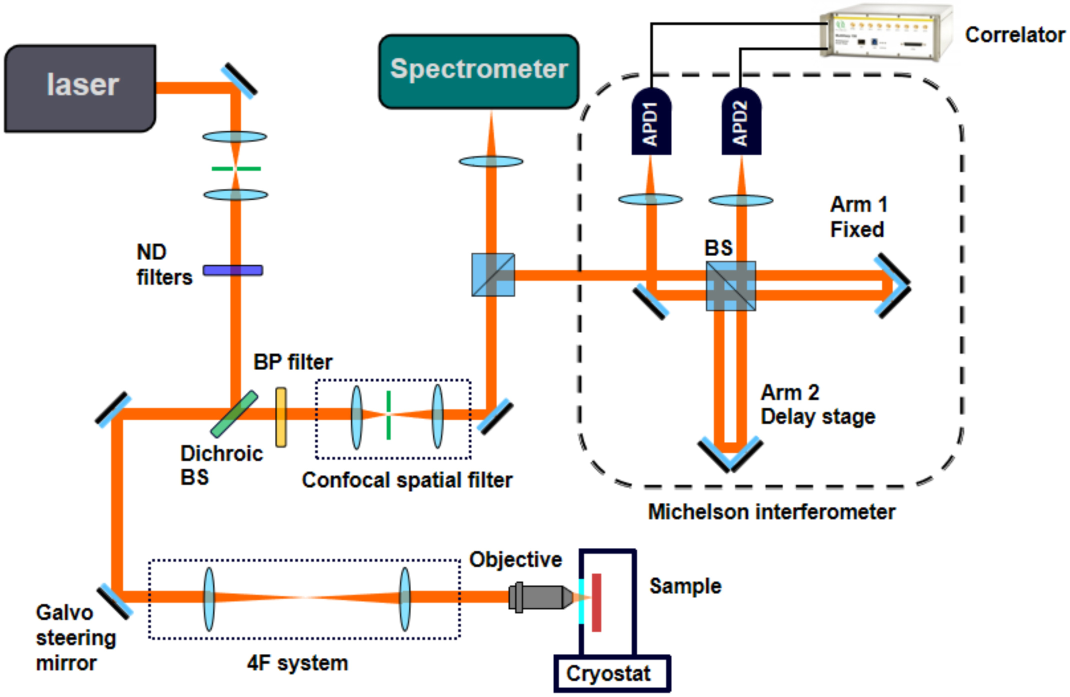

Figure 4.11: The Michelson interferometer-based optical system can also be used to study the spectral diffusion effect. The setup is shown, though we do not use it in this study.

Figure 4.11 shows the setup for an ultrafast spectral diffusion measurement based on a Michelson interferometer scheme. In this setup, the left part remains the confocal scanning microscope; however, in the collection path, the PL light emitted by the defect emitter is directed into a Michelson interferometer (instead of an HBT interferometer). Arm 1 of the Michelson interferometer has a fixed length, while arm 2 is mounted on a delay stage that can change the optical path length. The results obtained through the Michelson interferometer can also characterize the coherence properties of the defect emitter and the characteristic time of spectral diffusion. This approach is typically used for extremely weak signals (such as when the emitter's brightness is very low) and is not affected by the SNR limitations imposed by spectral selection. However, the trade-off is that the Michelson interferometer requires high mechanical precision and very careful optical alignment. More information about this approach can be found in reference [71].

4.4 Experimental results and discussion

Figure 4.12 (a) shows that when the exit slit (indicated by the black dashed lines) is fully open to direct all the PL light from the defect emitter (pink shaded area) into the HBT interferometer, the regular antibunching effect, attributed to single-photon emission, is observed in the measured second-order correlation function ($g^{(2)}$), as presented in Figure 4.12 (c). However, when the exit slit width is adjusted to select a spectral window covering approximately one quarter of the total PL emission spectrum, as depicted in Figure 4.12 (b), the second-order correlation function exhibits both the antibunching effect at zero time delay and a bunching effect due to spectral diffusion. The bunching occurs because if the time delay between two photons is large enough, local electric field fluctuations can shift the energy of the second photon outside the selected spectral window, leading to a smaller $g^{(2)}$ value. Thus, the characteristic time of the bunching effect in the $g^{(2)}$ function measures the time scale of spectral diffusion. Since the bunch-

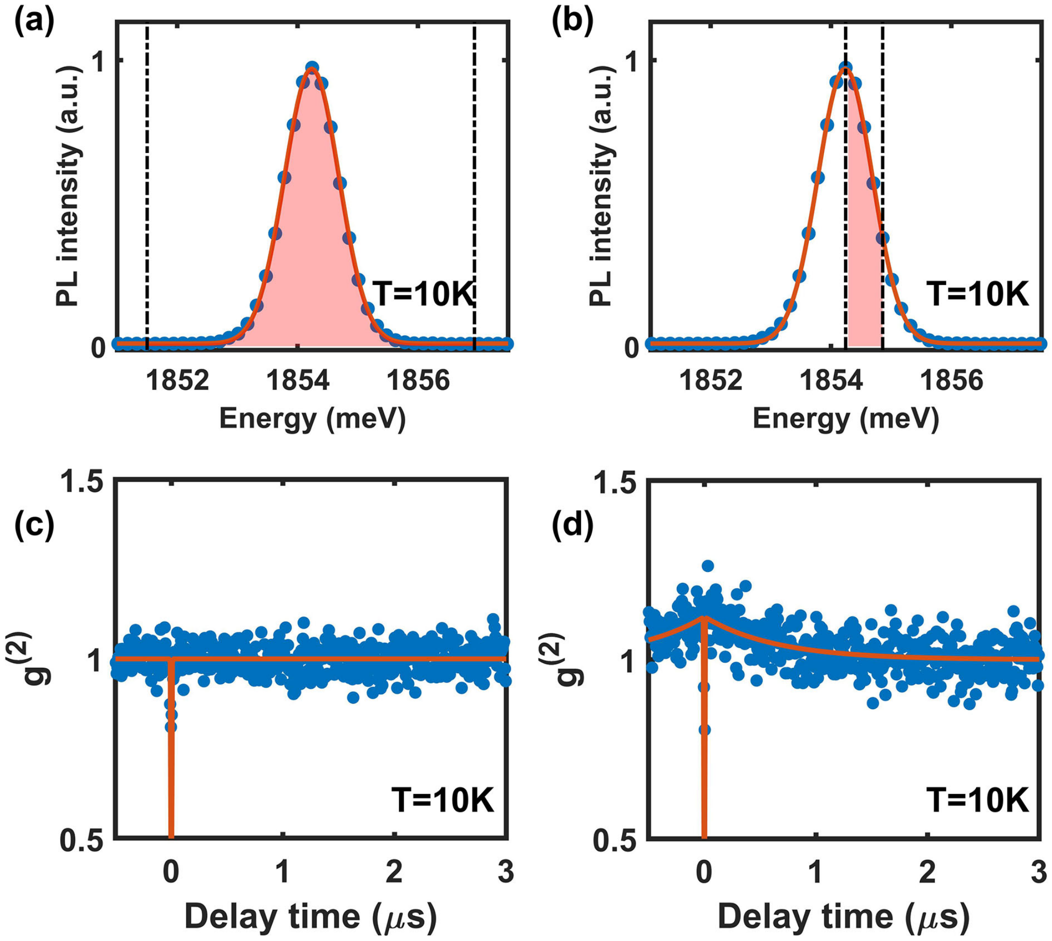

Figure 4.12: (a) The spectral window selected by the exit slit of the monochromator (indicated by the black dashed lines) covers the entire PL spectrum (shown by the shaded pink area). (b) The spectral window selected by the exit slit of the monochromator (indicated by the black dashed lines) covers about one quarter of the PL spectrum (shown by the shaded pink area). (c) The measured second-order correlation function ($g^{(2)}$) for the case described in (a) with a laser power of 150 μW. (d) The measured second-order correlation function ($g^{(2)}$) for the case described in (b) with a laser power of 150 μW.

ing effect, related to spectral diffusion, occurs at around $\sim \mu s$, the measurement's time resolution is set to 7.04 ns, effectively averaging out the antibunching effect as shown in Figures 4.12 (c-d). Importantly, this bunching arises solely from spectral diffusion, not from the metastable state of the defect emitter, as the excitation laser power is carefully controlled (150 μW, well below saturation), resulting in no noticeable bunching from the metastable state, as seen in Figure 4.12 (c).

The measured $g^{(2)}$ data can be fitted using the function:[64, 66]

$$g^{(2)}(\tau) = \left[1 - \alpha exp(-\frac{|\tau|}{\tau_e})\right]\left[1 + \beta exp(-\frac{|\tau|}{\tau_{SD}})\right] \tag{4.1}$$

Here, τ_e represents the characteristic time for the antibunching effect, while τ_{SD} represents the characteristic time for spectral diffusion. Previous works have demonstrated that the width of the selected spectral window does not affect the characteristic time of the bunching effect, but only its height [64, 65]. Figure 4.12 (d) illustrates the characteristic time of spectral diffusion to be $\tau_{SD} = 0.64 \pm 0.11 \mu s$. Considering that the lifetime of the single-photon emitter (SPE) estimated in Figure 4.12 (e) is 2.3 ns, the spectral diffusion characteristic time is two orders of magnitude longer than the emitter's lifetime. Consequently, this defect emitter can emit several hundred indistinguishable photon wave packets before local electric field fluctuations shift the emission energy to distinguishable values, as shown in Figure 4.13.

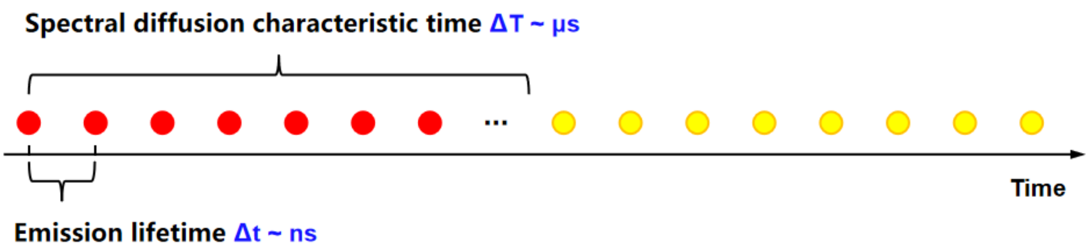

Figure 4.13: The physical explanation of spectral diffusion involves the lifetime of a defect emitter, which is $\sim$ ns, while the characteristic time of spectral diffusion is $\sim$ μs. This defect emitter emits a photon every $\sim$ ns, and these photons are indistinguishable. After emitting several hundred photons, the emitter undergoes spectral diffusion, shifting to another wavelength and continuing to emit photons. This shift corresponds to approximately 1 meV in the energy domain.

In the following discussion, we examine the dependency of the spectral diffusion rate and PL spectrum Gaussian linewidth on the excitation laser power. To ensure long-term

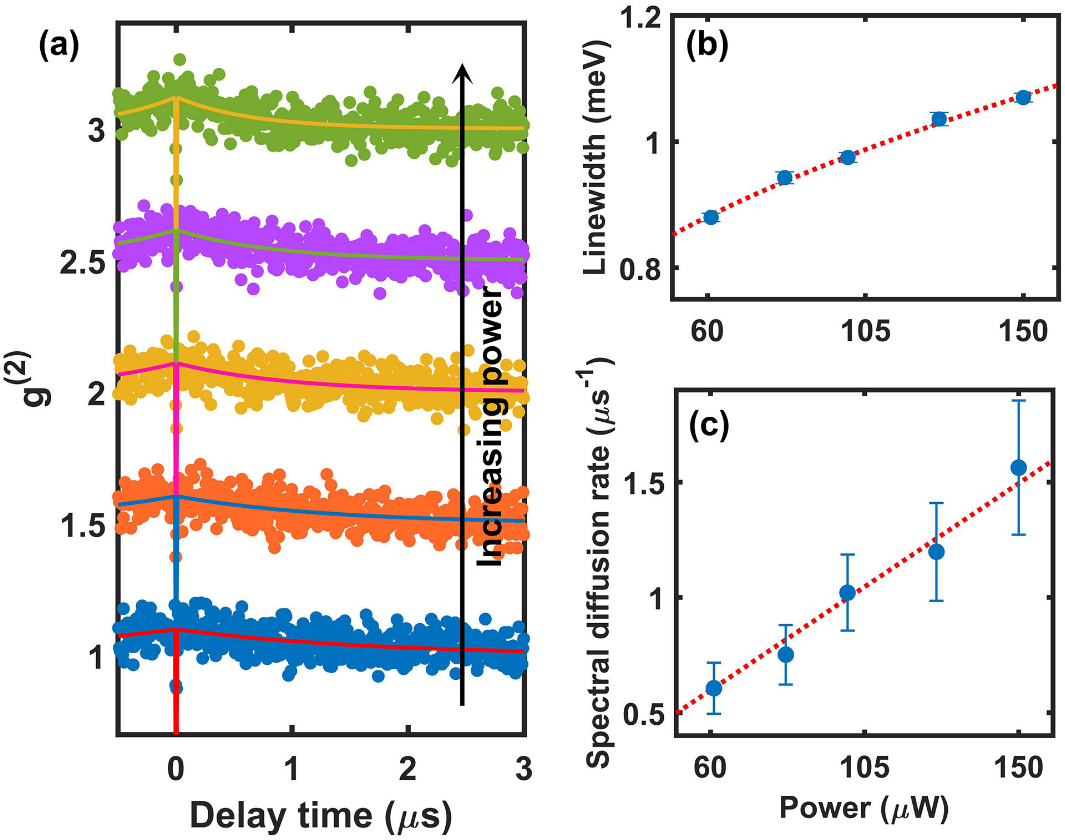

Figure 4.14: (a) The excitation laser power dependent photon autocorrelation results at 10 K in the case described in Fig.4.12 (b) are shown. (b) The excitation laser power dependent PL spectrum Gaussian linewidth of the defect emitter is shown. (c) The excitation laser power dependent spectral diffusion rate obtained by fittings in (a) is shown.

photostability and prevent metastable state transitions from contributing to the bunching effect, the laser power is limited to a maximum of 150 μW. Spectral diffusion is attributed to the fluctuating Stark shifts of the emitter induced by the local electric environment, hence, it is anticipated to be influenced by the number of excited charges in the environment, which is assumed to be proportional to the laser power[73]. While keeping the photon autocorrelation measurement condition described in Figure 4.12 (b) unchanged, the excitation laser power is varied in the range from 61 μW to 150 μW. As a result, the characteristic time of the bunching effect in the $g^{(2)}$ function decreases with increasing power, as shown in Figure 4.14 (a). By fitting the measured data with Eq. 4.1, we find that the spectral diffusion rate, expressed in units of μs^{-1} (which is $1/\tau_{SD}$), exhibits a linear dependence on the excitation laser power, as shown in Figure 4.14 (c). This linear dependence has also been observed in other SPE platforms, such as NV centers in diamond[69], quantum dots[66, 65, 68, 74], and defect emitters in 2D materials like hBN[35]. This observation is consistent with the assumption that spectral diffusion is governed by single carrier processes rather than multiple carrier processes like Auger-assisted carrier escape from traps or two-photon processes like photoinduced charge conversion[69, 66, 65]. In the limit of zero laser power, we observe that the spectral diffusion rate also approaches zero, confirming the excitation laser as the primary cause of spectral diffusion. Additionally, Figure 4.14 (b) illustrates the relationship between the PL spectrum linewidth of the defect emitter and the laser power. As the power increases from 61 μW to 150 μW, the linewidth only increases by about 20%, from 0.88 meV to 1.07 meV, and the measured linewidth data exhibits a nearly square root dependence on the laser power, which has also been reported previously in the GaN quantum dot system[73].

Spectral diffusion in SPEs limits quantum applications that demand indistinguishable photon emission. At cryogenic temperatures, the reported Gaussian linewidth of SPEs in various platforms is typically of the order $\sim$ meV, but the measured spectral diffusion characteristic time scale for different systems varies over a relatively wide range. The characteristic time (τ_{SD}) of regular quantum dot systems is reported to be in the order of a few nanoseconds to a few hundred nanoseconds[64, 66, 65, 67]. Nonpolar InGaN quantum dots are reported to have a maximum characteristic time of 1170 ns[68]. NV centers in diamond are reported to have a spectral diffusion characteristic time of 4.6 μs[69]. And defects in hBN have been reported to exhibit characteristic times of 23 μs[71] and also in a range of 0.32 to 3.9 μs[35]. In contrast, τ_{SD} in GaN defect-based

SPE systems is on the order of $\sim 1\ \mu s$, placing it in an intermediate region between quantum dot systems and defects in 2D materials or color centers in diamond. The bare defect SPEs in GaN can only emit a few hundred indistinguishable photon wave packets each time. Clearly, to enable more applications, integrating GaN defect SPEs into photonic cavities to harness the full potential of the Purcell effect is an important approach to overcome the limitations faced by bare SPEs[75, 76].

CHAPTER 5

SUMMARY AND CONCLUSION

In Chapter 1, we introduced the fundamentals of single-photon sources and presented our target of investigation: the GaN defect single-photon emitter. Following this, Chapters 2, 3, and 4 discuss three key aspects of its properties: the dephasing mechanism, the optical dipole structure and orientation, and ultrafast spectral diffusion.

Despite the many favorable properties of GaN defect single-photon emitters, research on them is still in its early stages. For example, their underlying nature remains unclear, although we have discussed some possible candidates and supporting evidence. Understanding this nature is crucial for future efforts to create these emitters on demand and to couple them into photonic structures for on-chip applications.

Based on this, we can envision the next steps of our work. Firstly, using our existing experimental evidence, such as our conjecture that the defect is likely of the $X_{Ga}Y_{N}$ form discussed in Chapter 3 rather than a dislocation or stacking fault, we can conduct Density Functional Theory (DFT) calculations with different elements. Specifically, we should calculate the binding energies of possible defects and the orientations of their optical dipoles. Carbon and iron atoms may be the first elements to consider, given their high concentrations in the SIMS data, along with certain intrinsic vacancies in GaN.

Secondly, ion implantation experiments should be conducted. We can select pure GaN crystals, ensuring they do not contain defect emitters, and then intentionally implant atoms with a high potential to be candidates, such as carbon and iron. Additionally, we should adjust the annealing temperature to determine if defect emitters can be produced.

We have observed many sophisticated optical experiments that I hope you enjoyed.

However, we can also conduct certain electrical experiments on these defect emitters, such as cathodoluminescence (CL), and compare the results with photoluminescence (PL). This approach would be very beneficial for revealing their underlying nature.

If the above experiments can confirm the nature of these defect emitters in GaN, it would represent a significant breakthrough.

According to the big picture outlined in Chapter 1 regarding the field of single-photon sources, we should continue our research by studying their properties and applications. Research on the physical properties of a single-photon source can include investigations into its Stark shift, optical Rabi oscillation, response to external stress, and the recently proposed spin structure. We have also explored the optically detected magnetic resonance of the defect emitters at room temperature recently [77, 78, 79]. Even though they may not be ideal qubits, they still hold promise for quantum sensing applications.

In addition to researching their physical properties, we can also explore their applications. For example, we can couple a defect emitter into a photonic cavity to study the Purcell effect, or integrate it into an optical waveguide for on-chip single-photon source applications. Furthermore, we can combine single-photon sources with other trending topics in classical optics, such as topological photonics [80, 81] and orbital angular momentum [82]. What is even more exciting is that if we can determine their nature, we could intentionally implant defect emitters into GaN-based p-i-n junctions and then flow current to excite them. This would enable us to achieve an electrically controlled single-photon source, eliminating the need for laser excitation. This concept is known as a single-photon diode, which serves as the quantum version of an LED. The GaN-based blue LED has transformed the world over the past few decades, and now, a quantum version of the LED that can emit single photons under electrical control would be highly significant for quantum communication. I believe this innovation could reshape the world once again.

Of course, we should also acknowledge the limitations of these defect emitters as single-photon sources. Firstly, they are not always very stable; for instance, long-term exposure to high-power lasers can lead to photobleaching. Secondly, the zero-phonon lines of these defect emitters are distributed over a wide range of 600-700 nm, making it difficult to find two emitters with exactly the same emission spectrum. In contrast, the NV center in diamond has a fixed zero-phonon line at 637 nm. This variability poses a challenge for using two defect emitters in photon interference experiments. Addressing these issues will naturally be one of the future research directions.

In conclusion, defect emitters in GaN appear to be highly promising candidates for single-photon sources. This field offers a vast expanse of boundless opportunities. I hope this dissertation has inspired you and sparked new ideas.

BIBLIOGRAPHY

[1] Igor Aharonovich, Dirk Englund, and Milos Toth. Solid-state single-photon emitters. *Nature Photonics*, 10(10):631–641, 2016.

[2] Julien Claudon, Joël Bleuse, Nitin Singh Malik, Maela Bazin, Périne Jaffrennou, Niels Gregersen, Christophe Sauvan, Philippe Lalanne, and Jean-Michel Gérard. A highly efficient single-photon source based on a quantum dot in a photonic nanowire. *Nature Photonics*, 4(3):174–177, 2010.

[3] Charles Santori, Matthew Pelton, Glenn Solomon, Yseulte Dale, and Yoshihisa Yamamoto. Triggered single photons from a quantum dot. *Physical Review Letters*, 86(8):1502, 2001.

[4] Yu-Ming He, Genevieve Clark, John R Schaibley, Yu He, Ming-Cheng Chen, Yu-Jia Wei, Xing Ding, Qiang Zhang, Wang Yao, Xiaodong Xu, et al. Single quantum emitters in monolayer semiconductors. *Nature nanotechnology*, 10(6):497–502, 2015.

[5] Toan Trong Tran, Kerem Bray, Michael J Ford, Milos Toth, and Igor Aharonovich. Quantum emission from hexagonal boron nitride monolayers. *Nature nanotechnology*, 11(1):37–41, 2016.

[6] Christian Kurtsiefer, Sonja Mayer, Patrick Zarda, and Harald Weinfurter. Stable solid-state source of single photons. *Physical review letters*, 85(2):290, 2000.

[7] Elke Neu, Mario Agio, and Christoph Becher. Photophysics of single silicon vacancy centers in diamond: implications for single photon emission. *Optics express*, 20(18):19956–19971, 2012.

[8] Stefania Castelletto, BC Johnson, Viktor Ivády, N Stavrias, T Umeda, A Gali, and T Ohshima. A silicon carbide room-temperature single-photon source. *Nature materials*, 13(2):151–156, 2014.

[9] Yongzhou Xue, Hui Wang, Nan Xie, Qian Yang, Fujun Xu, Bo Shen, Jun-jie Shi, Desheng Jiang, Xiuming Dou, Tongjun Yu, et al. Single-photon emission from point defects in aluminum nitride films. *The Journal of Physical Chemistry Letters*, 11(7):2689–2694, 2020.

[10] Amanuel M Berhane, Kwang-Yong Jeong, Zoltán Bodrog, Saskia Fiedler, Tim Schröder, Noelia Vico Triviño, Tomás Palacios, Adam Gali, Milos Toth, Dirk En-

glund, et al. Bright room-temperature single-photon emission from defects in gallium nitride. *Advanced Materials*, 29(12):1605092, 2017.

[11] Amanuel M Berhane, Kwang-Yong Jeong, Carlo Bradac, Michael Walsh, Dirk Englund, Milos Toth, and Igor Aharonovich. Photophysics of gan single-photon emitters in the visible spectral range. *Physical Review B*, 97(16):165202, 2018.

[12] Hutomo Suryo Wasisto, Joan Daniel Prades, Jan Gülink, and Andreas Waag. Beyond solid-state lighting: Miniaturization, hybrid integration, and applications of gan nano-and micro-leds. *Applied Physics Reviews*, 6(4), 2019.

[13] Shijie Zhu, Xinyi Shan, Runze Lin, Pengjiang Qiu, Zhou Wang, Xinyi Lu, Lintao Yan, Xugao Cui, Guoqi Zhang, and Pengfei Tian. Characteristics of gan-on-si green micro-led for wide color gamut display and high-speed visible light communication. *ACS Photonics*, 10(1):92–100, 2022.

[14] Stephen P Najda, Piotr Perlin, Tadek Suski, Lucja Marona, Mike Leszczyński, Przemek Wisniewski, Szymon Stanczyk, Dario Schiavon, Thomas Slight, Malcolm A Watson, et al. Gan laser diode technology for visible-light communications. *Electronics*, 11(9):1430, 2022.

[15] Chao-Tsung Ma and Zhen-Huang Gu. Review of gan hemt applications in power converters over 500 w. *Electronics*, 8(12):1401, 2019.

[16] Edward A Jones, Fei Fred Wang, and Daniel Costinett. Review of commercial gan power devices and gan-based converter design challenges. *IEEE journal of emerging and selected topics in power electronics*, 4(3):707–719, 2016.

[17] Kevin J Chen, Oliver Häberlen, Alex Lidow, Chun lin Tsai, Tetsuzo Ueda, Yasuhiro Uemoto, and Yifeng Wu. Gan-on-si power technology: Devices and applications. *IEEE Transactions on Electron Devices*, 64(3):779–795, 2017.

[18] Vishank Talesara, Yuxuan Zhang, Vijay Gopal Thirupakuzi Vangipuram, Hongping Zhao, and Wu Lu. Vertical gan-on-gan pn power diodes with baliga figure of merit of 27 gw/cm2. *Applied Physics Letters*, 122(12), 2023.

[19] Minh Nguyen, Tongtong Zhu, Mehran Kianinia, Fabien Massabuau, Igor Aharonovich, Milos Toth, Rachel Oliver, and Carlo Bradac. Effects of microstructure and growth conditions on quantum emitters in gallium nitride. *APL Materials*, 7(8):081106, 2019.

[20] Minh Anh Phan Nguyen, Jennifer Hite, Michael A Mastro, Mehran Kianinia, Mi-

los Toth, and Igor Aharonovich. Site control of quantum emitters in gallium nitride by polarity. *Applied Physics Letters*, 118(2):021103, 2021.

[21] Junxiao Yuan, Yidong Hou, Zenghui Yang, Feiliang Chen, and Qian Li. Gan as a material platform for single-photon emitters: Insights from ab initio study. *Advanced Optical Materials*, 11(8):2202158, 2023.

[22] Yifei Geng, Jialun Luo, Len van Deurzen, Debdeep Jena, Gregory Fuchs, and Farhan Rana. Temperature dependence of spectral emission from gan defect quantum emitters. In *APS March Meeting Abstracts*, volume 2022, pages D67–006, 2022.

[23] Yifei Geng, Jialun Luo, Len van Deurzen, Debdeep Jena, Gregory David Fuchs, Farhan Rana, et al. Temperature dependence of the emission spectrum of gan defect single-photon emitters. *arXiv e-prints*, pages arXiv–2206, 2022.

[24] Yifei Geng, Jialun Luo, Len van Deurzen, Debdeep Jena, Gregory David Fuchs, and Farhan Rana. Decoherence by optical phonons in gan defect single-photon emitters. *arXiv preprint arXiv:2206.12636*, 2022.

[25] Yifei Geng, Jialun Luo, Len van Deurzen, Huili Xing, Debdeep Jena, Gregory David Fuchs, and Farhan Rana. Dephasing by optical phonons in gan defect single-photon emitters. *Scientific Reports*, 13(1):8678, 2023.

[26] Yifei Geng, Debdeep Jena, Gregory D Fuchs, Warren R Zipfel, and Farhan Rana. Optical dipole structure and orientation of gan defect single-photon emitters. *ACS Photonics*, 10(10):3723–3729, 2023.

[27] Yifei Geng, Jialun Luo, Gregory Fuchs, and Farhan Rana. Optical dipole structure and orientation of gan defect single photon emitters. In *APS March Meeting Abstracts*, volume 2023, pages G41–003, 2023.

[28] Yifei Geng, Debdeep Jena, Gregory D Fuchs, Warren R Zipfel, and Farhan Rana. Optical dipole structure and orientation of gan defect single photon emitters. *arXiv preprint arXiv:2306.17339*, 2023.

[29] Yifei Geng and Kazuki Nomoto. Ultrafast spectral diffusion of gan defect single photon emitters. *Applied Physics Letters*, 123(17), 2023.

[30] Hamidreza Siampour, Shailesh Kumar, Valery A Davydov, Liudmila F Kulikova, Viatcheslav N Agafonov, and Sergey I Bozhevolnyi. On-chip excitation of sin-

gle germanium vacancies in nanodiamonds embedded in plasmonic waveguides. *Light: Science & Applications*, 7(1):1–9, 2018.

[31] Tzu-Yung Huang, Richard R Grote, Sander A Mann, David A Hopper, Annemarie L Exarhos, Gerald G Lopez, Amelia R Klein, Erik C Garnett, and Lee C Bassett. A monolithic immersion metalens for imaging solid-state quantum emitters. *Nature communications*, 10(1):1–8, 2019.

[32] L Marseglia, JP Hadden, Antony C Stanley-Clarke, JP Harrison, B Patton, Y-LD Ho, B Naydenov, F Jelezko, J Meijer, PR Dolan, et al. Nanofabricated solid immersion lenses registered to single emitters in diamond. *Applied Physics Letters*, 98(13):133107, 2011.

[33] Mohammad Jamali, Ilja Gerhardt, Mohammad Rezai, Karsten Frenner, Helmut Fedder, and Jörg Wrachtrup. Microscopic diamond solid-immersion-lenses fabricated around single defect centers by focused ion beam milling. *Review of Scientific Instruments*, 85(12):123703, 2014.

[34] Constantin Dory, Dries Vercruysse, Ki Youl Yang, Neil V Sapra, Alison E Rugar, Shuo Sun, Daniil M Lukin, Alexander Y Piggott, Jingyuan L Zhang, Marina Radulaski, et al. Inverse-designed diamond photonics. *Nature communications*, 10(1):1–7, 2019.

[35] Bernd Sontheimer, Merle Braun, Niko Nikolay, Nikola Sadzak, Igor Aharonovich, and Oliver Benson. Photodynamics of quantum emitters in hexagonal boron nitride revealed by low-temperature spectroscopy. *Physical Review B*, 96(12):121202, 2017.

[36] Benjamin Lienhard, Tim Schröder, Sara Mouradian, Florian Dolde, Toan Trong Tran, Igor Aharonovich, and Dirk Englund. Bright and photostable single-photon emitter in silicon carbide. *Optica*, 3(7):768–774, 2016.

[37] V Hizhnyakov and P Reineker. Optical dephasing in defect-rich crystals. *The Journal of chemical physics*, 111(17):8131–8135, 1999.

[38] Kai-Mei C Fu, Charles Santori, Paul E Barclay, Lachlan J Rogers, Neil B Manson, and Raymond G Beausoleil. Observation of the dynamic jahn-teller effect in the excited states of nitrogen-vacancy centers in diamond. *Physical Review Letters*, 103(25):256404, 2009.

[39] Tesfaye A Abtew, YY Sun, Bi-Ching Shih, Pratibha Dev, SB Zhang, and Peihong Zhang. Dynamic jahn-teller effect in the nv- center in diamond. *Physical review letters*, 107(14):146403, 2011.

[40] V Hizhnyakov, H Kaasik, and I Sildos. Zero-phonon lines: the effect of a strong softening of elastic springs in the excited state. *physica status solidi (b)*, 234(2):644–653, 2002.

[41] RH Silsbee. Thermal broadening of the mössbauer line and of narrow-line electronic spectra in solids. *Physical Review*, 128(4):1726, 1962.

[42] Lorenzo De Santis, Matthew E Trusheim, Kevin C Chen, and Dirk R Englund. Investigation of the stark effect on a centrosymmetric quantum emitter in diamond. *Physical Review Letters*, 127(14):147402, 2021.

[43] J. M. Ziman. *Electrons and Phonons*. Oxford University Press, 1st edition, 1960.

[44] D.F. Walls and Gerard J. Milburn. *Quantum Optics*. Springer Verlag, 2nd edition, 2008.

[45] T Ruf, J Serrano, M Cardona, P Pavone, M Pabst, M Krisch, M D'astuto, T Suski, I Grzegory, and M Leszczynski. Phonon dispersion curves in wurtzite-structure gan determined by inelastic x-ray scattering. *Physical review letters*, 86(5):906, 2001.

[46] Gordon Callsen, Juan Sebastián Reparaz, Markus R Wagner, Ronny Kirste, Christian Nenstiel, Axel Hoffmann, and Matthew R Phillips. Phonon deformation potentials in wurtzite gan and zno determined by uniaxial pressure dependent raman measurements. *Applied Physics Letters*, 98(6):061906, 2011.

[47] Ji-Yang Zhou, Qiang Li, Ze-Yan Hao, Fei-Fei Yan, Mu Yang, Jun-Feng Wang, Wu-Xi Lin, Zheng-Hao Liu, Wen Liu, Hao Li, Lixing You, Jin-Shi Xu, Chuan-Feng Li, and Guang-Can Guo. Experimental determination of the dipole orientation of single color centers in silicon carbide. *ACS Photonics*, 8(8):2384–2391, 2021.

[48] M. Andreas Lieb, James M. Zavislan, and Lukas Novotny. Single-molecule orientations determined by direct emission pattern imaging. *J. Opt. Soc. Am. B*, 21(6):1210–1215, Jun 2004.

[49] Jan Jasny and Jerzy Sepioł. Single molecules observed by immersion mirror objective. a novel method of finding the orientation of a radiating dipole. *Chemical Physics Letters*, 273(5):439–443, 1997.

[50] Martin Böhmer and Jörg Enderlein. Orientation imaging of single molecules by wide-field epifluorescence microscopy. *J. Opt. Soc. Am. B*, 20(3):554–559, Mar 2003.

[51] Digambara Patra, Ingo Gregor, and Jörg Enderlein. Image analysis of defocused single-molecule images for three-dimensional molecule orientation studies. *The Journal of Physical Chemistry A*, 108(33):6836–6841, 2004.

[52] Lucia Gardini, Marco Capitanio, and Francesco S Pavone. 3d tracking of single nanoparticles and quantum dots in living cells by out-of-focus imaging with diffraction pattern recognition. *Scientific Reports*, 5(1):1–10, 2015.

[53] Roman Schuster, Michael Barth, Achim Gruber, and Frank Cichos. Defocused wide field fluorescence imaging of single cdse/zns quantum dots. *Chemical physics letters*, 413(4-6):280–283, 2005.

[54] Digambara Patra, Ingo Gregor, Jörg Enderlein, and Markus Sauer. Defocused imaging of quantum-dot angular distribution of radiation. *Applied physics letters*, 87(10):101103, 2005.

[55] Clotilde Lethiec, Ferruccio Pisanello, Luigi Carbone, Alberto Bramati, Laurent Coolen, and Agnès Maitre. Polarimetry-based analysis of dipolar transitions of single colloidal cdse/cds dot-in-rods. *New Journal of Physics*, 16(9):093014, 2014.

[56] Satoshi Habuchi, Tatsuya Oba, and Martin Vacha. Multi-beam single-molecule defocused fluorescence imaging reveals local anisotropic nature of polymer thin films. *Physical Chemistry Chemical Physics*, 13(15):7001–7007, 2011.

[57] Liang Su, Haifeng Yuan, Gang Lu, Susana Rocha, Michel Orrit, Johan Hofkens, and Hiroshi Uji-i. Super-resolution localization and defocused fluorescence microscopy on resonantly coupled single-molecule, single-nanorod hybrids. *ACS nano*, 10(2):2455–2466, 2016.

[58] Masahiko Matsubara and Enrico Bellotti. A first-principles study of carbon-related energy levels in GaN. I. Complexes formed by substitutional/interstitial carbons and gallium/nitrogen vacancies. *Journal of Applied Physics*, 121(19), 05 2017. 195701.

[59] Masahiko Matsubara and Enrico Bellotti. A first-principles study of carbon-related energy levels in GaN. II. Complexes formed by carbon and hydrogen, silicon or oxygen. *Journal of Applied Physics*, 121(19), 05 2017. 195702.

[60] Darshana Wickramaratne, Jimmy-Xuan Shen, Cyrus E. Dreyer, Audrius Alkauskas, and Chris G. Van de Walle. Electrical and optical properties of iron in gan, aln, and inn. *Phys. Rev. B*, 99:205202, May 2019.

[61] John L. Lyons, Darshana Wickramaratne, and Chris G. Van de Walle. A first-principles understanding of point defects and impurities in GaN. *Journal of Applied Physics*, 129(11):111101, 03 2021.

[62] John L. Lyons, Evan R. Glaser, Mary Ellen Zvanut, Subash Paudel, Malgorzata Iwinska, Tomasz Sochacki, and Michal Bockowski. Carbon complexes in highly c-doped gan. *Phys. Rev. B*, 104:075201, Aug 2021.

[63] Stephen A Empedocles and Moungi G Bawendi. Quantum-confined stark effect in single cdse nanocrystallite quantum dots. *Science*, 278(5346):2114–2117, 1997.

[64] Gregory Sallen, Adrien Tribu, Thomas Aichele, Régis André, Lucien Besombes, Catherine Bougerol, Maxime Richard, Serge Tatarenko, Kuntheak Kheng, and J-Ph Poizat. Subnanosecond spectral diffusion measurement using photon correlation. *Nature Photonics*, 4(10):696–699, 2010.

[65] Kang Gao, Helen Springbett, Tongtong Zhu, Rachel A Oliver, Yasuhiko Arakawa, and Mark J Holmes. Spectral diffusion time scales in ingan/gan quantum dots. *Applied Physics Letters*, 114(11):112109, 2019.

[66] Kang Gao, Ivan Solovev, Mark Holmes, Munetaka Arita, and Yasuhiko Arakawa. Nanosecond-scale spectral diffusion in the single photon emission of a gan quantum dot. *AIP Advances*, 7(12):125216, 2017.

[67] Marco Abbarchi, Takashi Kuroda, Takaaki Mano, Massimo Gurioli, and Kazuaki Sakoda. Bunched photon statistics of the spectrally diffusive photoluminescence of single self-assembled gaas quantum dots. *Physical Review B*, 86(11):115330, 2012.

[68] Claudius Kocher, John C Jarman, Tongtong Zhu, Gunnar Kusch, Rachel A Oliver, and Robert A Taylor. Decreased fast time scale spectral diffusion of a nonpolar ingan quantum dot. *ACS Photonics*, 9(1):275–281, 2021.

[69] Janik Wolters, Nikola Sadzak, Andreas W Schell, Tim Schröder, and Oliver Benson. Measurement of the ultrafast spectral diffusion of the optical transition of nitrogen vacancy centers in nano-size diamond using correlation interferometry. *Physical review letters*, 110(2):027401, 2013.

[70] Laura Orphal-Kobin, Kilian Unterguggenberger, Tommaso Pregnolato, Natalia Kemf, Mathias Matalla, Ralph-Stephan Unger, Ina Ostermay, Gregor Pieplow, and Tim Schröder. Optically coherent nitrogen-vacancy defect centers in diamond nanostructures. *Physical Review X*, 13(1):011042, 2023.

[71] Boris Spokoyny, Hendrik Utzat, Hyowon Moon, Gabriele Grosso, Dirk Englund, and Moungi G Bawendi. Effect of spectral diffusion on the coherence properties of a single quantum emitter in hexagonal boron nitride. *The Journal of Physical Chemistry Letters*, 11(4):1330–1335, 2020.

[72] Clarisse Fournier, Kenji Watanabe, Takashi Taniguchi, Julien Barjon, Stéphanie Buil, Jean-Pierre Hermier, and Aymeric Delteil. Investigating the fast spectral diffusion of a quantum emitter in hbn using resonant excitation and photon correlations. *Physical Review B*, 107(19):195304, 2023.

[73] M Holmes, S Kako, K Choi, M Arita, and Y Arakawa. Spectral diffusion and its influence on the emission linewidths of site-controlled gan nanowire quantum dots. *Physical Review B*, 92(11):115447, 2015.

[74] Gregory Sallen, Adrien Tribu, Thomas Aichele, Régis André, Lucien Besombes, Catherine Bougerol, Maxime Richard, Serge Tatarenko, Kuntheak Kheng, and J-Ph Poizat. Subnanosecond spectral diffusion of a single quantum dot in a nanowire. *Physical Review B*, 84(4):041405, 2011.

[75] A Lyasota, C Jarlov, A Rudra, B Dwir, and E Kapon. Limiting the spectral diffusion of nano-scale light emitters using the purcell effect in a photonic-confined environment. *Scientific Reports*, 9(1):1195, 2019.

[76] Yuqing Huang, Rui Su, Yubin Wang, Chao Zhu, Jiangang Feng, Jiaxin Zhao, Zheng Liu, and Qihua Xiong. A fano cavity–photon interface for directional suppression of spectral diffusion of a single perovskite nanoplatelet. *Nano Letters*, 22(20):8274–8280, 2022.

[77] Jialun Luo, Yifei Geng, Farhan Rana, and Gregory D Fuchs. Room temperature optically detected magnetic resonance of single spins in gan. *Nature Materials*, 23(4):512–518, 2024.

[78] Jialun Luo, Yifei Geng, Farhan Rana, and Gregory D Fuchs. Room-temperature optically detected magnetic resonance of gan defect single-photon emitters. In *2023 Conference on Lasers and Electro-Optics (CLEO)*, pages 1–2. IEEE, 2023.

[79] Jialun Luo, Yifei Geng, Farhan Rana, and Gregory Fuchs. Room temperature optically detected magnetic resonance in single spins hosted in gan. *Bulletin of the American Physical Society*, 2024.

[80] YF Geng, ZN Wang, YG Ma, and F Gao. Topological surface plasmon polaritons. *Acta PhysicaSinica*, 68(22):224101, 2019.

[81] Geng Yi-Fei, Wang Zhu-Ning, Ma Yao-Guang, and Gao Fei. Topological surface plasmon. polaritons. *ACTA PHYSICA SINICA*, 68(22), 2019.

[82] Cuo Wu, Shailesh Kumar, Yinhui Kan, Danylo Komisar, Zhiming Wang, Sergey I Bozhevolnyi, and Fei Ding. Room-temperature on-chip orbital angular momentum single-photon sources. *Science Advances*, 8(2):eabk3075, 2022.